

POLITECNICO
MILANO 1863

SCHOOL OF INDUSTRIAL AND INFORMATION ENGINEERING

Master of science in Mechanical Engineering, Advanced Mechanical Design

Design of an innovative engine used as range extender for electric vehicles

Supervisor: Prof. Mario GUAGLIANO
Co-supervisor: Roberto PAPETTI

M. Sc. thesis work of:
Tommaso MARZI 875957

Academic Year 2017/2018

Table of Contents

1 Abstract 1
2 Introduction 2
3 State of the art 3
3.1 Range extender in automotive field 3
3.2 Design of an internal combustion engine outline 5
3.2.1 The crankshaft 6
3.2.2 The connecting rod 6
4 The RME range extender 8
4.1 The electric generator 8
4.2 Internal combustion engine 9
4.2.1 The crankshaft 10
4.2.2 The connecting rod 12
5 Design 13
5.1 Design for environment 13
5.1.1 Qualitative material analysis 13
5.1.2 Estimated increase of autonomy and comparison with BMW i3 14
5.2 Forces on the slider crank mechanism 17
5.2.1 Force generated by the pressure in the combustion chamber 17
5.2.2 Forces generated by the inertiae 18
5.2.3 Forces and schematization of the slider crank mechanism 22
5.3 Crankshaft design 25
5.3.1 Interference fit 25
5.3.1.1 Analytic design 26
5.3.1.2 Analytic static strength assessment 31
5.3.1.3 FEM static strength assessment 33
5.3.1.4 FEM contact pressure assessment 41
5.3.2 Static assessment of the crankshaft 44
5.3.3 FE model of the crankshaft 45
5.3.3.1 Analytical static strength assessment 54
5.3.3.2 FEM static strength assessment 62
5.3.3.3 FEM slipping analysis 66
5.3.4 Modal analysis of the crankshaft 68
5.4 Connecting rods design 70
5.4.1 FE model of the rod 70

5.4.2 FEM static strength assessment 76
5.4.3 Fretting assessment 78
5.5 Electric generator design 81
5.5.1 FE model of the stator 83
5.5.2 FEM plastic analysis on the holes of the stator 87
5.5.3 FEM slipping analysis of the contact surfaces of the stator 88
6 Fatigue design 89
6.1 Fatigue assessment on the crankshaft 92
6.2 Fatigue assessment on the rod 98
7 Conclusions 100
Bibliography 101
Appendix 1 103
Ringraziamenti 106

List of figures

FIGURE 1 - CONCEPTUAL LAYOUT OF A SERIES HYBRID DRIVETRAIN IMPLEMENTED ON A RANGE EXTENDED ELECTRIC VEHICLE 3
FIGURE 2 – 2012 CHEVROLET VOLT (1) AND NEW BMW I3 (2) 3
FIGURE 3 – EXAMPLE OF A MONOLITHIC CRANKSHAFT AND ITS MAIN PARTS (SOURCE: HTTP://WWW.EUROSPECSPORT.COM/PRODUCTS/COMPONENTS/PERFORMANCE-CRANKSHAFTS.HTM) 6
FIGURE 4 – EXAMPLE OF A CONNECTING ROD USED FOR MONOLITHIC CRANKSHAFT AND ITS MAIN PARTS (SOURCE: HTTPS://WWW.SICURAUTO.IT/TECNICA/NEWS/CHE-COSA-E-LA-BIELLA-E-COME-E-FATTA.HTML) 7
FIGURE 5 – RME RANGE EXTENDER 8
FIGURE 6 - SECTION VIEW OF THE INTERNAL COMBUSTION ENGINE WITH THE WIDTH AND DEPTH VALUES 9
FIGURE 7 – CRANKSHAFT 10
FIGURE 8 – THREE COMPONENTS OF THE CRANKSHAFT STRUCTURE 10
FIGURE 9 – SECTION VIEW OF THE CRANKSHAFT WITH THE DRILLED DUCTS FOR THE LUBRICATING OIL ARE HIGHLIGHTED IN RED 11
FIGURE 10 – CONNECTING ROD 12
FIGURE 11 – THERMOPLASTIC NOVEL COMPONENTS; OIL SUMP (1), RIGHT CYLINDER'S HEAD COVER (2), INLET COOLING WATER MANIFOLD (3) 14
FIGURE 12 - RESISTANT POWER AS A FUNCTION OF THE VEHICLE'S SPEED 15
FIGURE 13 – COMBUSTION CHAMBER ABSOLUTE PRESSURE AS A FUNCTION OF THE CRANK ANGLE; THE GRAPH REPRESENTS THE VALUE IN THE COMBUSTION CHAMBER OF ONE OF THE TWO PISTONS REFERRED TO 4 COMPLETE REVOLUTIONS 17
FIGURE 14 – FORCE GENERATED BY THE PRESSURE IN THE COMBUSTION CHAMBER ACTING ON THE PISTON 18
FIGURE 15 – ALTERNATIVE MASS AND ROTATIONAL MASS OF THE ROD 18
FIGURE 16 – PISTON WITH THE INERTIA FORCE APPLIED 20
FIGURE 17 - CRANKSHAFT WITH THE INERTIA FORCE (CENTRIFUGAL FORCE) APPLIED 21
FIGURE 18 - SCHEMATIZATION OF THE SLIDER CRANK MECHANISM WITH THE FORCES APPLIED 22
FIGURE 19 – SCHEMATIZATION OF THE CRANKSHAFT WITH THE APPLIED FORCES 24
FIGURE 20 – COUPLING BY INTERFERENCE FIT OF THE MAIN COMPONENTS OF THE CRANKSHAFT .. 25
FIGURE 21 – LONGITUDINAL SECTION VIEW OF THE ASSEMBLED CRANKSHAFT 25
FIGURE 22 – MODEL OF THE CRANKSHAFT FOR DETERMINING THE INTERNAL ACTION OF TORSION 26
FIGURE 23 - TORSION DIAGRAM OF THE BEAM MODEL OF THE CRANKSHAFT FOR THE MOST CRITICAL CASE (A=25°) 28
FIGURE 24 – REPRESENTATION OF THE MOST STRESSED COUPLING, THAT IS THE ONE BETWEEN THE POSTERIOR CRANK AND THE CENTRAL PART OF THE CRANKSHAFT 28
FIGURE 25 – EXTERNAL AND INTERNAL RADIUS OF THE HUB AND OF THE SHAFT 30
FIGURE 26 – HUB AND SHAFT WITH THE MAXIMUM CONTACT PRESSURE APPLIED 31
FIGURE 27 - LONGITUDINAL SECTION OF THE CRANKSHAFT, GEOMETRY OF THE SHAFT (UP-LEFT) AND GEOMETRY OF THE HUB (UP-RIGHT) 33
FIGURE 28 – ASSEMBLY OF THE SHAFT AND THE HUB 34
FIGURE 29 – SKETCHES OF THE AXISYMMETRIC SECTION OF THE SHAFT AND OF THE HUB USED IN THE FEM STATIC STRENGTH ASSESSMENT 34
FIGURE 30 – ABAQUS DEFINITION OF THE INTERACTION BETWEEN THE TWO SURFACES 35
FIGURE 31 – SURFACES INVOLVED IN THE INTERACTION PROPERTIES; THE RED SURFACE, THAT BELONGS TO THE SHAFT, IS THE MASTER, WHILE THE PURPLE SURFACE, THAT BELONGS TO THE HUB, IS THE SLAVE 35
FIGURE 32 – MESHED MODEL OF THE TWO COMPONENTS INVOLVED IN THE COUPLING 36
FIGURE 33 – RESULTS OF THE FIRST FEM ANALYSIS IN TERMS OF VON MISES STRESS 36
FIGURE 34 – PATH ON THE CONTACT SURFACE OF THE HUB USED FOR THE STRESSES EXTRAPOLATION 36
FIGURE 35 - TREND OF THE HOOP AND RADIAL STRESSES OF THE CONTACT SURFACE OF THE HUB37
FIGURE 36 – TREND OF THE MISES EQUIVALENT STRESS OF THE CONTACT SURFACE OF THE HUB . 37
FIGURE 37 - PATHS USED FOR THE STRESS EXTRAPOLATION: THE ONE ABOVE IS THE PATH ON THE CONTACT SURFACE WHILE THE ONE BELOW IN THE PATH ON THE INNER SURFACE OF THE SHAFT 38

FIGURE 38 - TREND OF THE HOOP AND RADIAL STRESSES OF THE CONTACT SURFACE OF THE SHAFT 38
FIGURE 39 - TREND OF THE MISES EQUIVALENT STRESS OF THE CONTACT SURFACE OF THE SHAFT 39
FIGURE 40 – TREND OF THE HOOP AND RADIAL STRESSES ON THE INNER SURFACE OF THE SHAFT 39
FIGURE 41 - TREND OF THE MISES EQUIVALENT STRESS ON THE INNER SURFACE OF THE SHAFT ... 40
FIGURE 42 - RESULTS OF THE SECOND FEM ANALYSIS IN TERMS OF EQUIVALENT PLASTIC STRAIN PEEQ 40
FIGURE 43 - SKETCHES OF THE AXISYMMETRIC SECTION OF THE SHAFT AND OF THE HUB USED IN THE FEM CONTACT PRESSURE ASSESSMENT 42
FIGURE 44 – MESHED MODEL USED FOR THE FEM CONTACT PRESSURE ASSESSMENT 42
FIGURE 45 – RADIAL STRESS S11 FOUND AS A RESULT FROM THE FEM ANALYSIS WITH THE MINIMUM ELASTIC INTERFERENCE 42
FIGURE 46 – PATH IMPLEMENTED ON THE CONTACT SURFACE OF THE HUB, USED FOR THE EXTRACTION OF THE RADIAL STRESS S11 43
FIGURE 47 – CONTACT PRESSURE TREND WITH THE MINIMUM ELASTIC INTERFERENCE 43
FIGURE 48 - VARIABLE FORCES ON THE CRANKSHAFT @ 4000 RPM 44
FIGURE 49 - CENTRIFUGAL FORCES ON THE CRANKSHAFT @ 4000 RPM 45
FIGURE 50 – IMPORTED MODELS OF THE POSTERIOR CRANKSHAFT (1), THE ANTERIOR CRANKSHAFT (2) AND THE CENTRAL PART OF THE CRANKSHAFT (3) 46
FIGURE 51 – DIMENSIONS OF THE DIAMETERS OF THE TWO HOLES IN THE CASE OF MAXIMUM ELASTIC INTERFERENCE AND MINIMUM ELASTIC INTERFERENCE 46
FIGURE 52 – ASSEMBLED MODEL OF THE CRANKSHAFT 47
FIGURE 53 – SLAVE SURFACE OF THE POSTERIOR CRANK PIN (PURPLE AREA ON THE LEFT COMPONENT) AND MASTER SURFACE OF THE HOLE OF THE CENTRAL PART OF THE CRANKSHAFT (RED AREA ON THE RIGHT COMPONENT) 48
FIGURE 54 – SECTION VIEW OF THE COUPLING AMONG THE POSTERIOR CRANK AND THE CENTRAL PART OF THE SHAFT 48
FIGURE 55 – INTERACTION PROPERTIES DEFINED FOR THE INTERFERENCE FIT 49
FIGURE 56 – BUSHING BEARINGS OF THE CRANKSHAFT THAT HAVE BEEN MODELLED IN THE FE MODEL 49
FIGURE 57 – SECTION VIEW OF THE CRANKSHAFT IN ABAQUS, WITH THE FOUR REFERENCE POINTS (RED DOTS) COUPLED WITH THEIR RELATED SURFACE (RED DASHED LINES) 50
FIGURE 58 – BOUNDARY CONDITION POSITIONED IN RP-1 THAT SIMULATES THE ROLLER (U1 AND U2 BLOCKED) AND THE RESISTANCE TORQUE (UR3 BLOCKED) 50
FIGURE 59 – BOUNDARY CONDITION POSITIONED IN RP-4 THAT SIMULATES THE HINGE (U1, U2 AND U3 BLOCKED) 50
FIGURE 60 – DEFINITION OF THE CENTRIFUGAL FORCE IN THE ROTATION STEP, SELECTING THE “ROTATIONAL BODY FORCE” ON THE LEFT AND WRITING IN THE ANGULAR SPEED OF 419 RAD/S ON THE RIGHT 51
FIGURE 61 – CENTRIFUGAL FORCE THAT APPEARS ON THE MODEL AFTER THE DEFINITION OF THIS TYPE OF LOAD 51
FIGURE 62 – FE MODEL WITH THE LOADS COMING FROM THE RODS APPLIED, IN PARTICULAR FOR THE CRANK ANGLE OF 374° (STEP NAMED ALPHA_374) 52
FIGURE 63 – ELEMENTS TYPE USED FOR THE COMPONENTS OF THE ANTERIOR CRANK (1), POSTERIOR CRANK (2) AND THE CENTRAL PART OF THE CRANKSHAFT (3); THE C3D20R ARE THE GREEN AND THE YELLOW ZONES WHILE THE C3D10 ARE THE REMAINING PINK ZONES 53
FIGURE 64 – EXAMPLE OF HOW THE MESH HAS BEEN IMPLEMENTED FOR THE PIN OF THE POSTERIOR CRANK 53
FIGURE 65 - BEAM MODEL OF THE CRANKSHAFT FOR A GENERIC CRANK ANGLE, WITH THE LOADS APPLIED. 54
FIGURE 66 - BEAM MODEL OF THE CRANKSHAFT WITH THE CENTRIFUGAL FORCES APPLIED 55
FIGURE 67 – BENDING MOMENT DIAGRAM RELATED TO THE CONSTANT CENTRIFUGAL FORCES 55
FIGURE 68 – BEAM MODEL OF THE CRANKSHAFT WITH THE VARIABLE LOADS THAT ACT ON THE Y-Z PLANE APPLIED, VALID FOR THE CRANK ANGLES OF 14° AND 25° 56
FIGURE 69 – BENDING MOMENT DIAGRAM IN THE PLANE Y-Z FOR THE CRANK ANGLES OF 14° AND 25° 56
FIGURE 70 – BEAM MODEL OF THE CRANKSHAFT WITH THE VARIABLE LOADS THAT ACT ON THE Y-Z PLANE APPLIED, VALID FOR THE CRANK ANGLES OF 374° AND 385° 57
FIGURE 71 – BENDING MOMENT DIAGRAM IN THE PLANE Y-Z FOR THE CRANK ANGLES OF 374° AND 385° 57

FIGURE 72 – BEAM MODEL OF THE CRANKSHAFT WITH THE VARIABLE LOADS APPLIED THAT ACT ON THE X-Z PLANE APPLIED, VALID FOR THE CRANK ANGLES OF 14° AND 25° 58
FIGURE 73 – BENDING MOMENT DIAGRAM IN THE X-Z PLANE FOR THE CRANK ANGLES OF 14° AND 25° 58
FIGURE 74 – BEAM MODEL OF THE CRANKSHAFT WITH THE VARIABLE LOADS APPLIED THAT ACT IN THE X-Z PLANE FOR THE CRANK ANGLES OF 374° AND 385° 59
FIGURE 75 – BENDING MOMENT DIAGRAM IN THE X-Z PLANE FOR THE CRANK ANGLES OF 347° AND 385° 59
FIGURE 76 - TORSION DIAGRAM OF THE CRANKSHAFT FOR A CRANK ANGLE OF 374° 60
FIGURE 77 – SECTION VIEW OF THE CRITICAL ZONE (SECTION 3) 61
FIGURE 78 – FEM RESULT OF THE FIRST STATIC STRENGTH ANALYSIS OF THE CRANKSHAFT 62
FIGURE 79 - CRITICAL ZONE OF THE INTERNAL PART OF THE POSTERIOR CRANK PIN FOR A CRANK ANGLE OF 374° 62
FIGURE 80 – PATH USED FOR THE EXTRACTION OF THE VON MISES STRESS 63
FIGURE 81 – VON MISES STRESS IN THE CRITICAL ZONE OF THE CRANK; VON MISES 1 IS THE STRESS CARRIED OUT FROM THE FIRST ANALYSIS, WHILE VON MISES 2 IS THE STRESS CARRIED OUT FROM THE SECOND ANALYSIS, AFTER THE CHANGE OF THE INTERNAL RADIUS 63
FIGURE 82 – FILLET RADIUS ZONE OF THE PIN OF THE POSTERIOR CRANK THAT SHOWS A VON MISES STRESS HIGHER THAT THE YIELDING LIMIT; MOREOVER, THE PATH USED FOR THE STRESS EXTRACTION IS SHOWN 64
FIGURE 83 – VON MISES STRESS ALONG THE PATH ON THE FILLET OF THE PIN OF THE POSTERIOR CRANK VERSUS THE YIELDING LIMIT 64
FIGURE 84 – CRITICAL NOTCHED ZONE OF THE CENTRAL PART OF THE CRANKSHAFT FOR A CRANK ANGLE OF 374° 65
FIGURE 85 – MAXIMUM PRINCIPAL STRESS CONCENTRATED IN THE NOTCH OF THE CENTRAL PART OF THE CRANKSHAFT FOR A CRANK ANGLE OF 374° 65
FIGURE 86 – MINIMUM PRINCIPAL STRESS CONCENTRATED IN THE NOTCH OF THE CENTRAL PART OF THE CRANKSHAFT FOR A CRANK ANGLE OF 374° 66
FIGURE 87 – VON MISES STRESS IN THE CRITICAL ZONE OF THE CENTRAL PART OF THE CRANKSHAFT, HIGHER THAN THE YIELDING LIMIT EVEN AFTER THE INCREASING OF THE FITTING RADIUS 66
FIGURE 88 – RESULTS OF THE FEM SLIPPING ANALYSIS IN TERMS OF CONTACT STATUS (CSTATUS) 67
FIGURE 89 – DETAILED VIEW OF THE CSTATUS OF THE PIN OF THE POSTERIOR CRANK (LEFT) AND OF THE PIN OF THE ANTERIOR CRANK (RIGHT) 67
FIGURE 90 – CAMPBELL DIAGRAM 69
FIGURE 91 – SECTION VIEW OF THE JOINT AMONG THE PISTON AND THE ROD, THANKS TO THE PIN (BLACK COMPONENT) 70
FIGURE 92 – IMPORTED ROD (1) AND DRAWN PIN (2) USED IN THE FE MODEL OF THE CONNECTING ROD 70
FIGURE 93 – ASSEMBLED MODEL OF THE CONNECTING ROD AND THE PIN 71
FIGURE 94 – INTERACTION DEFINED WITHOUT FRICTION AMONG THE PIN AND THE CONNECTING ROD 72
FIGURE 95 – SECTION VIEW OF THE CONNECTING ROD IN ABAQUS, WITH THE TWO REFERENCE POINTS (RED DOTS) AND THEIR RELATED SURFACES (RED DASHED LINES) 72
FIGURE 96 – SECTION VIEW OF THE PIN IN ABAQUS, WITH THE REFERENCE POINT (RED DOT) AND THEIR RELATED SURFACE (RED SURFACE) 73
FIGURE 97 – BOUNDARY CONDITIONS APPLIED ON THE ROD; ON THE LEFT THE HINGE WITH U1, U2, U3 CONSTRAINED AND ON THE RIGHT THE ROLLER WITH U1 AND U3 CONSTRAINED 73
FIGURE 98 – BOUNDARY CONDITIONS APPLIED ON THE PIN 74
FIGURE 99 – SECTION VIEW OF THE FE MODEL WITH THE BOUNDARY CONDITIONS AND THE LOAD APPLIED IN THE MAXIMUM COMPRESSION AT STARTING CASE 75
FIGURE 100 – ZOOM ON THE FINE MESH OF THE ZONE OF INTEREST 75
FIGURE 101 – FORCE GENERATED BY THE PRESSURE IN THE COMBUSTION CHAMBER AS A FUNCTION OF THE CRANK ANGLE 76
FIGURE 102 – VON MISES STRESS RESULTS OF THE FEM ANALYSIS PERFORMED ON THE ROD IN THE MAXIMUM COMPRESSION CASE 76
FIGURE 103 – PATH USED FOR THE EXTRACTION OF THE VON MISES STRESS IN THE MOST CRITICAL ZONE OF THE ROD 77
FIGURE 104 – TREND OF THE VON MISES STRESS VERSUS THE YIELD STRENGTH ALONG THE PATH 77
FIGURE 105 – LAYOUT OF THE ROD WITH THE BUSHING BEARING COUPLED WITH THE HEAD OF THE ROD 78

FIGURE 106 – MODEL OF THE BUSHING BEARING CREATED IN ABAQUS 79
FIGURE 107 - SECTION OF THE REFERENCE BUSHING BEARING MADE OF K-796 AND PRODUCED BY KING (SOURCE: HTTP://WWW.KINGBEARINGS.COM/CATALOG/) 79
FIGURE 108 – RESULTS OF THE FEM FRETTING ANALYSIS IN TERMS OF CONTACT STATUS (CSTATUS) 80
FIGURE 109 – ELECTRIC GENERATOR 81
FIGURE 110 – STATOR OF THE ELECTRIC GENERATOR WITH THE CRITICAL COMPONENTS 82
FIGURE 111 – COMPONENTS THAT TAKE PART TO THE ASSESSMENT ON THE STATOR 82
FIGURE 112 – COMPONENTS USED FOR THE ASSESSMENTS IN ABAQUS; THE SCREW (1), THE COVER PLATE (2) AND THE MAGNETS CARRIER (3) 83
FIGURE 113 – ASSEMBLED MODEL OF THE STATOR IMPLEMENTED IN ABAQUS 84
FIGURE 114 – BOUNDARY CONDITIONS AND BOLT LOAD POSITION IN THE SCREW MODELLED IN ABAQUS 85
FIGURE 115 – ELEMENTS TYPE USED FOR THE DIFFERENT COMPONENTS; THE GREEN AND YELLOW AREAS INDICATE THE C3D20R ELEMENTS, WHILE THE PINK AREAS INDICATE THE C3D10 ELEMENTS 86
FIGURE 116 – MESHED MODEL OF THE STATOR 86
FIGURE 117 – RESULTS IN TERMS OF PEEQ OF THE PLASTIC ANALYSIS PERFORMED ON THE STATOR 87
FIGURE 118 – RESULTS IN TERMS OF CSTATUS OF THE SLIPPING ANALYSIS PERFORMED ON THE STATOR 88
FIGURE 119 – EXAMPLE OF THE REPORT FILE EXTRACTED FROM ABAQUS WITH THE STRESS VALUES IN EACH NODE (FOR THE FIRST 10 NODES) 89
FIGURE 120 – FORCES ON THE CRANKSHAFT AS A FUNCTION OF THE CRANK ANGLE 92
FIGURE 121 - RESULTS OF THE FATIGUE ASSESSMENT PERFORMED ON THE POSTERIOR CRANK; THE BLACK DASHED LINE INDICATES THE RELIABLE RESULTS 94
FIGURE 122 – REFINED MESH WITH C3D20R ELEMENTS OF THE CRITICAL PART OF THE POSTERIOR CRANK 95
FIGURE 123 – RESULTS OF THE FEM ANALYSIS PERFORMED FOR THE TWO CRANK ANGLES OF 374° (LEFT) AND 14° (RIGHT) 95
FIGURE 124 – EQUIVALENT STRESS USED FOR THE SINES CRITERION IN THE CRITICAL ZONE OF THE POSTERIOR CRANK 96
FIGURE 125 – RESULTS OF THE FATIGUE ASSESSMENT PERFORMED ON THE ANTERIOR CRANK; THE BLACK DASHED LINE INDICATES THE RELIABLE RESULTS 96
FIGURE 126 - SAFETY FACTORS BETWEEN 1 AND 1.5 OF THE NODES OF THE POSTERIOR CRANK 97
FIGURE 127 – SAFETY FACTORS BETWEEN 1 AND 1.5 OF THE NODES OF THE ANTERIOR CRANK; THE BLACK DASHED LINE INDICATES THE RELIABLE RESULTS 97
FIGURE 128 – CRITICAL ZONES FOR THE FATIGUE LIFE OF THE POSTERIOR AND ANTERIOR CRANKS 98
FIGURE 129 – FORCE ON THE ROD @ 4000 RPM AS A FUNCTION OF THE CRANK ANGLE 98
FIGURE 130 – GRAPHIC RESULT OF THE FATIGUE ASSESSMENT ON THE ROD 99
FIGURE 131 - SAFETY FACTORS OF THE FATIGUE ASSESSMENT OF THE ROD; THE RED POINTS REPRESENT THE VALUES WITHIN THE MINIMUM SAFETY FACTOR (1.45) AND 2 99

List of tables

TABLE 1 – PRINCIPAL DATA OF THE TWO RE ICE USED FOR THE CHEVROLET VOLT AND FOR THE BMW I3 4
TABLE 2 – MAIN SPECIFICS OF THE INTERNAL COMBUSTION ENGINE 9
TABLE 3 – MECHANICAL PROPERTIES OF THE 18NICRMO5 CARBURISING STEEL 11
TABLE 4 – MECHANICAL PROPERTIES OF THE 39NICRMO3 HARDENING AND TEMPERING STEEL 12
TABLE 5 – FUEL CONSUMPTIONS COMPARISON AMONG RME RANGE EXTENDER AND BMW 16
TABLE 6 – DATA AND RESULTS OF THE CALCULATION OF MASSES CONTRIBUTION OF THE ROD 19
TABLE 7 – DATA USED TO DETERMINE THE INERTIA OF THE PISTON 20
TABLE 8 – DATA AND RESULTS OF CALCULATIONS OF THE ROTATIONAL INERTIA FORCES 21
TABLE 9 – MEANING OF THE SYMBOLS 22
TABLE 10 – DIMENSIONS OF THE CRANKSHAFT'S MODEL 27
TABLE 11 – RESULTS OF THE ANALYTIC CALCULATIONS ON THE HUB AND ON THE SHAFT 33
TABLE 12 – RESULTS OF THE FIRST FEM ANALYSIS 41
TABLE 13 – RESULTS OF THE SECOND FEM ANALYSIS 41
TABLE 14 – CONTACT PRESSURE ON THE CONTACT SURFACE OF THE HUB 43
TABLE 15 – VALUES OF THE FORCES OF THE CRITICAL CASES 44
TABLE 16 – MATERIAL PROPERTIES USED FOR THE FEM ANALYSIS OF THE CRANKSHAFT 47
TABLE 17 – CRANK ANGLES USED FOR THE DIFFERENT ANALYSIS 52
TABLE 18 – VALUES OF THE LOADS USED IN THE DIFFERENT FEM ANALYSIS 52
TABLE 19 – BENDING MOMENT VALUES ALONG THE CRANKS DUE TO THE CENTRIFUGAL FORCES 55
TABLE 20 – BENDING MOMENTS ALONG THE CRANKS FOR THE CRANK ANGLES OF 14° AND 25° 56
TABLE 21 – BENDING MOMENTS ALONG THE CRANKS FOR THE CRANK ANGLES OF 374° AND 385° 57
TABLE 22 – TOTAL BENDING MOMENTS ALONG THE CRANKS THAT ACT IN THE Y-Z PLANE 57
TABLE 23 – VALUES OF THE BENDING MOMENT IN THE X-Z PLANE FOR THE CRANK ANGLES OF 14° AND 25° 59
TABLE 24 - VALUES OF THE BENDING MOMENT IN THE X-Z PLANE FOR THE CRANK ANGLES OF 374° AND 385° 59
TABLE 25 – VALUES OF THE EQUIVALENT BENDING MOMENTS ALONG THE CRANKS FOR ALL THE CRANK ANGLES 60
TABLE 26 – PROPERTIES OF SECTION 3 61
TABLE 27 – EIGEN-FREQUENCIES OF THE FIRST 5 VIBRATIONAL MODES OF THE CRANKSHAFT 68
TABLE 28 – MODAL SHAPES OF THE CRANKSHAFT 68
TABLE 29 – MATERIAL PROPERTIES OF THE CONNECTING ROD 71
TABLE 30 – LOAD CASES AND ASSESSMENTS FOR WHICH THEY HAVE BEEN USED 74
TABLE 31 – VALUES OF THE LOADS USED IN THE DIFFERENT LOAD CASES 74
TABLE 32 – ELASTIC PROPERTIES OF THE BUSHING BEARING USED FOR THE FEM ANALYSIS 80
TABLE 33 – PROPERTIES OF THE MATERIALS USED FOR THE FE MODEL OF THE STATOR 83
TABLE 34 – PARAMETERS OF THE M8 SCREWS CLASS 6.6 ACCORDING TO THE STANDARD UNI 4535-64 85
TABLE 35 – MATERIAL DATA OF BOTH THE CRANKSHAFT AND THE ROD USED FOR THE FATIGUE DESIGN 90
TABLE 36 – VALUES OF THE FORCES THAT ACTS ON THE CRANKSHAFT FOR THE SELECTED LOAD CASES 93
TABLE 37 – DEFORMED SHAPES OF THE CRANKSHAFT FOR THE LOAD CASES ANALYSED WITH THE FEM 93
TABLE 38 – RESULTS OF THE FATIGUE ASSESSMENT IN THE CRITICAL ZONE OF THE POSTERIOR CRANK 95
TABLE 39 – FORCE USED FOR THE FATIGUE ASSESSMENT ON THE ROD 98

1 Abstract

The present work is based on the cooperation between Polytechnic of Milan and Robby Moto Engineering S.r.l., whose object is the development of a new internal combustion engine used as range extender on electric vehicles. The principal activities done and here explained concern the assessments and the dimensioning of the principal components of the range extender, such as the crankshaft, the connecting rods and the stator of the electric generator. Both static and fatigue assessments have been performed on the crankshaft and on the connecting rods, which are the most stressed components. The used criteria are the Von Mises and Guest-Tresca for the static assessments and the Sines one for the fatigue assessments. Moreover, the crankshaft is composed by three pieces, that are joined by interference fit coupling, so the tolerances have been selected. The stator of the electric generator, that is made of aluminium 6060, is composed by two pieces connected by a friction bolted joint, so it has been necessary to perform an elastic-plastic analysis on the threaded holes and a slipping analysis of the friction joint.
All the components have been analysed with the fundamental help of computer aided engineering (CAE), which today is widely used for the stress analysis phase, allowing to reduce the testing costs.

2 Introduction

The present master thesis work is based on the project of an innovative internal combustion engine, whose purpose is to act as a range extender for the electric vehicles. The range extender is a device which comprises an engine and an electric generator. The engine is aimed at charging the electric battery by driving the electric generator connected to his output shaft.
The project, that is financed by the Lombardia region, started on March 2017 and its end is scheduled for March 2019. The involved participants are three and they are Robby Moto Engineering S.r.l. which is the project coordinator, ACM-Engineering S.r.l. and Meta System S.p.a.. Each one of these firms has its own field of application in the range extender development: Robby Moto Engineering S.r.l. deals with the internal combustion engine, ACM-Engineering S.r.l. deals with the electric generator and Meta System S.p.a. deals with the electronics. Polytechnic of Milan has collaborated to this project by assessing the mechanical design of the components and suggesting changes in case of negative result of the assessments. In this thesis, the work done by Polytechnic of Milan is reported.
In particular, in this thesis is reported the work done in order to assess the components of the internal combustion engine, that have been initially designed by the staff of Robby Moto Engineering S.r.l.. This was necessary because most of the components are novel and so both static and fatigue assessments have been performed on them. The novelty of this engine comes from the fact that it has been conceived to suit the role of range extender. Indeed, the criteria used for the design are the fluid dynamic optimization at a constant rotational speed, the compactness, the lightness and the lowest environmental impact.
The principal tasks done and here explained are related to the mechanical design of some of the principal components of the range extender. The design activities are related to the selection of some tolerances, the static assessments and the fatigue assessments. All of them have been performed with the help of the finite element software Abaqus, and the fatigue assessments also with the help of MatLab. In particular, the analysed components are the crankshaft, the connecting rods and the stator of the electric generator. Concerning the crankshaft, the first thing to do has been the selection of the tolerances for the interference fit and then the static and fatigue assessments have been performed. Even a modal analysis has been done on the crankshaft, for being sure that it works far from resonance conditions. On the connecting rod, the static and the fatigue assessments have been done, and even a fretting analysis. The stator of the electric generator has been analysed because is made of aluminium 6060 and it is composed by two pieced connected by a friction bolted joint. Thus, an elastic-plastic analysis of the threaded holes and a slipping analysis have been done. The computer aided engineering (CAE) has had a fundamental role in all the assessments, allowing a very detailed stress analysis even in the most complex geometry.

3 State of the art

3.1 Range extender in automotive field

A range extender (RE), in the automotive field of application, is a device that increases the range of the battery electric vehicles (BEV), in terms of duration of the battery and consequently in terms of the distance that can be covered. Indeed, one of the main hindering factor in the BEV commerce is the range autonomy of the electric battery, that limits the usage and the sales of such vehicles.
The range extender is an engine, usually an internal combustion engine (ICE), that drives an electric generator, in order to produce electric power for charging the battery that powers the electric motor of the car. This layout is named series hybrid drivetrain (Figure 1) and it is typical of the range-extended electric vehicles (REEV).

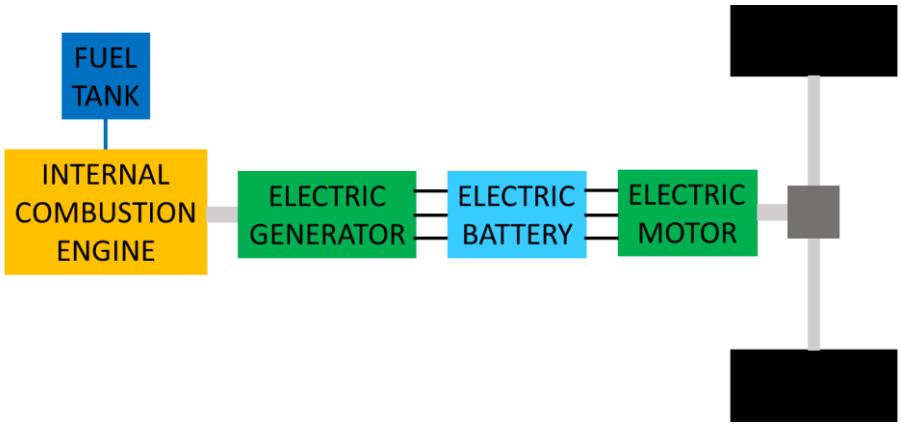

Figure 1 - Conceptual layout of a series hybrid drivetrain implemented on a range extended electric vehicle

In the REEVs the power to the wheels is entirely provided by the electric motor, and the range extender starts when the battery charge level goes below a certain limit, for example the 30%, acting like a reservoir in the common internal combustion engine vehicles. For these vehicles, the primary fuel is therefore the electric energy stored in the battery, while the petrol or the gas are the secondary fuel, to be used only if necessary.
Today, on the market there are some range-extended electric vehicles, such as the Chevrolet Volt and the BMW i3 (Figure 2).



Figure 2 – 2012 Chevrolet Volt (1) and New BMW i3 (2)

These two cars, that are very different from each other, use, as RE, internal combustion engines derived from existing ones. In particular, the Chevrolet Volt uses the four cylinders in-line petrol engine developed by Opel and already mounted on some cars like the “Opel

Corsa" without any variation, while the BMW i3 uses the two cylinders in-line petrol engine developed by BMW and mounted on the scooter BMW C 650, but with a maximum power reduction. The principal data of the two engines are reported in the following table (Table 1).

Table 1 – Principal data of the two RE ICE used for the Chevrolet Volt and for the BMW i3

Car	Displacement	Configuration	Power
Chevrolet Volt	1398 cm^3	4 in-line	63 kW (84 hp) @ 4800 rpm
BMW i3	647 cm^3	2 in-line	25 kW (34 hp) @ 4300 rpm

These two ICE are both characterized by the same origin that is the traction field of application. Indeed, they were born for being mounted on ground vehicles, where they provide the power to the wheels. Thus, they can be used in a quite wide range of regimes, from the minimum to the maximum. Moreover, they are designed for a quite high power, feature that affects their weight and their dimensions.

The characteristics of the actual internal combustion engines used as RE, like those reported above, have created the conditions for the need of a new concept of range extender designed on this specific purpose. The principal design criteria are the lightness and the compactness, as well as the infinite life duration (with reference to the fatigue design). The infinite life and the lightness are two opposite concepts, and their implementation in the same project requires a deep analysis of the principal components in terms of stresses. Another important concept is the environmental impact, both in terms of emissions and in terms of used materials.

Concerning the emissions, the engine has to be optimized, from a fluid dynamics perspective, at a specific rotational speed, the one for which the group composed by the ICE and the electric generator have been designed. In this way it should be possible to reduce the fuel consumption for a given nominal power to provide.

The choice of the materials should be done for reducing as much as possible the environmental impact. This can be obtained by the usage of thermoplastic materials for the low loaded components, like the water ducts, the cylinders head covers and the oil sump. This material carries benefits both to the lightness of the engine and to the environment, respectively thanks to its low density and high recyclability. Moreover, it is important to highlight that the fuel consumption of a car is directly proportional to his weight, so the lightness is bonded to environmental impact.

3.2 Design of an internal combustion engine outline

The design of an internal combustion engine is a procedure that requires a systematic analysis of the involved phenomena. Indeed, due to the high safety and emission standards needed, it is no more possible to base the decisions only to the common sense. Today, the use of sophisticated computational systems, like the CAD and FE softwares, is mandatory in the design phase, for better understanding the feasibility of the manufacturing processes and for performing the structural analysis. Moreover, the market researches are of an always increasing relevance before starting the design and production of a brand-new engine. The targets of such research are the competitors, for understanding how they are proceeding in the market, and the possible customers, for ensuring that the new project will be of their interest.
However, there are some basic considerations that have to be taken before all the other phases of the project, that can be summarized in the followings:

- Motivation of the new project
- Type of utilization of the engine
- Power and fuel consumption requirements
- Layout of the engine (number and arrangement of the cylinders, naturally aspired or turbocharged, etc…)
- Fuel type
- Development cost estimation
- Production time estimation
- Production cost estimation
- Market evaluations

From a structural point of view, it is important that the components of the engine can resist to the high forces involved in the operating phase, given by the pressure in the combustion chamber, the inertia forces, the thermal expansion and so on. Once that that the integrity of the components is ensured, it is necessary to proceed with a more detailed analysis for removing the material where is not needed, in order to reduce the total weight. Indeed, the material of an ideal structure should be distributed in such a way that it undergoes the same stress in all its points for a fraction of the yielding limit, defined by the safety factor. This is an ideal situation, because in the reality the degree of perfection is always a good compromise among the cost and the level of the structure needed.
Concerning the possible failures of an engine, the principal cause is, as in most of the cases, due to the fatigue of the components. This kind of failure is caused by the cyclic loading conditions and usually the starting points of the fractures are the notches, where the stresses are concentrated. The evaluation of the stresses is an operation that is complicated by the uncertainty of the loads and their distribution. Indeed, even if the loads generated by the gasses can be easily calculated, their value can change during time and, since the structure is flexible, they can be increased by flexion and vibrations. Moreover, the distribution of such loads in a lot of the engine zones depends on too complex elastic phenomena for being easily evaluated.
For these reasons, the design of the engine's components has had an almost totally empiric development during the years, assisted by analytic calculations and experimental tests. The introduction of the finite element method has simplified a lot the design of the mechanical components, but the testing procedure is still mandatory.

The components of the engine that are mostly stressed are for sure the connecting rods and the crankshaft, and so their design requires an accurate analysis and assessment.

3.2.1 The crankshaft

The crankshaft is the component that, together with the rods, converts the alternating motion of the pistons into a rotary motion, and sends the power to the user, such as the transmission or, in the case of this thesis, the electric generator. Usually, the crankshaft is monolithic, except for some 2 strokes engine that needs the roller bearings for the rod's heads, that otherwise cannot be mounted. In Figure 3 a crankshaft used in a 4 cylinders engine of a car is illustrated, and its main parts are indicated. The main bearing journals are the points in which the component is constrained to the crankcase, the crankpin journals are the connection points among the crankpins and rods, the balance mass are counterweights for damping the vibrations and compensating the centrifugal forces, and finally the flywheel mounting flange is the part at which the flywheel is joined to the crankshaft.

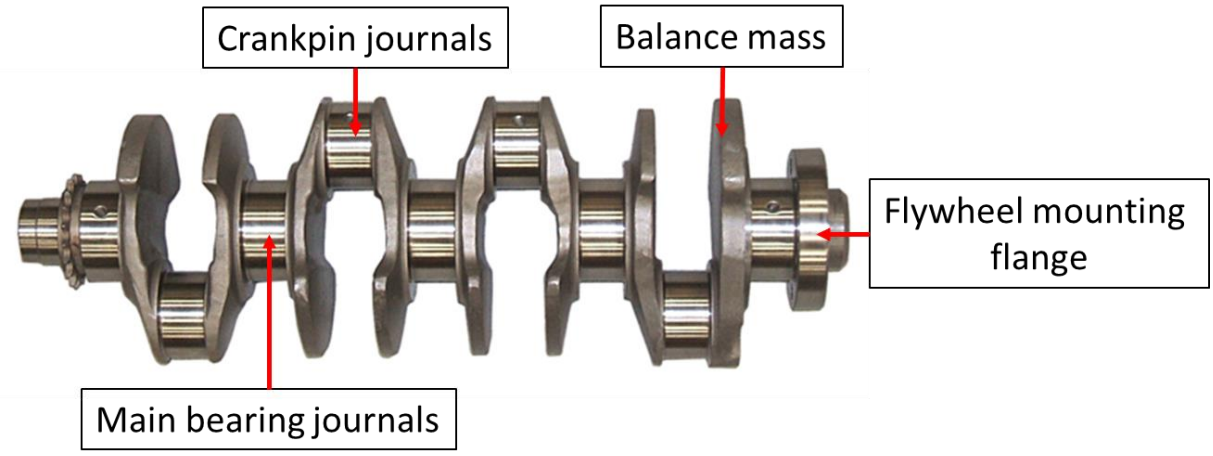

Figure 3 – Example of a monolithic crankshaft and its main parts (source: http://www.eurospecsport.com/products/components/performance-crankshafts.htm)

The crankshaft undergoes to both static and alternating stresses, the first due to the inertia forces and the second due to the pressure generated in the combustion chamber. Moreover, since it is a rotating component, it must weight as little as possible. Due to these reasons, the crankshafts are in most of the cases made of high strength steels, such as the 18NiCrMo5 carburising steel. However, for maximizing the fatigue life it is important to avoid the stress concentrations, thus the attention must be focused on the fillet radius among the crankpins and the crankwebs (the crankwebs are the parts that connect the crankpin to the main bearing journal and then they develop into the balance masses) and on the surface finishing of the crankpins (their surface roughness Ra is of about 0.2 μm). In the zones in which there is relative movement among the components, such as the journals, it is necessary to bring lubrication oil. This task can be performed thanks to appropriate holes, that allow to carry the oil from the axial extremity of the crankshaft to the journals, thanks to the centrifugal force.

3.2.2 The connecting rod

The connecting rod (or simply the rod) is the component that connects the crankpin with the piston pin, allowing together with the crankshaft to transform the alternating motion of

the piston into the rotary motion of the crankshaft. In Figure 4 an example of a connecting rod used for monolithic crankshaft is shown. This kind of rod, has a dismountable rod cap, that allows to connect the rod head to crankpin of the crankshaft. Even the rod bearing is composed by two semi-bearing, that must be positioned in the internal surface of the rod head during the mounting phase. If a composite crankshaft (characterized by more than one components) is used, for example in a two strokes engine, the rod is monolithic, because it can be mounted coupled to the crankpin before assembling the crankshaft. The small end of rod foot, is coupled with the piston by means of the piston pin.

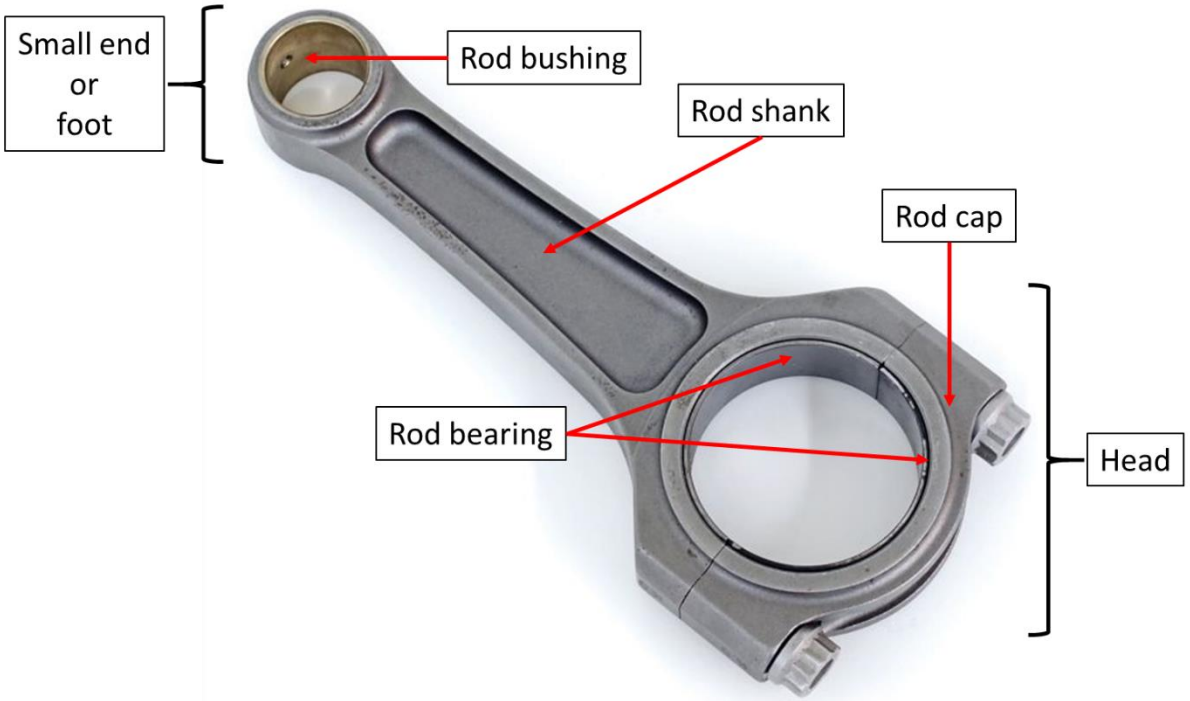

Figure 4 – Example of a connecting rod used for monolithic crankshaft and its main parts (source: https://www.sicurauto.it/tecnica/news/che-cosa-e-la-biella-e-come-e-fatta.html)

The rod shown in Figure 4 is produced by the printing manufacturing process, and due to this it is more economically convenient respect to others. Indeed its section has not any undercuts, allowing the printing process. Other geometries for the rods are adopted in the racing field of application.
The holes of the foot and of the head are used for coupling the connecting rod respectively to the piston pin and to the crankpin, thus relative motion is present, requiring lubrication. The lubricating oil is carried to the hole of the foot by means of one or two holes drilled in the superior part of the ring, that allow to the oil present in the bottom part of the piston to flow down in the interface among the piston pin and the bushing. Moreover, the continuous movement of the piston pin brings the oil all over the contact surface for improving the lubrication. The coupling among the head of the rod and the crankpin is lubricated by the oil carried by the holes in the crankshaft, thanks to the centrifugal force.

4 The RME range extender

In this chapter the principal features of the range extender developed by the Robby Moto Engineering (RME) in collaboration of Polytechnic of Milan will be illustrated and explained, focusing the attention on the novelty of the components.
The range extender object of this thesis is composed by and internal combustion engine that drives an electric generator. The architecture of the system is shown in Figure 5, where the two macro components (engine and generator) are highlighted. It is also possible to see that the electric generator is rigidly constraint directly to the internal combustion engine, increasing the compactness of the range extender. Indeed, the objective of the project was to create an independent system, which can be treated as a single module, in order to make easier its embedment in the electric vehicles.

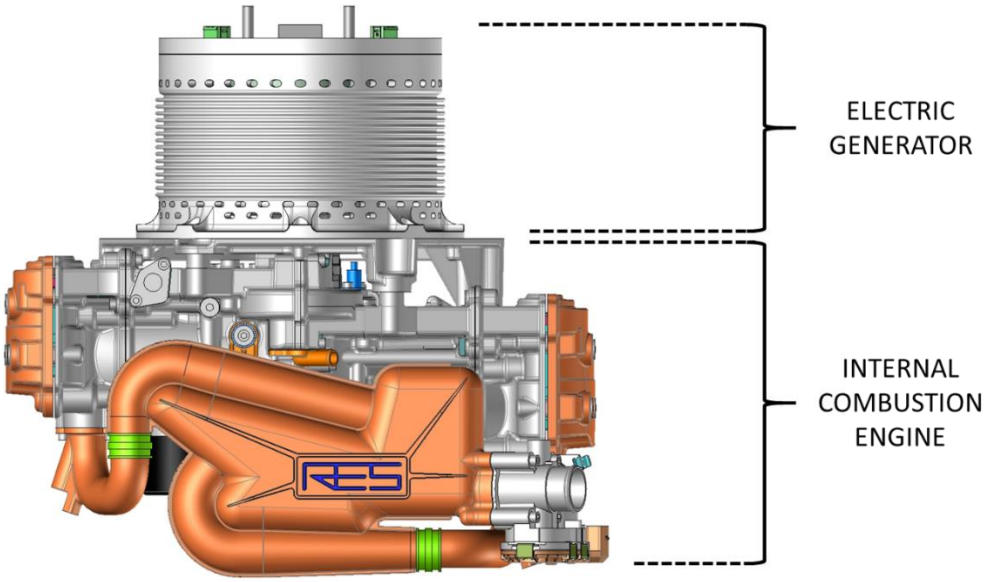

Figure 5 – RME range extender

4.1 The electric generator

The electric generator is the device that converts the mechanical power coming from the internal combustion engine into electric power for charging the batteries. It is basically composed by a rotor and a stator. The rotor is connected to the output shaft of the engine by means of a conic coupling, and carries the windings making them rotate respect to the magnets, that are located on the stator. The stator is fixed with the engine, and on it the magnets are located.
Concerning the choice of the electric generator, the starting hypothesis were two, both about the stator-rotor relative position. Indeed, the available architectures are those with the external stator and internal rotor and with the external rotor and internal stator. The selected solution has been fallen upon the one with the external rotor, because, despite it is more complex than the other one from both a manufacturing and heat dissipation point of view, it is advantageous in terms of axial size reduction (its volume develops more in the radial direction), the external rotor acts as a fly wheel for the engine allowing a weight saving and it simplifies the embedment of the control electronics directly inside the machine.

4.2 Internal combustion engine

The design and development of the internal combustion engine has been the main task of the Robby Moto Engineering in collaboration with Polytechnic of Milan.
The aim of the engine is to move the rotor of the electric generator for providing electric power to the batteries when their residual charge level goes below a predefined level, for extending the range of the electric vehicle. Due to this reason, the required features for this engine are the compactness, the lightness, as noiseless as possible, low vibrational and of course the cheapness. To meet these characteristics, the choice has been fallen upon a petrol powered flat-twin boxer engine architecture, a displacement of 500 cm^3 and able to provide 20 kW at a regime of 4000 rpm to the electric generator.
The main characteristics of the present internal combustion engine are reported in the following table (Table 2).

Table 2 – Main specifics of the internal combustion engine

Main specifics of the internal combustion engine	
Stroke	72 mm
Bore	61.4 mm
N° of cylinders	2
Architecture	Boxer
Displacement	499.98 cm^3
Nominal power	20 kW
Nominal speed	4000 rpm
Distribution	Camshaft with two valves per cylinder
Cooling system	Liquid cooling
Fuel introduction	Direct injection

All these specifics allow to meet the needed characteristics, making the present project interesting if compared to the state of the art range extenders. In Figure 6 a section view of the internal combustion engine is illustrated, also showing the width and the depth.

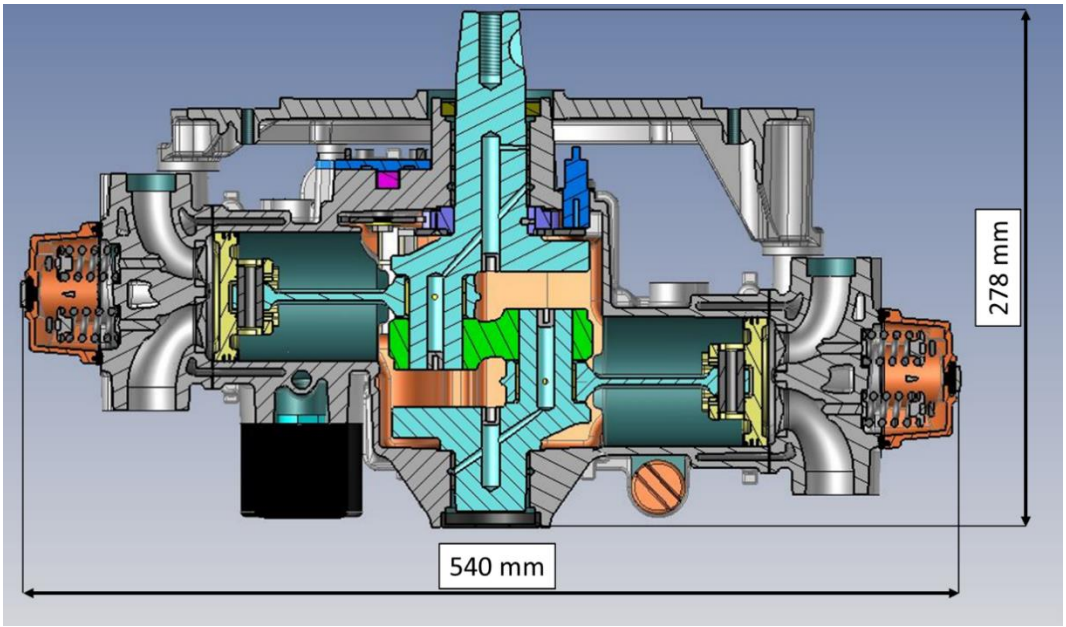

Figure 6 - Section view of the internal combustion engine with the width and depth values

4.2.1 The crankshaft

The crankshaft of the engine object of this work (Figure 7) is quite different from the common monolithic crankshafts, usually used for the four strokes internal combustion engine. Indeed, it is composed by three different components instead of being monolithic. This choice has been done after a cost forecasting, from which it has been resulted convenient to adopt this layout.

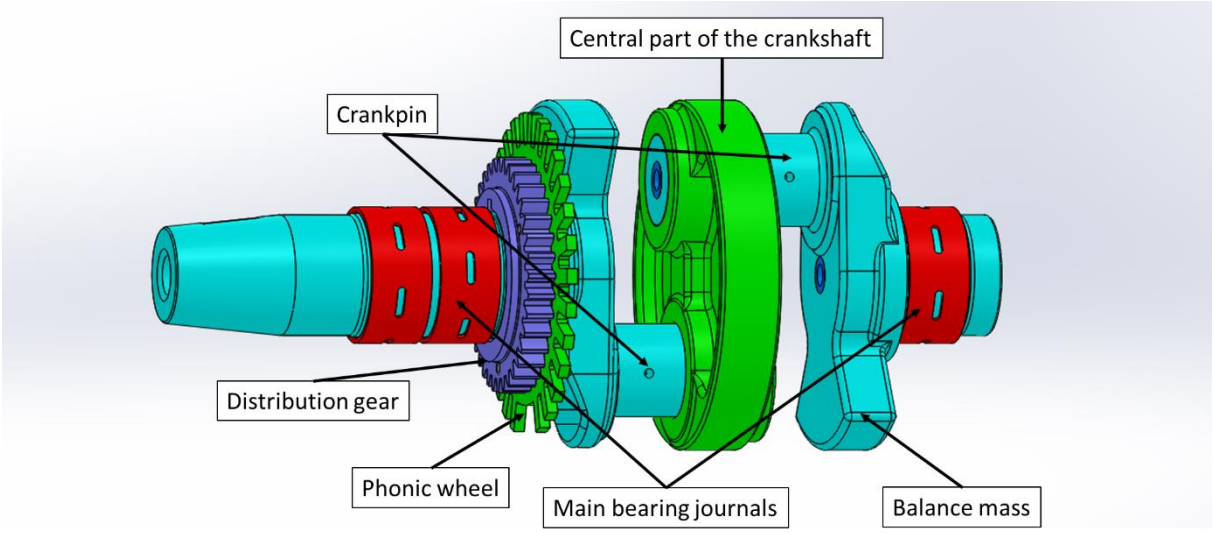

Figure 7 – Crankshaft

The three components that compose the structure of the crankshaft are the posterior crank, the anterior crank and the central part of the crankshaft, as shown in Figure 8. The two cranks, the posterior and the anterior, are connected to the central part of the crankshaft by means of an interference fit. The coupling involves the crankpins and the holes of the central part, that are dimensioned for ensure the needed interference. The interference fit has been designed by looking at the maximum torque that flows through the coupling, that is given by the pressure peaks in the combustion chamber.

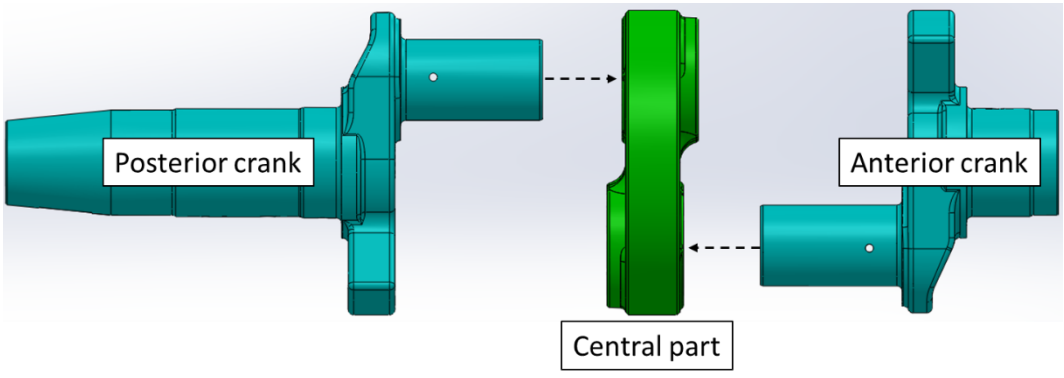

Figure 8 – Three components of the crankshaft structure

The solution of adopting a composite crankshaft instead of a monolithic one, is possible only because the power produced by the engine is relatively low (about 20 kW @ 4000 rpm) and consequently also the average torque is relatively low (about 48 Nm @ 4000 rpm). However, the problem that can arise using an interference fit coupling is the slipping among the two involved surfaces. Indeed, along the crankpins, it is not only the torsion

that is flowing through, but also the bending due to the force transmitted by the rods. The combination of torsion and bending can create a condition in which the friction among the surfaces is no more sufficient to keep them constrained, causing wearing and even a misalignment of the axis of the three components. Anyway, thanks to the finite elements method, it is possible to simulate the worst condition, that with the minimum interference and the maximum torsion, for predicting the behaviour of the coupling.
The material of which the crankshaft is made of is the 18NiCrMo5 (according to the standard UNI 7846) carburising steel, which has good mechanical properties for this task. The mechanical properties of the 18NiCrMo5, used for the design of the crankshaft, are reported in Table 3, with reference to a specimen of a diameter equal to 30 mm, hardened and stress relieved.

Table 3 – Mechanical properties of the 18NiCrMo5 carburising steel

18NiCrMo5			
Parameter	**Name**	**Value**	**Unit**
Minimum yielding strength	σ_y	735	MPa
Ultimate tensile strength	UTS	980	MPa
Elongation at fracture	A%	9	-
Resilience	KCU	32.5	J

The conical extremity of the posterior crank is connected with the rotor of the electric generator, by means a conical coupling that requires about 5200 N of preloading (with a service factor equal to 2). On the other side of the crankshaft, at the extremity of the anterior crank, there is not any flywheel mounting flange, since the rotor acts as a flywheel, thanks to configuration of external rotor of the electric generator.
The lubrication of the journals is guaranteed by the oil ducts shown in Figure 9, where they have been highlighted in red. The oil input is located at the main journal bearing, where the pressurized oil pass through the bearings thanks to apposite holes, flowing inside the crankshaft. The exit points are located in the crankpins, where there are two holes per crankpin (obviously in the section view is shown only one per crankpin).

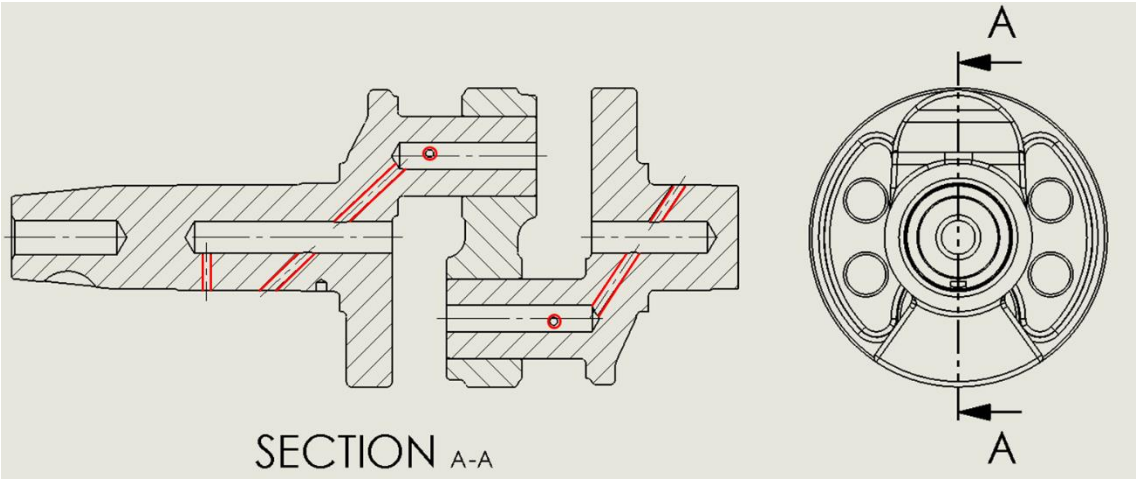

Figure 9 – Section view of the crankshaft with the drilled ducts for the lubricating oil are highlighted in red

4.2.2 The connecting rod

The connecting rods used in this internal combustion engine are monolithic, since the rod cap is no more necessary with a composite crankshaft. Indeed, the rod are mounted on the crankpin before mounting the crankshaft. In this way, it has been possible to save on the manufacturing costs and on the assembly time. The connecting rod, together with the components at which is connected, is illustrated in Figure 10.

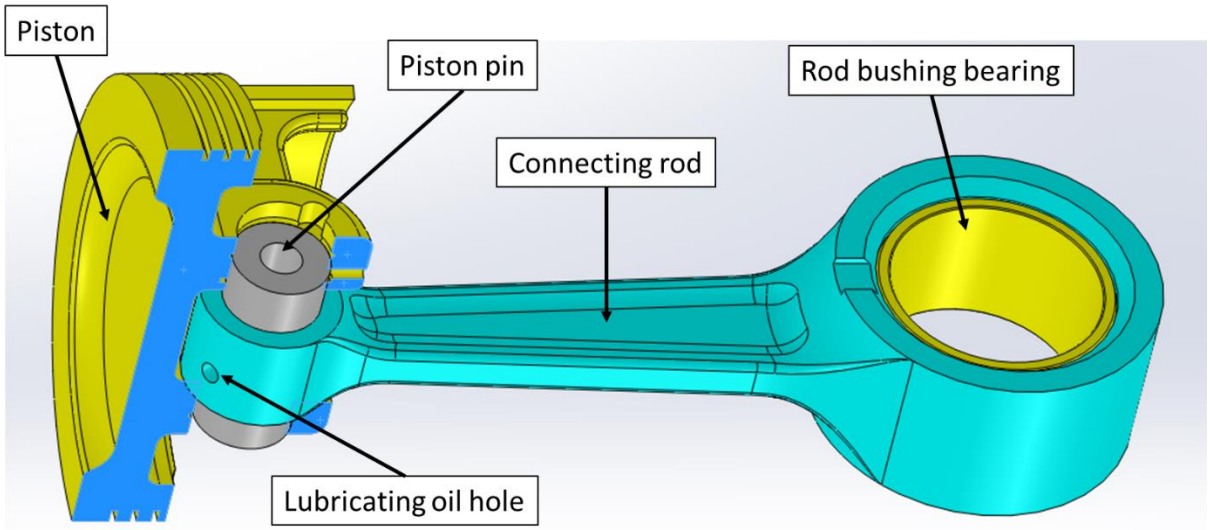

Figure 10 – Connecting rod

From Figure 10, it is possible to see that the connecting rod is monolithic, and that there is not a bushing in the rod foot. The oil film is directly interposed among the external surface of the piston pin and the internal surface of the rod foot. In the rod head, the bushing bearing is monolithic too, and it is forced inside the hole with a minimum interference of 20 μm (the bushings have not already been selected, so the interference range and the tolerances are not reported in this work).

The connecting rod is made of 39NiCrMo3 hardening and tempering steel, that does not undergo any surface treatment like shoot peening or carburization. Its mechanical properties are reported in Table 4 with reference to a specimen diameter of 16 mm.

Table 4 – Mechanical properties of the 39NiCrMo3 hardening and tempering steel

39NiCrMo3			
Parameter	**Name**	**Value**	**Unit**
Minimum yielding strength	σ_y	785	MPa
Ultimate tensile strength	UTS	980	MPa
Elongation at fracture	A%	11	-
Resilience	KCU	30	J

5 Design

5.1 Design for environment

The design for environment is a preliminary phase of the development of a new project, in which the environmental impact of the life cycle of the product is taken into consideration. The aim of this phase is to reduce as much as possible such environmental impact, for example using recyclable materials instead of the disposables, or using reversible joint method like bolted joints instead of welding joints and so on. Of course, it is not always possible to meet all the characteristics that an environmental friendly product should has, because of structural needed or manufacturing issues. It is always a trade-off between the production costs and the environmental impact.
During the development of the present internal combustion engine a lot of effort has been put into the selection of the materials, that must be as much as possible recyclable and light. Indeed, the most impact phase of the life cycle of an internal combustion engine is when it is operating, because of the fuel consumption and the pollutants emission. So, for reducing the environmental impact of the engine during this phase, it should weight as low as possible, feature that can be reached by using lightweight materials.
The principal materials of which the engine is made of are steel, aluminium and thermoplastic. They are all recyclable, and in addition, aluminium and thermoplastic are lightweight materials.

5.1.1 Qualitative material analysis

In this paragraph it is reported the list of the components of the internal combustion engine with the selected materials. The principal components have been clustered in three macro categories according to their material: the steel, the aluminium and the thermoplastic.

- Steel components: crankshaft, connecting rods, camshafts, rockers, gears, pistons, piston pins, timing chains, rotor of the oil pump, springs and screws
- Aluminium components: carters of the cylinders (engine block), cylinder's heads, camshaft's slots, cover of the oil pump, oil circuit cups
- Thermoplastic components: oil sump, cylinder's head covers, airbox, chain tensioner shoes, cooling water manifolds, oil cup with integrated stick

These three materials, of which almost the totality of components is made of, satisfy the recyclability parameter, which is one of the most important concerning the environmental impact. Moreover, the aluminium and the thermoplastic are lightweight materials, and they allow a weight reduction decreasing the fuel consumption and the emissions of pollutants. Among these components, there are three that see an unusual use of the thermoplastic: the oil sump, the cylinder's head covers and the cooling water manifolds. Both the oil sump and the cylinder's head covers are usually made of aluminium, so in this case a weight saving is reached, since keeping constant the volume of the components, the aluminium has density of about 2700 kg/m^3 while the thermoplastic has a density of about 1000 kg/m^3. The cooling water manifolds are usually made of rubber reinforced with steel wires, which is not as easily recyclable as the thermoplastic. In this way, their environmental impact it has been decreased. These three components are shown in Figure 11.

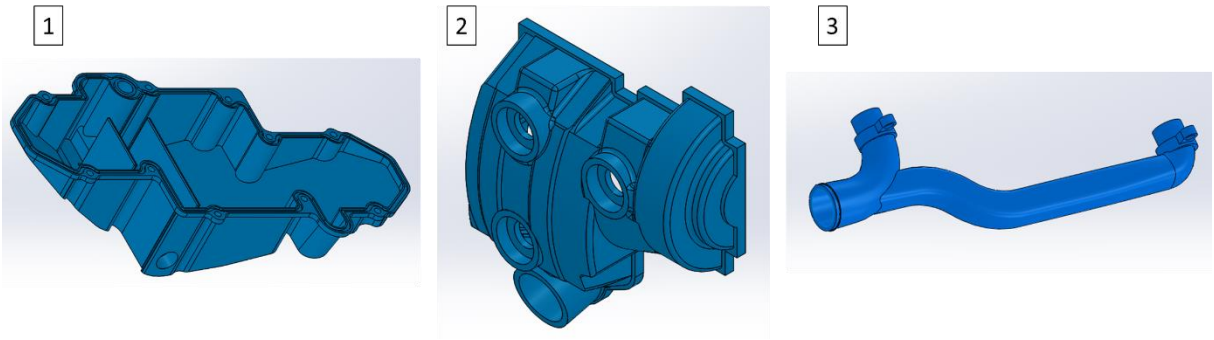

Figure 11 – Thermoplastic novel components; oil sump (1), right cylinder's head cover (2), inlet cooling water manifold (3)

5.1.2 Estimated increase of autonomy and comparison with BMW i3

In this paragraph, an estimation of the extension of the range autonomy is reported. For computing the range extension, the fuel consumption has been calculated in [km/l] for a speed at which the nominal power of the internal combustion engine, decreased of the efficiencies, equals the resistance power that acts on the moving vehicle. The fuel consumption has been calculated for such speed because the range extender can only work at the nominal speed, regime at which the nominal power is provided.
Since a concrete model of the RME range extender object of the present work does not already exist, some hypothesis has been guessed for the fuel consumption calculation.
The guesses are:

- Total mass of the vehicle: $m_{tot} = 1500\ kg$
- Drag coefficient of the vehicle: $C_x = 0.32$
- Frontal surface of the vehicle: $S = 2.3\ m^2$
- Friction coefficients: $f_0 = 0.01$; $f_2 = 6.48 \cdot 10^{-6}$
- Engine total efficiency: $\eta_c = 0.34$
- Lower heating value petrol: $LHV_{fuel} = 43300 \frac{kJ}{kg}$
- Petrol density: $\rho_{fuel} = 0.74 \frac{kg}{dm^3}$
- Ground slope: $\alpha = 0°$
- Electric efficiency: $\eta_{el} = 0.84$
- Mechanical efficiency: $\eta_{mecc} = 0.95$

With these assumptions, the resistance power as a function of the vehicle's speed has been computed, using the following formula:

$$P_R = m_{tot} \cdot g \cdot (sin\alpha + f_0 \cdot cos\alpha) \cdot v + \left(\frac{1}{2} \cdot \rho_{air} \cdot C_x \cdot S + f_2 \cdot cos\alpha \cdot m_{tot} \cdot g\right) \cdot v^3$$

In the graph of Figure 12 the trend of the resistance power as a function of the hypnotised vehicle's speed is reported.

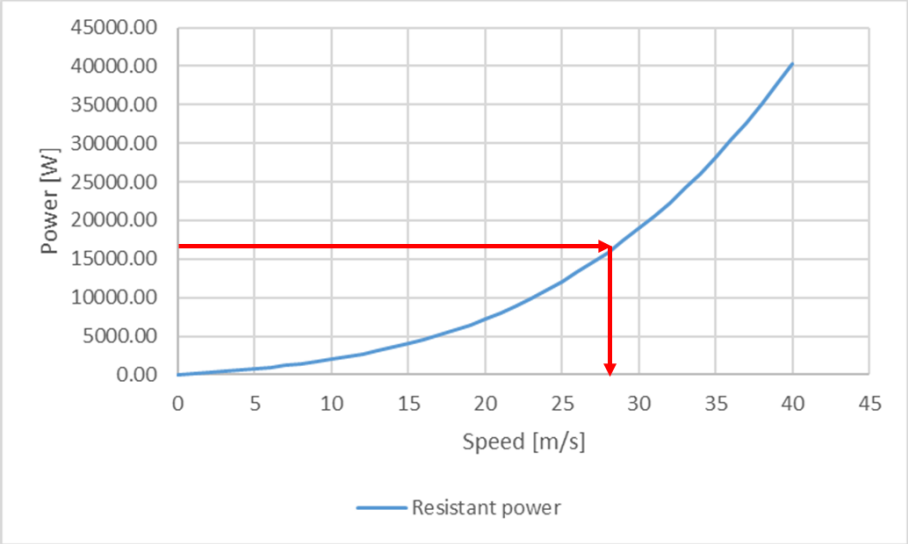

Figure 12 - Resistant power as a function of the vehicle's speed

The red arrows in Figure 12 represent the interpolation point for the speed determination. For finding the interpolation point it has been computed the power at the wheels of the vehicle, assuming that is entirely provided by the range extender (remember that the range extender can only charge the electric battery of the vehicle). So, this power comprises the efficiencies of the electric efficiency of the generator and of the electric motor (reported in a single value) and the efficiency of the differential (the transmission is useless on an electric vehicle) and it has been computed as follows:

$$P_{wheel} = \frac{P_{ICE}}{\eta_{el} \cdot \eta_{mecc}} = 16\ kW$$

Remembering that the nominal power at the output shaft of the internal combustion engine is equal to 20 kW at the regime of 4000 rpm.
The vehicle's speed that corresponds to such power is equal to v=28.5 m/s (102.6 km/h), and it will be used for calculated the fuel consumption in [km/l] starting from the volume flow rate of fuel.
Then, knowing the global efficiency of the engine, which comprises all the power losses during the transformation of the chemical energy of the fuel into the mechanical energy, it is possible to compute the combustion power:

$$P_{comb} = \frac{P_{ICE}}{\eta_c} = 58.8\ kW$$

From the power of the combustion, and knowing the lower heating value of the fuel, that in this case is petrol, the mass flow rate of fuel is:

$$\dot{m}_{fuel} = \frac{P_{comb}}{LHV_{fuel}} = 0.00136\ \frac{kg}{s}$$

Then, it is useful to switch to the volume flow rate, that has a more suitable unit of measurement for the final needed value of fuel consumption:

$$\dot{V}_{fuel} = \frac{\dot{m}_{fuel}}{\rho_{fuel}} = 0.00183 \ \frac{l}{s}$$

Finally, knowing the constant speed of the vehicles, for which this volume flow rate of fuel is needed, the fuel consumption in [km/l] is calculated in this way:

$$FC = \frac{v \cdot 10^{-3}}{\dot{V}_{fuel}} = 15.5 \frac{km}{l}$$

Now that the theoretical fuel consumption has been calculated, it is possible either to predict the range extinction for a given fuel tank capacity or to determine the fuel tank capacity for a given increase of autonomy.
For example, with all the previous assumptions and for a constant speed of 102.6 km/h, to guarantee an autonomy of 100 km more (that more or less is the maximum autonomy that a reservoir tank of a common petrol vehicle should provide) it is necessary to have a fuel tank that contains 6.45 litres of petrol.
From a theoretical point of view, it is possible to compare the autonomy extension of the present range extender (100 km with 6.45 litres of petrol at 102.6 km/h) with the one provided by the range extender mounted on the BMW i3, which has a fuel tank capacity of 9 litres (source: https://www.bmw.it/it/gamma/bmw-i/i3/2017/dati-tecnici.html#tab-1). The technical data of the BMW i3 report that the electric autonomy (NEDC) is comprises among 225 and 235 km, and it can be increased up to 330 km with the range extender. This means an extension of the range equal to about 100 km. Even if the fuel consumption of the present range extender has been computed for a constant speed of 102.6 km/h and not following the NEDC cycle, the fuel consumptions of the two devices have been compared. Moreover, the assumption used for calculating the fuel consumption of the RME range extender are conservative; for example, the drag coefficient of the BMW i3 is equal to 0.29 (instead of 0.32 that is a value for a common car), that is a more reasonable value for an electric vehicle. In Table 5 a comparison of the RME range extender with the BMW i3 range extender is reported.

Table 5 – Fuel consumptions comparison among RME range extender and BMW

Parameter	**RME range extender**	**BMW i3 range extender**
range extension	100 km (@ 102.6 km/h)	100 km (NEDC)
Fuel tank capacity	6.45 l	9 l
Fuel consumption	15.5 km/l	11.1 km/l

5.2 Forces on the slider crank mechanism

In this paragraph all the calculations of the forces involved in the present study of the slider crank mechanism are reported. The forces that act on the slider crank mechanism are due to both the pressure in the combustion chamber and the inertia of the components.

5.2.1 Force generated by the pressure in the combustion chamber

The principal input data for computing this force is the value of the pressure in the combustion chamber as a function of the crank angle. Its value has been analytically computed and its trend is reported in the graph in Figure 13.

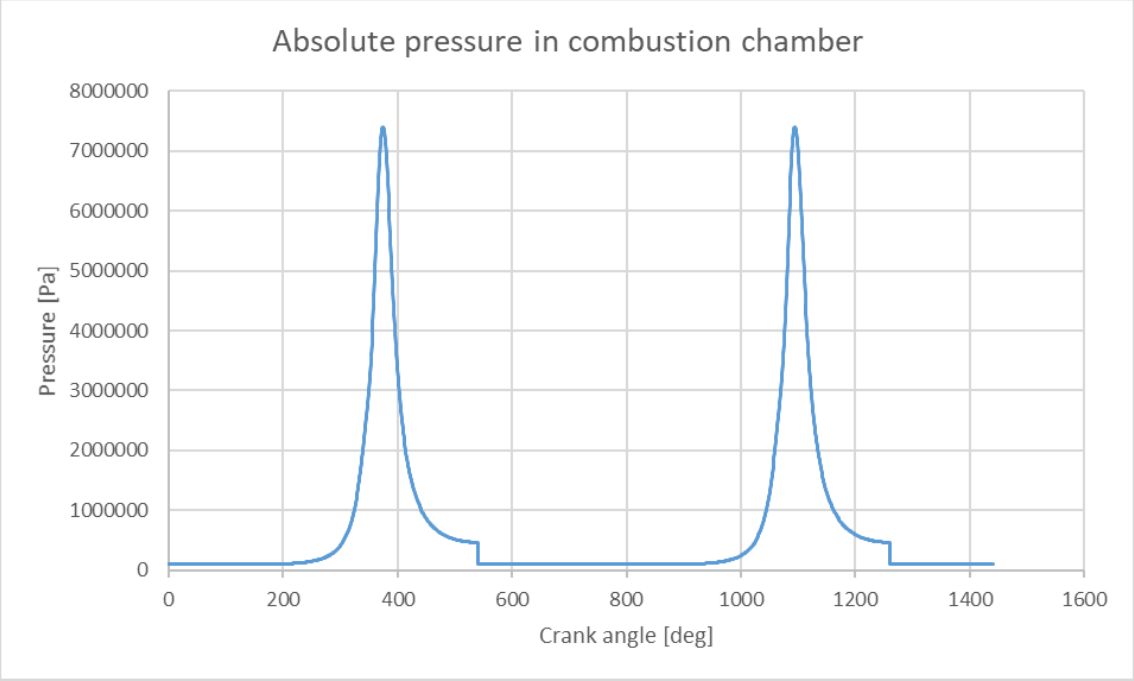

Figure 13 – Combustion chamber absolute pressure as a function of the crank angle; the graph represents the value in the combustion chamber of one of the two pistons referred to 4 complete revolutions

From the figure above, it is possible to see that there is a discontinuity of the pressure trend: such discontinuity is due to the opening of the discharge valves, that, for hypothesis of the used analytic formula, makes the internal pressure decreases instantly to the ambient value.
The value of the force generated by the pressure as a function of the crank angle is given by the following formula:

$$F_p(\alpha) = [p(\alpha) - p_0] \cdot \pi \frac{D_p^2}{4}$$

Where

- $p(\alpha)$ is the absolute pressure in the combustion chamber as a function of the crank angle
- p_0 is the basement pressure, that is equal to the ambient pressure (101300 Pa)
- D_p is the diameter of the piston

The value of this force is reported in Figure 14 and it is possible to notice that its trend is the same as the one of the pressure (Figure 13).

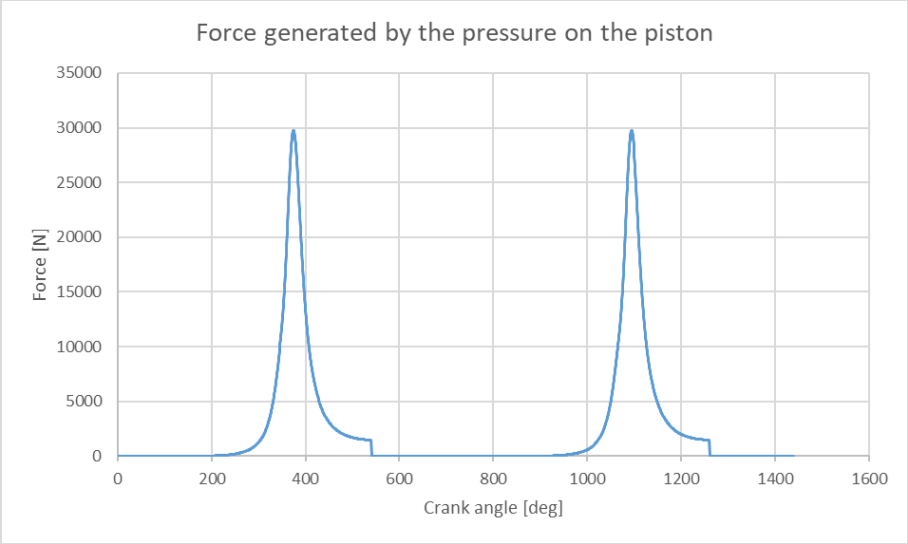

Figure 14 – Force generated by the pressure in the combustion chamber acting on the piston

The range of values is among a maximum value of 29815 N and a minimum value of 0 N.

5.2.2 Forces generated by the inertiae

The forces generated by the inertiae act on the piston, on the rod and on the crankshaft. While the piston and the crankshaft have only one kind of motion, alternative and rotational respectively, the rod has a rototraslative motion. Due to this, the mass of the rod is split into two contributions, one to the alternative motion and one to the rotational motion. In the following steps, the evaluation of these forces is shown, starting from the splitting of the mass of the rod.

- Inertia force due to the mass of the rod, with rototraslative motion

The rototraslative contribution, given by the mass of the rod, is split among the alternative and rotational contributions, by looking at the position of the centre of mass of the rod. The alternative mass is concentrated in the centre of the foot of the rod, while the rotational mass is concentrated in the centre of the head of the rod. This procedure is shown in Figure 15.

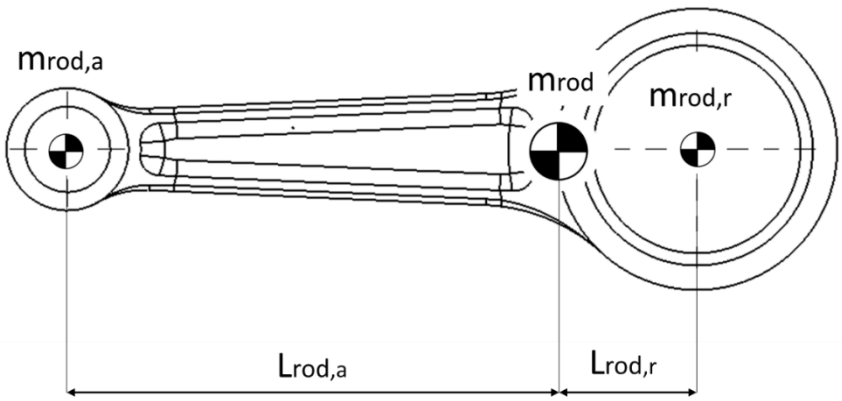

Figure 15 – Alternative mass and rotational mass of the rod

The two contributions of the mass are calculated by a static rotational equilibrium of the rod, as shown in the following steps.

The alternative contribution is calculated in this way:

$$m_{rod,a}\left(L_{rod,a} + L_{rod,r}\right) = m_{rod}L_{rod,r}$$

$$m_{rod,a} = m_{rod}\frac{L_{rod,r}}{\left(L_{rod,a} + L_{rod,r}\right)}$$

The rotational contribution is calculated in this way:

$$m_{rod,r}\left(L_{rod,a} + L_{rod,r}\right) = m_{rod}L_{rod,a}$$

$$m_{rod,r} = m_{rod}\frac{L_{rod,a}}{\left(L_{rod,a} + L_{rod,r}\right)}$$

The data and the results of this procedure are reported in the following table (Table 6).

Table 6 – Data and results of the calculation of masses contribution of the rod

DATA			
Parameter	**Variable name**	**Value**	**Unit**
Mass of the rod	m_{rod}	0.199	kg
Length of the rod	L	103	mm
Distance of the concentrated alternative mass from the centre of mass	$L_{rod,a}$	76.89	mm
Distance of the concentrated rotational mass from the centre of mass	$L_{rod,r}$	26.11	mm
RESULTS			
Parameter	Variable name	Value	Unit
Alternative contribution	$m_{rod,a}$	0.050	kg
Rotational contribution	$m_{rod,r}$	0.149	kg

- Inertia force due to the mass of the piston, with alternative motion

The inertia force on the piston (Figure 16 – Piston with the inertia force appliedFigure 16) takes into consideration the alternative contribution of the mass of the rod. The expression of the inertia as a function of the crank angle due to the alternative motion is given by the following equation:

$$F_{ip}(\alpha) = -(m_p + m_{rod,a})\omega^2 r(\cos\alpha + \lambda\cos 2\alpha)$$

In the following table (Table 7) all the data are reported.

Table 7 – Data used to determine the inertia of the piston

DATA			
Parameter	Variable name	Value	Unit
Mass of the piston	m_p	0.408	kg
Total alternative mass	$m_p + m_{rod,a}$	0.458	kg
Length of the rod	L	103	mm
Crank radius	r	30.7	mm
Angular speed	ω	419	rad/s

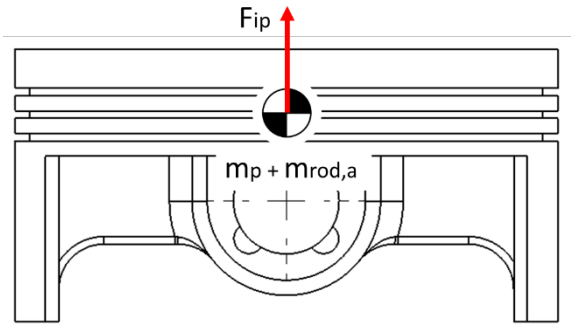

Figure 16 – Piston with the inertia force applied

- Inertia force due to the mass of the crank, with rotational motion

The inertia force due to the rotation is a centrifugal force and acts on the eccentric masses of the crankshaft, that are the crank and the equilibrium masses (Figure 17). So, first it is necessary to evaluate the mass of the crank and the equilibrium mass, as well as their distance from the rotational axis. Then the equilibrium masses are reduced to the centre of mass of the crank. The procedure to find the inertia force is shown in the following steps.
Equilibrium mass reduced to the crank thank to a static rotational equilibrium

$$m_{red} r = m_{eqm} r_w$$

$$m_{red} = m_{eqm} \frac{r_w}{r}$$

Centrifugal force applied to the centre of mass of the crank

$$F_c = (m_{crank} + m_{rod,r} - m_{red})\omega^2 r$$

The data needed to those calculations and the results are reported in the following table (Table 8).

Table 8 – Data and results of calculations of the rotational inertia forces

DATA			
Parameter	Variable name	Value	Unit
Mass of the crank	m_{crank}	0.263	kg
Equilibrium mass	m_{eqm}	0.827	kg
Radius of crank	r	30.7	mm
Radius of equilibrium mass	r_w	7.34	mm
Angular speed	ω	419	rad/s
RESULTS			
Parameter	Variable name	Value	Unit
Equilibrium mass reduced to the centre of mass of the crank	m_{red}	0.197	kg
Total rotational mass	$m_{crank}+m_{rod,r}-m_{red}$	0.215	kg
Centrifugal force	Fc	1185	N

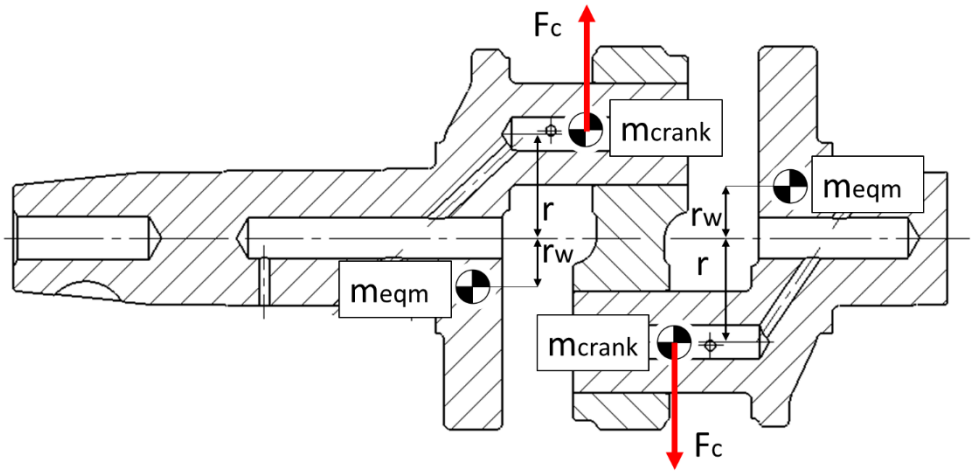

Figure 17 - Crankshaft with the inertia force (centrifugal force) applied

5.2.3 Forces and schematization of the slider crank mechanism

Once that all the forces have been calculated, a complete model of the mechanism can be implemented, for better understanding the situation. In particular, it is necessary to highlight the components of the forces acting on the piston, for determining the force transmitted by the rod to the crankshaft; even this latter force has a tangential component (that generates the motor torque) and a radial component. In Figure 18 the system is schematized and all the forces and their components are shown; the light blue arrows represent the forces calculated in the previous paragraphs, while the red arrows represent the force that will be calculated in this paragraph and that will be used for the assessments.

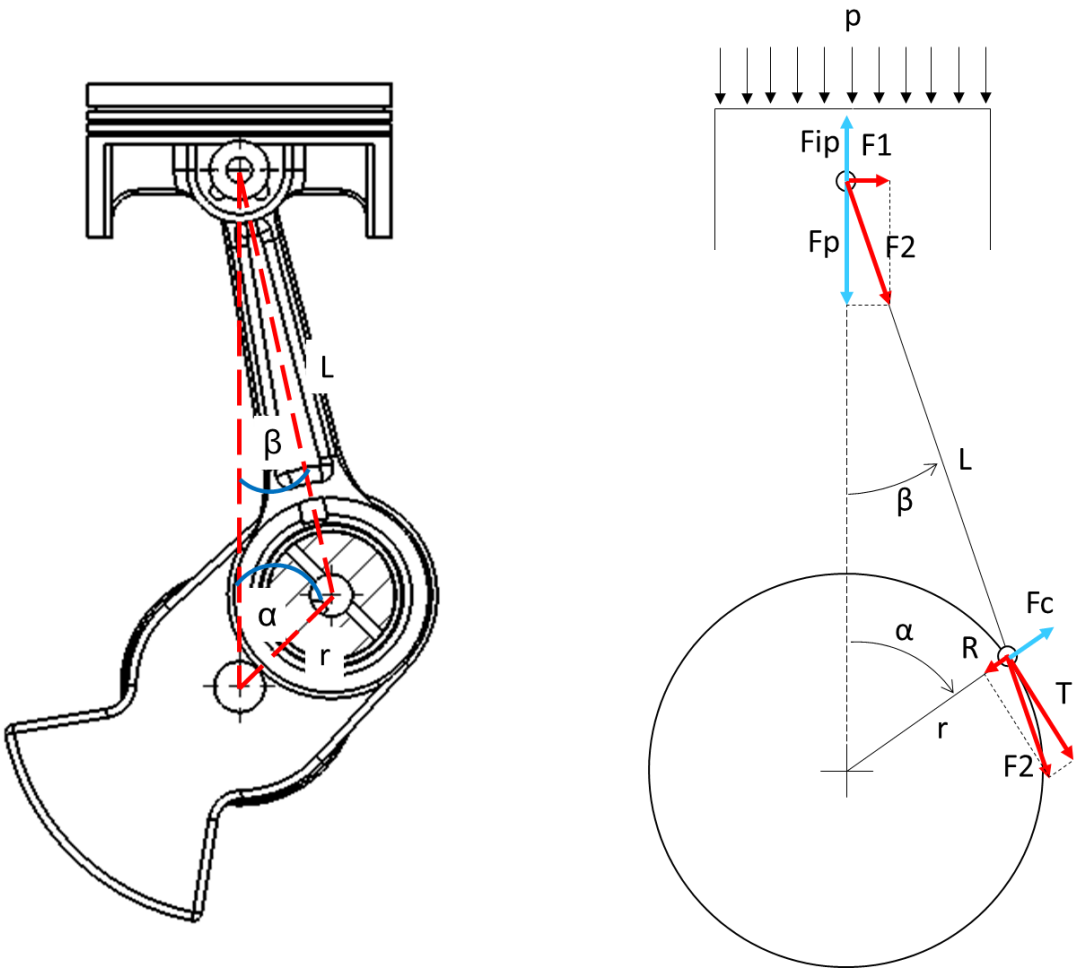

Figure 18 - Schematization of the slider crank mechanism with the forces applied

The meaning of the symbols of Figure 18 is reported in the following table (Table 9):

Table 9 – Meaning of the symbols

Symbol	Meaning
p	Pressure generated in the combustion chamber
Fp	Force generated by the pressure that acts on the piston
Fip	Inertia force that acts on the piston
F1	Force downloaded on the cylinder wall
F2	Force transmitted by the rod
T	Tangential component of F2 downloaded on the crank

R	Radial component of F2 downloaded on the crank
Fc	Centrifugal force of the crank
L	Length of the rod
r	Radius of the crank
α	Crank angle
β	Rod angle

For computing the components of the forces, it is necessary to apply simple trigonometric relations.
The calculations for determining the components on the piston are the following:

- The first parameter to find is the rod angle as a function of the crank angle

$$\beta = \arcsin\left(\frac{r}{L}\sin\alpha\right)$$

- The total force that acts on the piston, which contains both the pressure and the inertia contribution

$$\vec{F} = \overrightarrow{F_p} + \overrightarrow{F_{ip}}$$

- Force downloaded on the cylinder wall

$$F_1 = F\tan\beta$$

- Force transmitted by the rod

$$F_2 = \frac{F}{\cos\beta}$$

Once that the force transmitted by the rod has been determined, their components on the crank must be computed:

- Radial component of the force transmitted by the rod

$$R = F_2\cos(\alpha+\beta)$$

- Tangential component of the force transmitted by the rod

$$T = F_2\sin(\alpha+\beta)$$

A schematization of the crankshaft helps to better understand how the radial and tangential components act on it. The simplified model is reported in Figure 19.

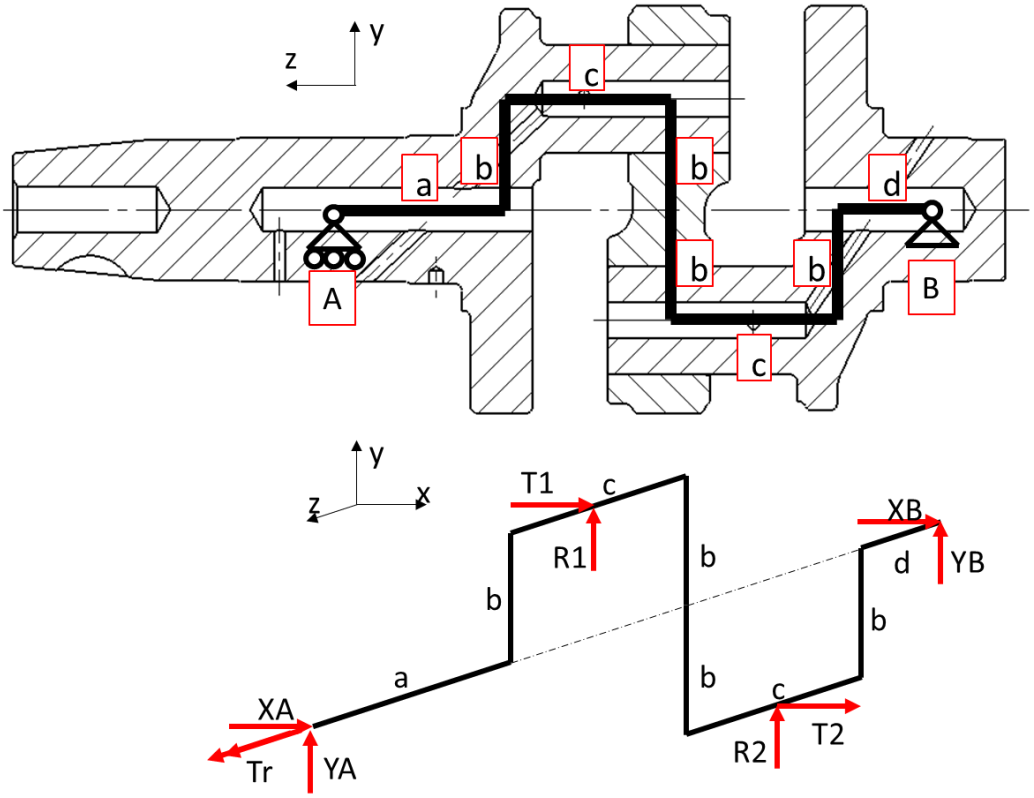

Figure 19 – Schematization of the crankshaft with the applied forces

5.3 Crankshaft design

The crankshaft design performed during this thesis work has received as input a starting model of this component, developed by the Robby Moto Engineering S.R.L. thanks to their experience in the engine field. However, there were some design steps that had to be done, such as the definition of the interference fit among the cranks and the central part of the crankshaft, the conical coupling between the alternator and the crankshaft output, the typical static and fatigue assessment and the modal analysis.

5.3.1 Interference fit

The interference fit is a type of coupling that is done by means of interference between a component that acts as a shaft and another that acts as a hub. In particular, the components that have to be joined in this way are the two cranks and the central part of the crankshaft, as shown in Figure 20 and in Figure 21.

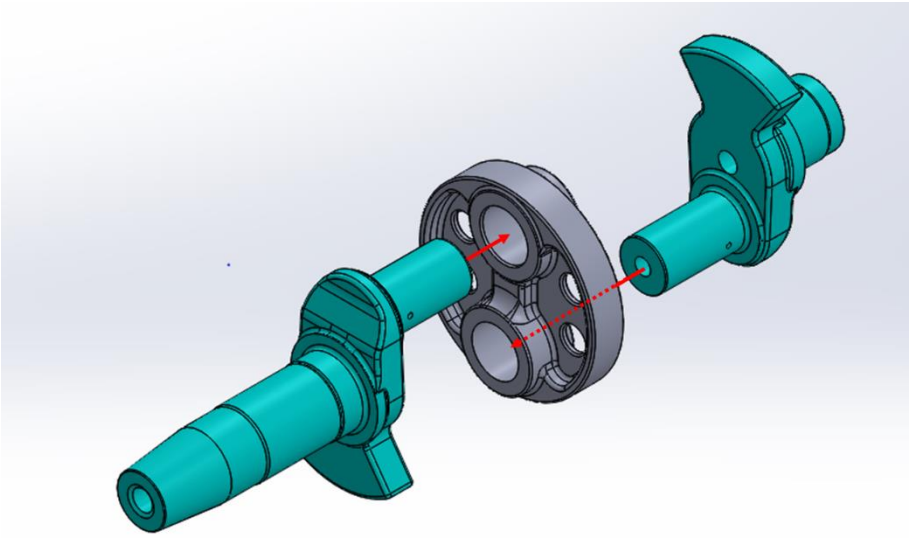

Figure 20 – Coupling by interference fit of the main components of the crankshaft

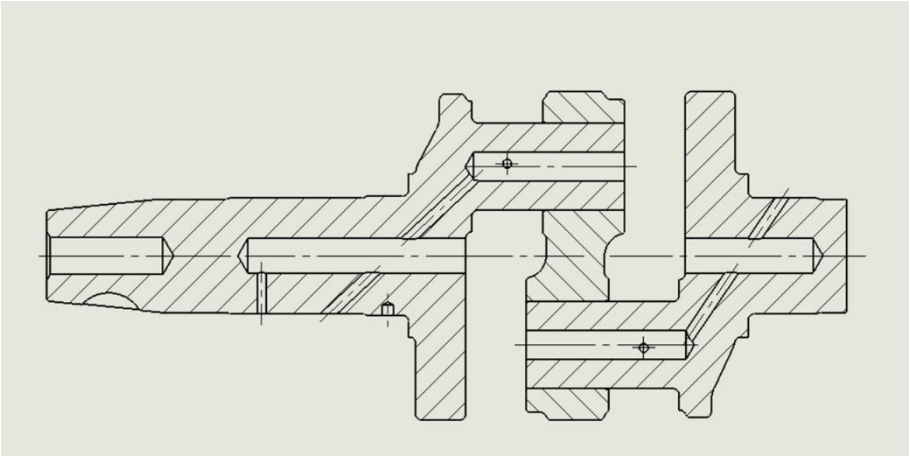

Figure 21 – Longitudinal section view of the assembled crankshaft

For designing the interference fit coupling, it is first necessary to evaluate the maximum torque that it undergoes, and then to determine the minimum interference that ensure a contact pressure able to guarantee the transmission of such torque. These steps have

been performed in an analytical way, as it will be shown in the next chapters. Once the minimum necessary interference has been found, we proceed with the determination of the dimensional tolerances, defining the interference range of the coupling. Then, after the designing procedure, two assessments (both static) have been performed:

- Static strength assessment, performed analytically and by FEM analysis using the maximum elastic interference to evaluate the generated stress in the components
- Contact pressure assessment, performed with a FEM analysis using the minimum interference to evaluate whether the real minimum contact pressure guarantees the torque transmission

5.3.1.1 Analytic design

The analytic design of the interference fit consists of determining the dimensional tolerances of the component that acts as a shaft and the one that acts as an hub, that guarantee the proper range of interference; a proper range of interference is characterized by a minimum value that allows the torque transmission without slippage and a maximum value that does not break the coupling.
The first quantity to calculate is the torque that pass through the coupling. For computing this quantity, it is necessary to evaluate the internal action of the crankshaft in terms of torsion. Since the forces are a function of the crank angle, the internal actions have been calculated as a function of the crank angle as well. The most critical case has been determined for a crank angle equal to 25°. The crankshaft beam model is reported in Figure 22, with the loads that contribute to the torque. The configuration of the loads shown in this figure is for a crank angle equal to 25°, value for which the most critical value has been found. Moreover, the sign of the forces and reaction forces reported in the following calculations is coherent with the model.

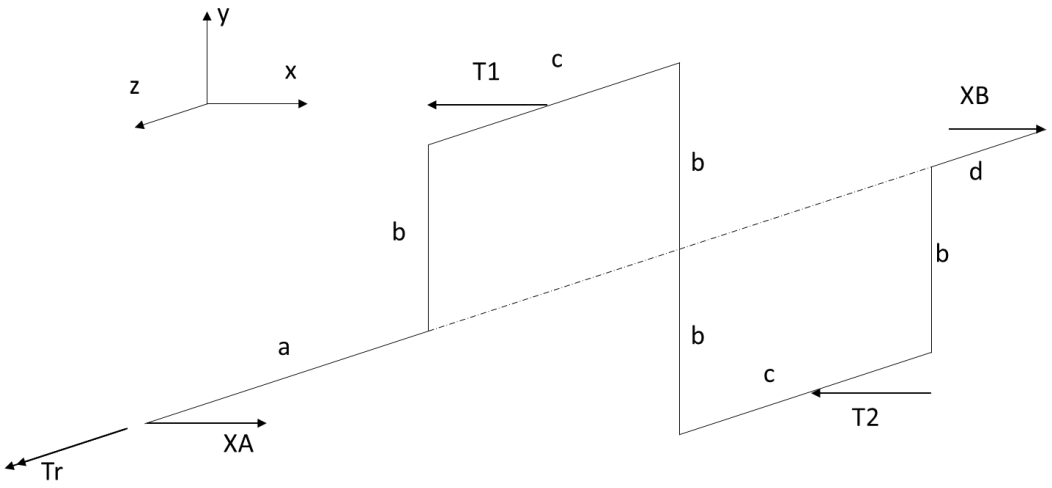

Figure 22 – Model of the crankshaft for determining the internal action of torsion

The dimensions of the crankshaft model of the above figure (Figure 22) are reported in the following table (Table 10Table 10 – Dimensions of the crankshaft's model)

Table 10 – Dimensions of the crankshaft's model

Variable name	Value	Unit
a	49	mm
b	30.7	mm
c	46	mm
d	24.5	mm

From this point on, all the reported values in this paragraph are related to the crank angle α=25°.
Then, for evaluating the internal actions, the reaction forces XA and XB must be calculated, given the values of the two forces T1 and T2.

$$T1(\alpha = 25°) = 1540\ N \qquad T2(\alpha = 25°) = 11497\ N$$

The reaction force XA is calculated by a rotational equilibrium in the plane x-z respect to B

$$\sum M_B = XA \cdot (a + 2c + d) - T1 \cdot \left(\frac{3}{2}c + d\right) - T2 \cdot \left(\frac{1}{2}c + d\right) = 0$$
$$XA = \frac{T1 \cdot \left(\frac{3}{2}c + d\right) + T2 \cdot \left(\frac{1}{2}c + d\right)}{(a + 2c + d)} = 4148\ N$$

While the reaction force XB is calculated by a force equilibrium in the direction of the x axis

$$\sum F_x = XA - T1 - T2 + XB = 0$$
$$XB = T1 + T2 - XA = 8845\ N$$

The resistance torque Tr is computed by a rotational equilibrium around the longitudinal axis of the crankshaft, that is in z direction

$$\sum Tz = T_r + T1 \cdot b - T2 \cdot b = 0$$
$$Tr = (T2 - T1) \cdot b = 306417\ Nmm$$

Finally, it is possible to determine and draw the internal action diagram of the torsion (Figure 23).

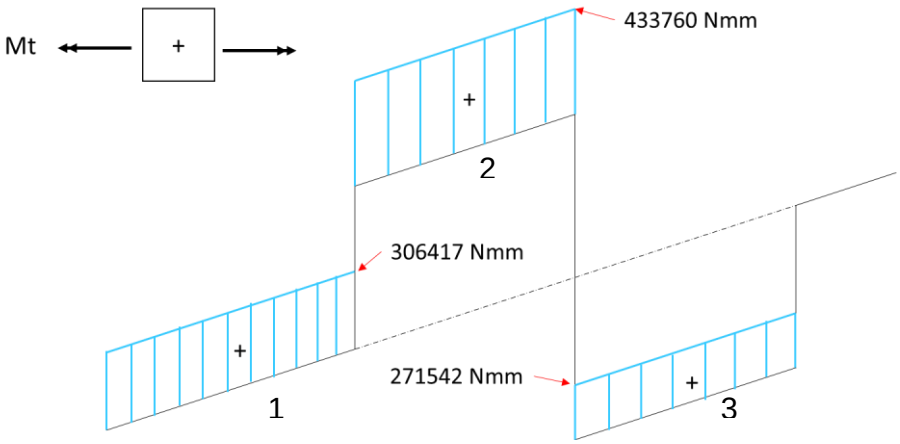

Figure 23 - Torsion diagram of the beam model of the crankshaft for the most critical case (α=25°)

As shown in the above diagram (Figure 23) the higher torsion is in the upper branch (branch 2) and so the interference fit will be designed by looking at that part of the crankshaft; such part represent the coupling between the posterior crank and the central part of the crankshaft (Figure 24).

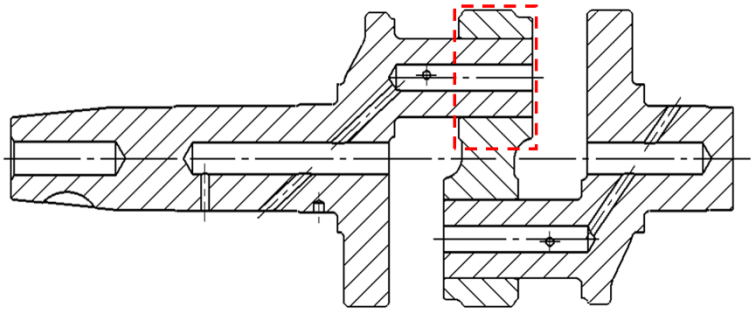

Figure 24 – Representation of the most stressed coupling, that is the one between the posterior crank and the central part of the crankshaft

Once the maximum torque to be transmitted has been found, the next step is to determine the interference needed. Such interference must guarantee a contact pressure that can generates the tangential stress for the torque transmission. Of course, the relation among the pressure and the tangential stress depends on the friction coefficient, that in this case is the static friction coefficient steel to steel f=0.2. Such relation is given by the following expression.

$$\tau = f \cdot p$$

Now the tangential stress (τ) must be expressed as a function of the maximum torque, in order to find its value.

$$T_{max} = \int_A \tau \cdot r \cdot dA = \int_0^{2\pi} \tau \cdot r \cdot r \cdot L \cdot d\alpha = \tau \cdot r^2 \cdot L \cdot 2\pi$$

$$\tau = \frac{T_{max}}{2\pi r^2 L} = 11.8\ MPa$$

By substituting the expression of the tangential stress in the relation that links it to the pressure by means of the friction coefficient, and making the pressure explicit, the following formula is obtained.

$$p = \frac{\tau}{f} = \frac{T_{max}}{2\pi r^2 L f} = 59\ MPa$$

The obtained value represents the minimum pressure that the interference must provide in order to ensure the necessary tangential stress for the torque transmission, given the friction coefficient steel to steel.
Finally, the value of the interference needed can be calculated by its definition, that is the difference between the bigger diameter (the one of the shaft) and the lower diameter (that is the one of the hub).

$$i = d_s - d_h$$

Since both the diameter of the shaft and of the hub are unknown, the above formula must be developed more into the detail, obtaining the interference as a function of the pressure. So, first of all, it has to be expressed as a function of the circumferential strains.

$$i = \Delta d_h - \Delta d_s = \varepsilon_{\theta,h} \cdot d_{nom} - \varepsilon_{\theta,s} \cdot d_{nom} = d_{nom} \cdot (\varepsilon_{\theta,h} - \varepsilon_{\theta,s})$$

Then, the constitutive laws of the circumferential strain of both the shaft and the hub will be substituted in the above formula. Since the shaft and the hub are made of the same material, the Young modulus and the Poisson's ratio are the same, and so they will be group. The constitutive laws are the followings two.

$$hub: \varepsilon_{\theta,h} = \frac{1}{E_h}\left(\sigma_{\theta,h} - \nu_h \sigma_{r,h}\right) \qquad shaft: \varepsilon_{\theta,s} = \frac{1}{E_s}\left(\sigma_{\theta,s} - \nu_s \sigma_{r,s}\right)$$

And the circumferential and radial stresses, in the case of the hollow disk, are in their turn substituted in the constitutive laws equations. The circumferential and the radial stresses are reported here below.

$$hub: \begin{cases} \sigma_{r.h} = -p \\ \sigma_{\theta,h} = p\dfrac{a_h^2 + 1}{a_h^2 - 1} \end{cases} \qquad shaft: \begin{cases} \sigma_{r,s} = -p \\ \sigma_{\theta,s} = -p\dfrac{a_s^2 + 1}{a_s^2 - 1} \end{cases}$$

Where the terms a_h and a_s represent the ratio among the external and internal diameters (or the rays) of the two components, as shown in Figure 25.

$$a_h = \frac{d_{h,e}}{d_{h,i}} = 1.6 \qquad a_h = \frac{d_{s,e}}{d_{s,i}} = 3$$

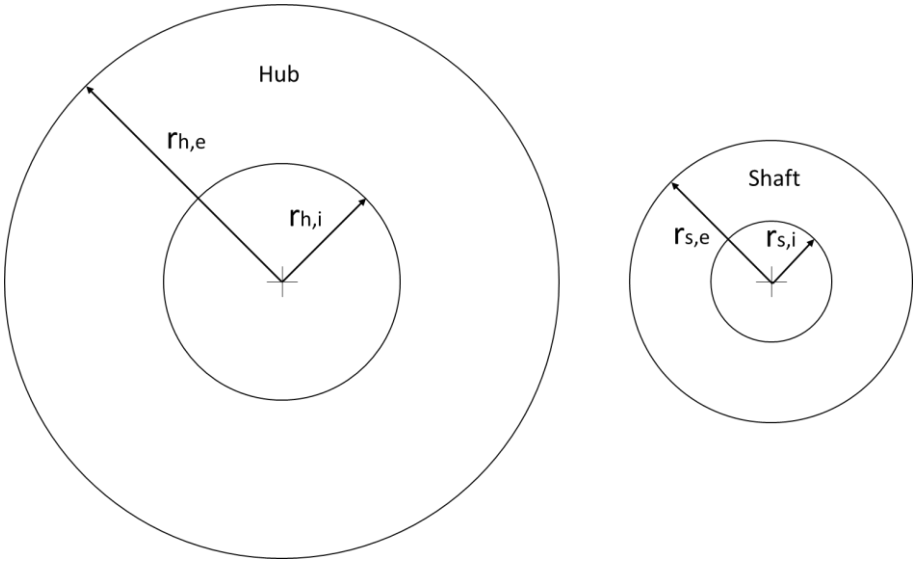

Figure 25 – External and internal radius of the hub and of the shaft

The final expression of the interference as a function of the pressure is then obtained. Moreover, a service faction k_s=2 has been used, for doubling the pressure to be ensured, in order to obtain a more conservative result (conservative for a slippage point of view).

$$i_{min,el} = \frac{k_s \cdot p \cdot d_{nom}}{E} \cdot \left[\frac{a_h^2 + 1}{a_h^2 - 1} + \frac{a_s^2 + 1}{a_s^2 - 1}\right] = 60.6\ \mu m$$

Once that the minimum elastic interference has been determined, the dimensional tolerances must be selected. The needed information is about the tolerance class of the two components, that in this case is IT7 for the hub and IT6 for the shaft, and about the surface roughness of the contact surfaces, that are Ra=2 μm for the hub and Ra=1.6 μm for the shaft. Given this two information, the dimensional tolerances should be selected for ensuring an interference that is equal or higher to the minimum elastic one. In this case the choice has fallen on an h for the shaft and a V for the hub. Se the final dimensions are:

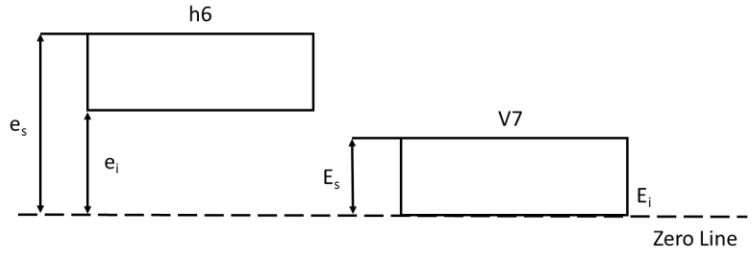

$$\text{SHAFT } 30\text{h}7^{+0.016}_{+0.000} \qquad \text{HUB } 30\text{V}7^{-0.068}_{-0.093}$$

Where the nominal diameter is $d_{nom} = 30\ mm$.
Now the real minimum and maximum interferences can be evaluated.

$$i_{min,ISO} = \left(d_{s,min} - d_{h,max}\right) + 2Ra_s + 2Ra_h = 75.2\ \mu m$$

$$i_{max,ISO} = \left(d_{s,max} - d_{h,min}\right) + 2Ra_s + 2Ra_h = 116.2\ \mu m$$

Once that the tolerances have been found, he next step is to perform the assessments.

5.3.1.2 Analytic static strength assessment

The analytic static strength assessment is performed to ensure that the coupling will not break as soon as the shaft is forced into the hub. This assessment is done by extracting the pressure as a function of the maximum elastic interference (that is the maximum interference without considering the roughness), and then calculating the hoop and radial stresses using the hollow disk with internal and external pressure formulation. It is important to underline that such method assumes a constant pressure all over the contact while in the reality it is variable in function of the position (this is why the FEM assessment has to be performed).
The maximum elastic interference is calculated in this way:

$$i_{max,el} = i_{max,ISO} - (2Ra_s + 2Ra_h) = 109\ \mu m$$

This value is then put into the equation of the interference, making the pressure explicit.

$$i_{max,el} = \frac{p_{max} \cdot d_{nom}}{E} \cdot \left[\frac{a_h^2 + 1}{a_h^2 - 1} + \frac{a_s^2 + 1}{a_s^2 - 1}\right] \rightarrow$$

$$\rightarrow p_{max} = \frac{i_{max,el} \cdot E}{d_{nom}} \cdot \left[\frac{a_h^2 + 1}{a_h^2 - 1} + \frac{a_s^2 + 1}{a_s^2 - 1}\right]^{-1} = 213\ MPa$$

The maximum contact pressure is then used for the hollow disk formula, simulating a situation reported in Figure 26: for the hub the pressure is internal while for the shaft the pressure is external.

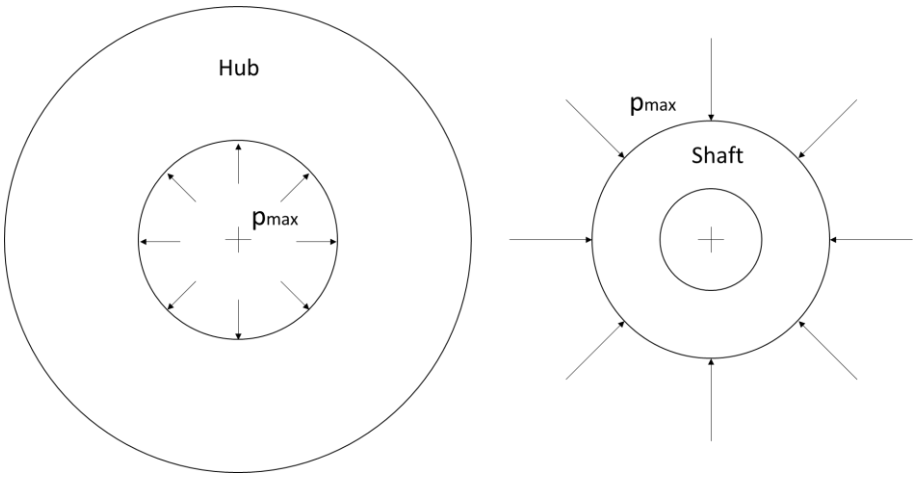

Figure 26 – Hub and shaft with the maximum contact pressure applied

Then, after the computation of the contact pressure, the radial and the circumferential stresses in the most stressed points must be evaluated.
The used criteria for the static assessment is the Guest-Tresca one, and so it is necessary to evaluate the principal stresses for both the components in the most critical zones. The principal stress to be evaluated for the hollow disk are the radial and the circumferential,

while the axial is always considered null. The expressions of those stresses, in the contact surface zone, are the same used for the interference fit design.

$$hub: \begin{cases} \sigma_{r.h} = -p = -213\ MPa \\ \sigma_{\theta,h} = p\dfrac{a_h^2+1}{a_h^2-1} = 486\ MPa \\ \sigma_{ax,h} = 0\ MPa \end{cases} \qquad shaft: \begin{cases} \sigma_{r,s} = -p = -213\ MPa \\ \sigma_{\theta,s} = -p\dfrac{a_s^2+1}{a_s^2-1} = -266\ MPa \\ \sigma_{ax,s} = 0\ MPa \end{cases}$$

Once that the principal stress in the contact zone have been found, the Guest-Tresca stresses must be evaluated and then compared to the yielding strength of the material.

$$hub: \sigma_{GT,h} = \sigma_{\theta,h} - \sigma_{r.h} = 699\ MPa \qquad shaft: \sigma_{GT,s} = \sigma_{ax,s} - \sigma_{\theta,s} = 266\ MPa$$

For both the components the Guest-Tresca stress is below the yielding strength (σ_y=735 MPa) and the safety factor are the following.

$$hub: \eta = \frac{\sigma_y}{\sigma_{GT,h}} = 1.05 \qquad shaft: \eta = \frac{\sigma_y}{\sigma_{GT,s}} = 2.76$$

The safety factor of the hub is very close to the unitary value but, since this is a static assessment and the load is not cyclical, the interference fit is from a static point of view safe.
The shaft has been assessed also in his inner surface, that has proven to be more stressed that the contact surface.

$$shaft: \begin{cases} \sigma_{r,s} = 0\ MPa \\ \sigma_{\theta,s} = -2p\dfrac{a_s^2}{a_s^2-1} = -479\ MPa \\ \sigma_{ax,s} = 0\ MPa \end{cases}$$

The Guest-Tresca value in the inner radius of the shaft is the following.

$$shaft: \sigma_{GT,s} = \sigma_{ax,s} - \sigma_{\theta,s} = 479\ MPa$$

Obtaining a safety factor bigger than the unit.

$$shaft: \eta = \frac{\sigma_y}{\sigma_{GT,s}} = 1.53$$

A recap of the analytic results is reported in the following table (Table 11).

Table 11 – Results of the analytic calculations on the hub and on the shaft

Hub contact surface			
Hoop stress	Radial stress	Axial stress	Guest-Tresca stress
486 MPa	-213 MPa	0 MPa	699 MPa
Shaft contact surface			
Hoop stress	Radial stress	Axial stress	Guest-Tresca stress
-266 MPa	-213 MPa	0 MPa	266 MPa
Shaft contact surface			
Hoop stress	Radial stress	Axial stress	Guest-Tresca stress
-479 MPa	0 MPa	0 MPa	479 MPa

Concluding, the interference fit between the posterior crank and the central part of the shaft is statically safe from an analytical point of view. However, a more detailed analysis made by means of a FEM software (Abaqus) has been necessary.

5.3.1.3 FEM static strength assessment

The FEM static strength assessment has been performed by using the maximum elastic interference. The purpose of this assessment is to verify the real trend of the pressure along the contact surface. Indeed, the analytical assessment considers the pressure as uniformly distributed along the coupling.
The two components to be modelled are the posterior crank (that acts as the shaft) and the central part of the crankshaft (that acts as the hub). They have been modelled by using CAX4R (A 4-node bilinear axisymmetric quadrilateral, reduced integration, hourglass control), in order to get the consistent results quicker than using a three-dimensional model. In Figure 27 it is shown how the two components have been modelled from a geometrical point of view. Since the used elements are axisymmetric, it has been sufficient to define their section. Moreover, their final assembly is reported in Figure 28.

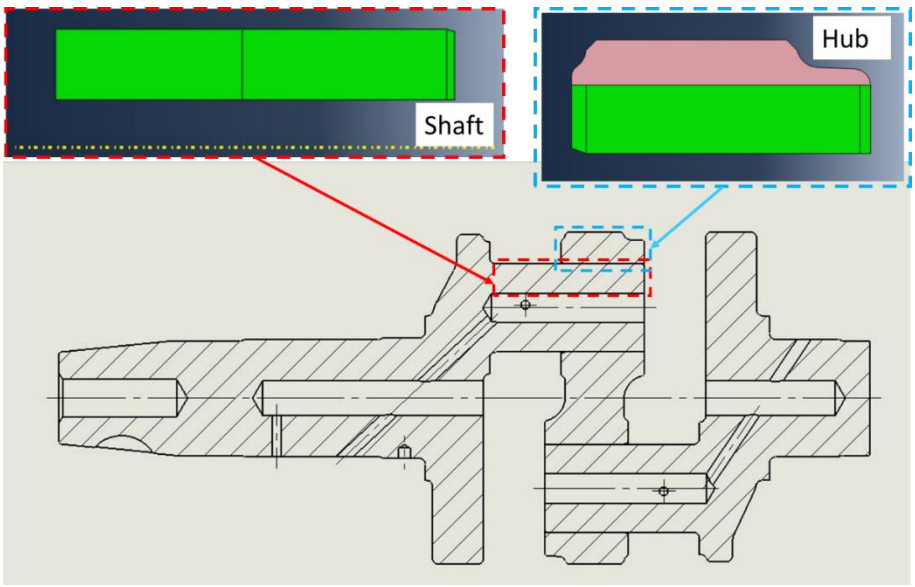

Figure 27 - Longitudinal section of the crankshaft, geometry of the shaft (up-left) and geometry of the hub (up-right)

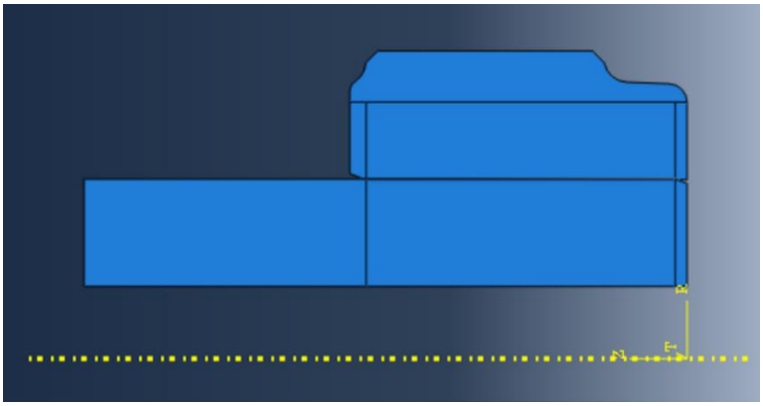

Figure 28 – Assembly of the shaft and the hub

The maximum elastic interference is totally provided by increasing the external radius of the shaft, while the inner radius of the hub is the nominal one. The used values for the coupling are reported below; all the other dimensions have been taken from the drawing.

$$i_{max,el} = i_{max,ISO} - (2Ra_s + 2Ra_h) = 109\ \mu m$$

$$hub: r_{h,i} = \frac{d_n}{2} = 15\ mm \qquad shaft: r_{s,e} = \frac{d_n}{2} + \frac{i_{max,el}}{2} = 15.0545\ mm$$

The sketches of the axisymmetric section of the shaft and of the hub, with the dimensions reported, are reported in the following figure (Figure 29).

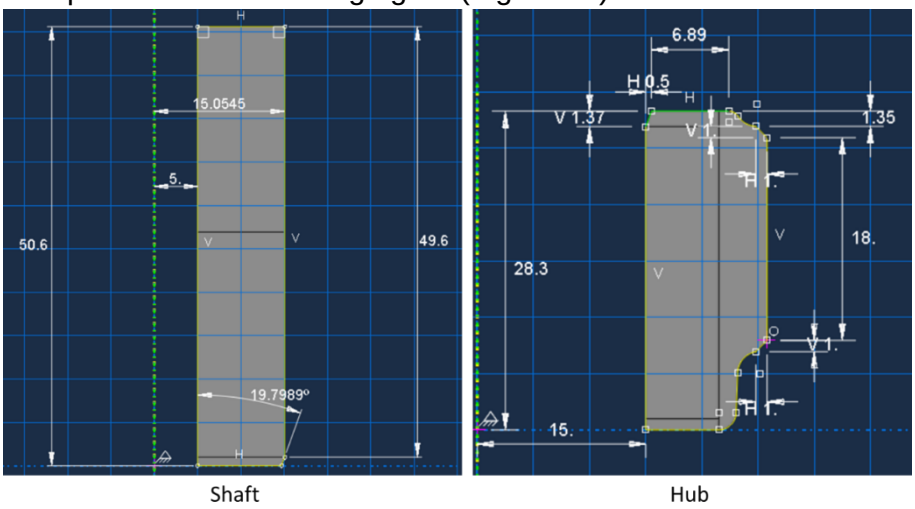

Figure 29 – Sketches of the axisymmetric section of the shaft and of the hub used in the FEM static strength assessment

The interaction between the two surfaces has been defined as a surface to surface contact (in the Abaqus interaction module), specifying that is and interference fit and that friction is present.
Since the most stressed component is the hub, its surface has been set as the slave, while the shaft surface has been set as the master. The interaction and its property are reported in a summary image in which all the steps are reported (Figure 30).

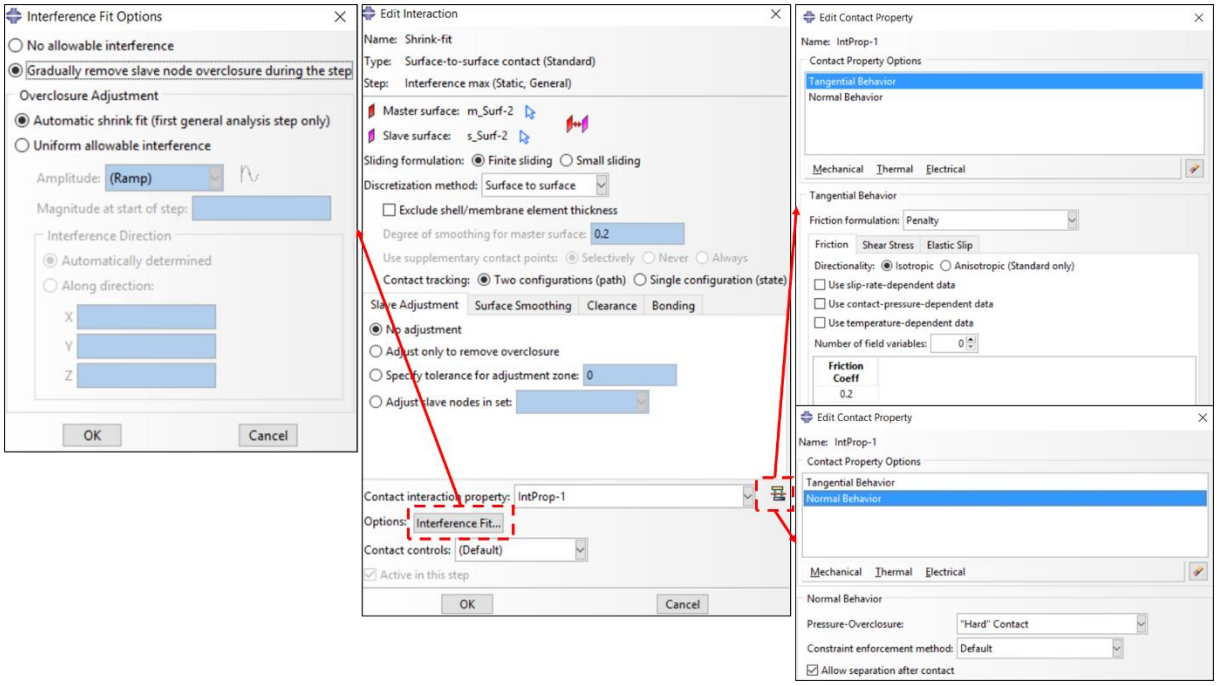

Figure 30 – Abaqus definition of the interaction between the two surfaces

In Figure 31 the final model with the interaction is shown, highlighting the master surface in red and the slave surface in purple.

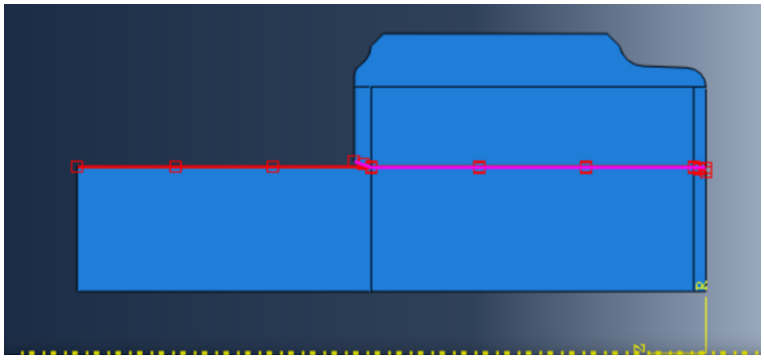

Figure 31 – Surfaces involved in the interaction properties; the red surface, that belongs to the shaft, is the master, while the purple surface, that belongs to the hub, is the slave

The mesh is finer for the hub, since it is the slave, while it is coarser for the shaft, since it is the master. In particular, the selected size of the grid selected for the hub is 0.5, while for the shaft is 0.8. In Figure 32 the meshed model of the two components involved in the interference fit coupling is shown.

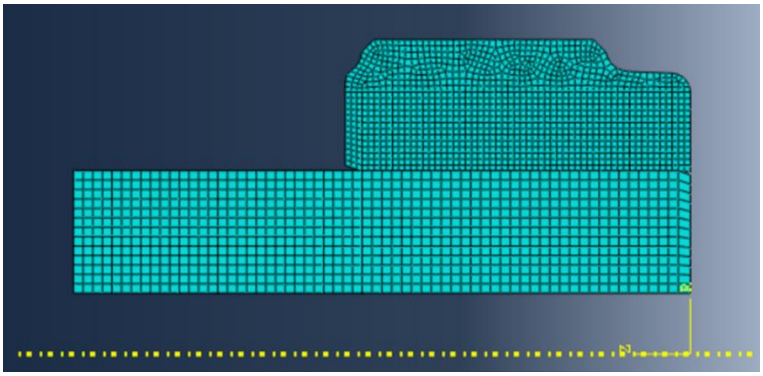

Figure 32 – Meshed model of the two components involved in the coupling

The FE model, which better approximates the reality than the analytical model, shows the presence of other stress components in addition to the hoop and radial, such as the axial and the in plane shear. But this is not a problem, since for the static assessment it is sufficient the Mises equivalent stress, that is provided by the software itself.
In Figure 33, the results of the first FEM analysis of the coupling are shown, in particular the Mises stress.

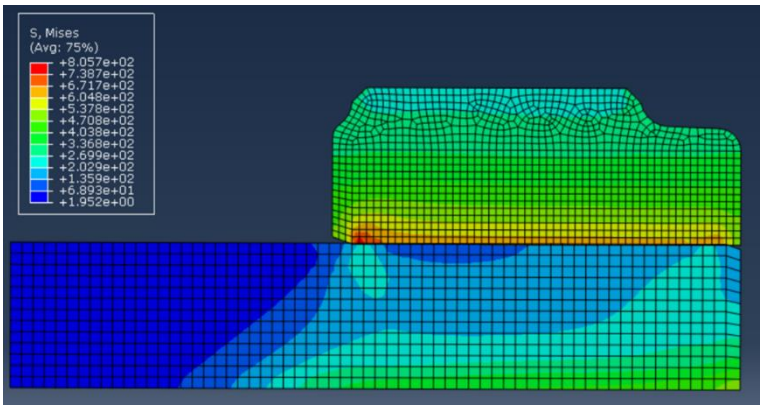

Figure 33 – Results of the first FEM analysis in terms of Von Mises stress

A deeper analysis of the principal stresses of both the hub and the shaft has been done, also for a comparison with the stresses analytically found.

Hub

Concerning the hub, the trend of the stresses has been extrapolated from the path shown in Figure 34.

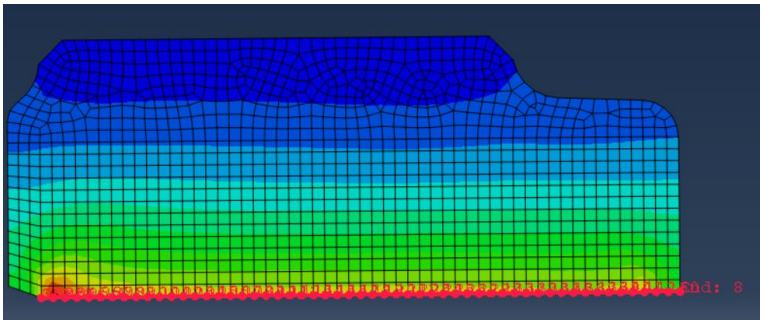

Figure 34 – Path on the contact surface of the hub used for the stresses extrapolation

In the following graphs, the trends of the hoop and of the radial stresses and of the equivalent Mises stress extracted from the above path are shown and commented:

1. Hoop and radial stresses

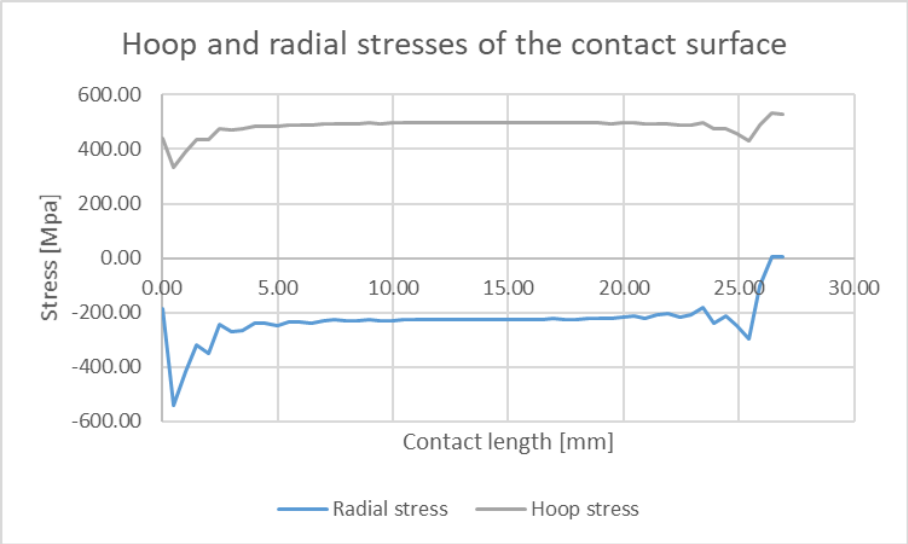

Figure 35 - Trend of the hoop and radial stresses of the contact surface of the hub

2. Mises equivalent stress

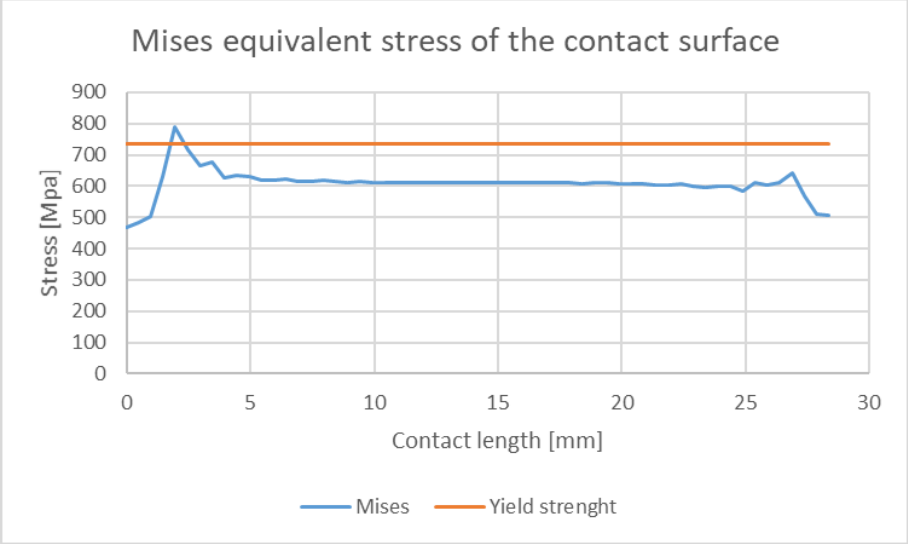

Figure 36 – Trend of the Mises equivalent stress of the contact surface of the hub

From the above graph it is noticeable that the Mises equivalent stress exceed the yielding limit, making necessary a plastic FEM analysis, for evaluating the yielded zone magnitude.

Shaft

Concerning the shaft, the trend of the stresses has been extrapolated from the two paths shown in Figure 37:

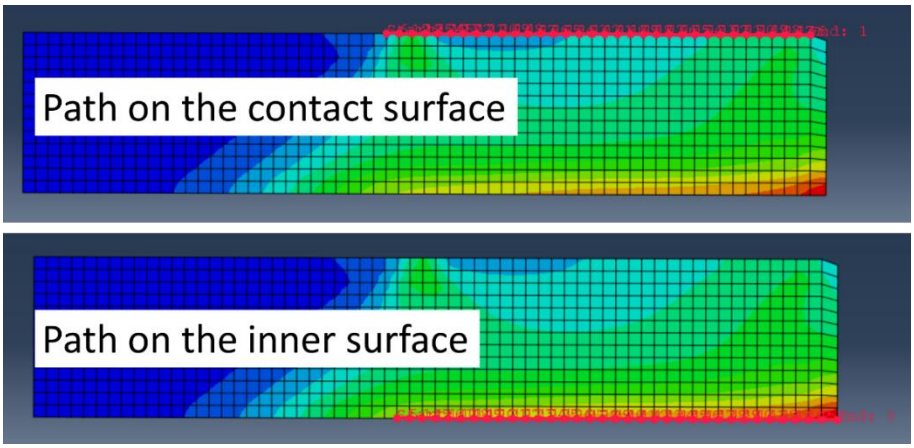

Figure 37 - Paths used for the stress extrapolation: the one above is the path on the contact surface while the one below in the path on the inner surface of the shaft

The stresses have been evaluated also in the inner surface of the shaft because this latter one is more stressed than the contact surface. In the following graphs, the trends of the hoop and of the radial stresses and of the equivalent Mises stress extracted from the above paths are shown and commented:

3. Hoop and radial stresses on the contact surface

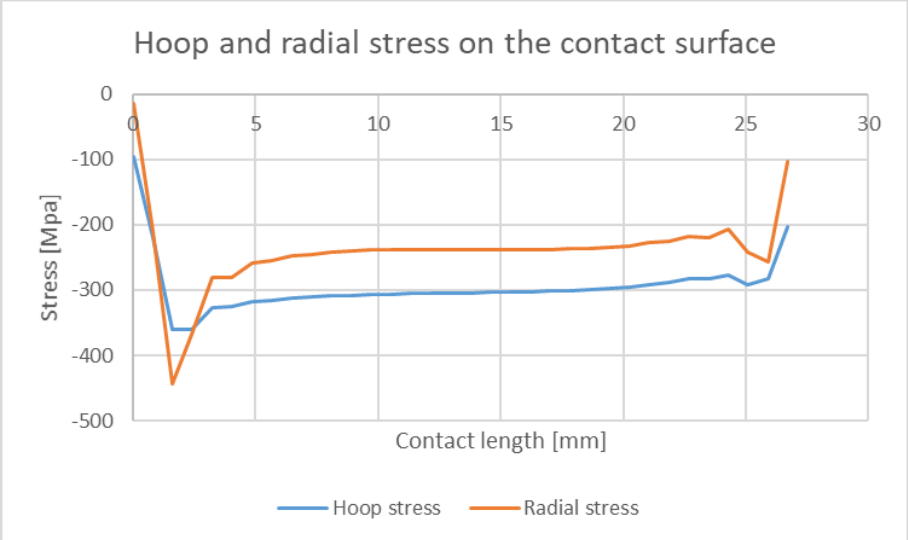

Figure 38 - Trend of the hoop and radial stresses of the contact surface of the shaft

4. Mises equivalent stress of the contact surface

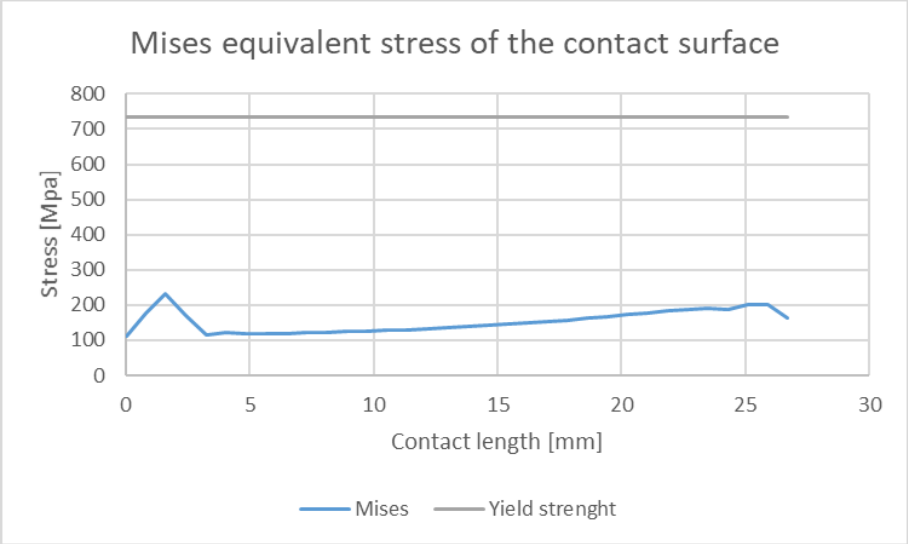

Figure 39 - Trend of the Mises equivalent stress of the contact surface of the shaft

From the above graph it is possible to see that the Mises equivalent stress is below the yield strength all over the contact length, thus the component is statically safe.

5. Hoop and radial stresses on the inner surface

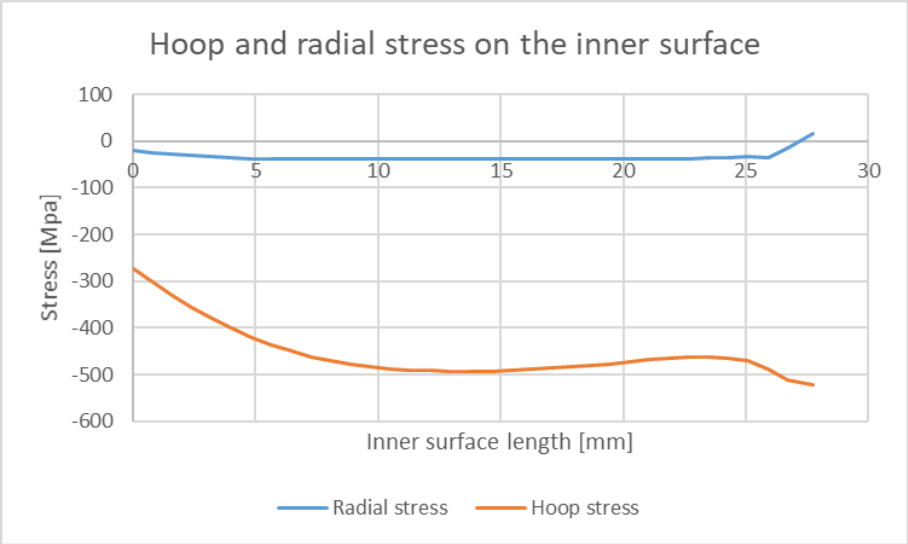

Figure 40 – Trend of the hoop and radial stresses on the inner surface of the shaft

6. Mises equivalent stress on the inner surface

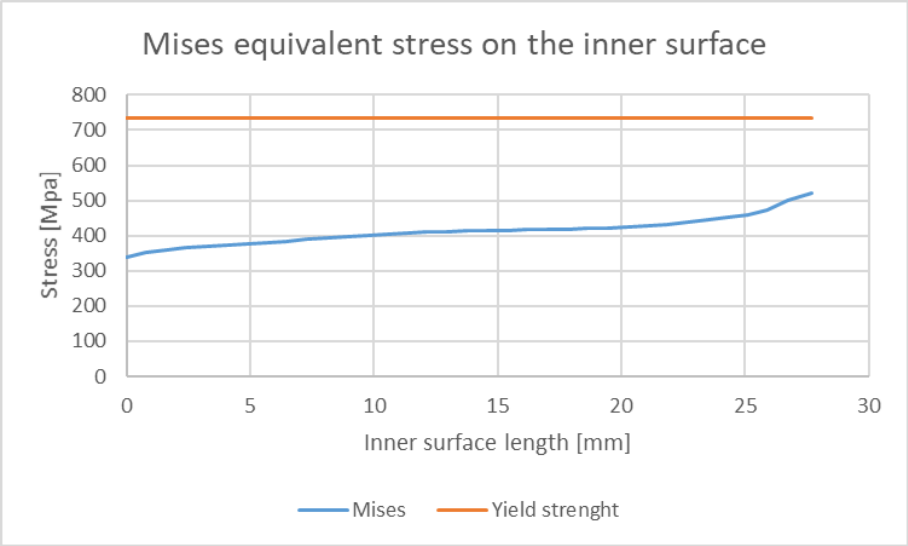

Figure 41 - Trend of the Mises equivalent stress on the inner surface of the shaft

From the above graph it is possible to see that the Mises equivalent stress is below the yield strength all over the contact length, thus the component is statically safe.

Since the hub contact surface shows a Mises equivalent stress that is locally higher than the yield strength, a second FEM analysis for deeper investigating this part has been performed. In particular, the modification did to the first analysis are: the mesh in the investigated zone of the hub has been refined, the element type used is CAX8R (An 8-node biquadratic axisymmetric quadrilateral, reduced integration), and the plastic properties of the material have been set. In this way an elasto-plastic evaluation has been done, and the extension of the yielding zone is reported in Figure 42, in terms of equivalent plastic strain (PEEQ).

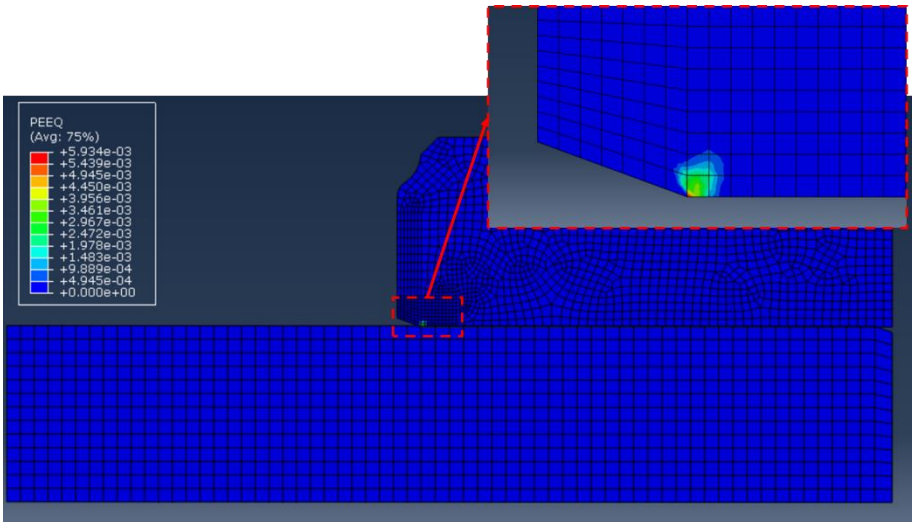

Figure 42 - Results of the second FEM analysis in terms of equivalent plastic strain PEEQ

The maximum equivalent plastic strain value is of 0.59 % and the plasticized zone is width about 0.5 mm and high about 0.5 mm, thus is very small both in terms of value and extension. Moreover, since the interference fit generates a constant stress over the time,

the yielding is static and not cyclic. In addition to this, it is to be remembered that this is a limit condition, statistically unlikely.
In the following table (Table 12) a recap of the first FEM static strength assessment results is reported.

Table 12 – Results of the first FEM analysis

First FEM analysis: elements type CAX4R					
Hub contact surface					
Max abs hoop stress	Avg hoop stress	Max abs radial stress	Avg radial stress	Max abs Mises stress	Avg Mises stress
531 MPa	484 MPa	-539 MPa	-230 MPa	790 MPa	608 MPa
Shaft contact surface					
Max abs hoop stress	Avg hoop stress	Max abs radial stress	Avg radial stress	Max abs Mises stress	Avg Mises stress
-360 MPa	-294 MPa	-443 MPa	-238 MPa	231 MPa	152 MPa
Shaft inner surface					
Max abs hoop stress	Avg hoop stress	Max abs radial stress	Avg radial stress	Max abs Mises stress	Avg Mises stress
-522 MPa	-454 MPa	-39 MPa	-34 MPa	520 MPa	412 MPa

In the following table (Table 13) a recap of the second FEM static strength assessment results is reported.

Table 13 – Results of the second FEM analysis

Second FEM analysis: elements type CAX8R		
Hub contact surface		
Max equivalent plastic strain	Yielded zone width	Yielded zone height
0.59%	0.5 mm	0.5 mm

Concluding, at the end of the FEM static strength analysis, performed with the maximum elastic interference, the interference fit has shown a safe static behaviour.

5.3.1.4 FEM contact pressure assessment

The FEM contact pressure assessment has been performed by using the minimum elastic interference, for being sure that the minimum average contact pressure is guaranteed all over the contact surface. Using the elastic interference instead of the ISO interference (that takes into account the roughness) makes this analysis more conservative. The model of the coupling is the same used in the precedent paragraph (5.3.1.3), except for the external radius on the shaft that in this case must provide the minimum elastic interference instead of the maximum one.
The minimum elastic interference and the external shaft radius and internal hub radius are reported below.

$$i_{min,el} = i_{min,ISO} - (2Ra_s + 2Ra_h) = 68\,\mu m$$

$$hub: r_{h,i} = \frac{d_n}{2} = 15\,mm \qquad shaft: r_{s,e} = \frac{d_n}{2} + \frac{i_{max,el}}{2} = 15.034\,mm$$

The sketches of the axisymmetric section of the shaft and of the hub, with the dimensions reported, are reported in the following figure (Figure 43).

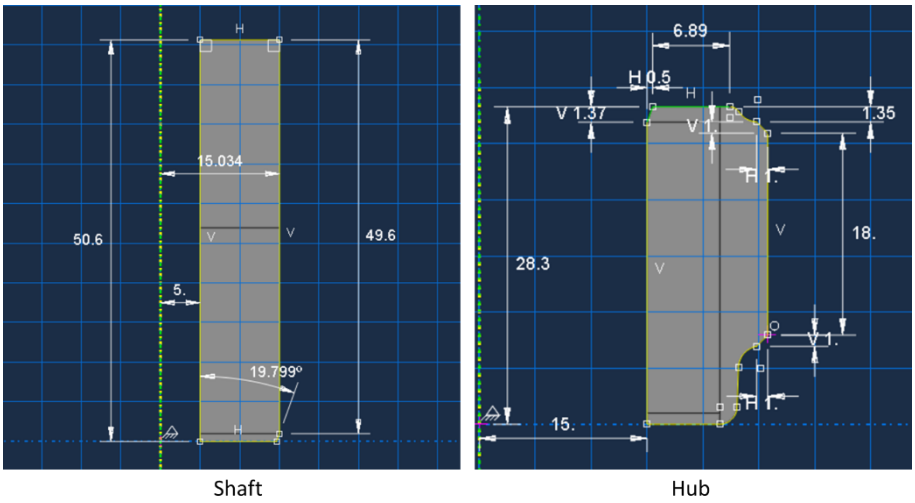

Figure 43 - Sketches of the axisymmetric section of the shaft and of the hub used in the FEM contact pressure assessment

The elements type used is CAX4R (A 4-node bilinear axisymmetric quadrilateral, reduced integration, hourglass control). The meshed model is shown in the following picture (Figure 44).

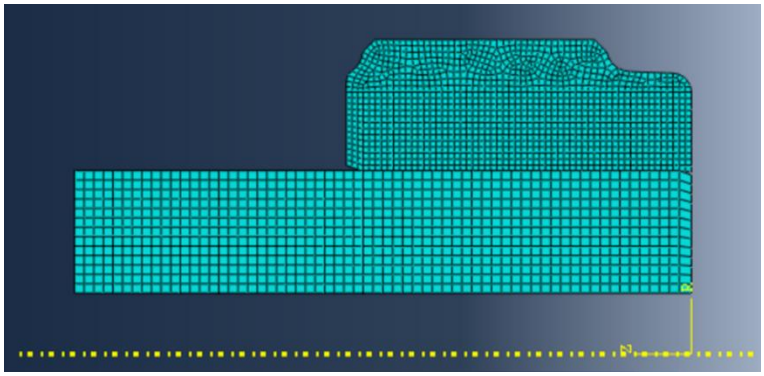

Figure 44 – Meshed model used for the FEM contact pressure assessment

The radial stress (S11 in this case) behaviour, found as a result of the FEM analysis, is shown in Figure 45.

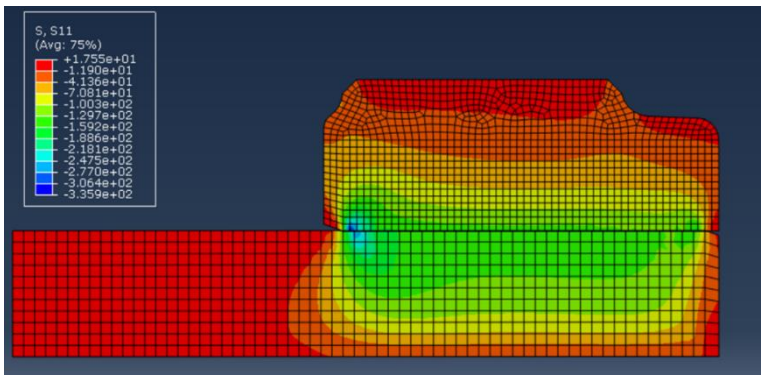

Figure 45 – Radial stress S11 found as a result from the FEM analysis with the minimum elastic interference

For the evaluation of the contact pressure, which is given by the radial stress on the contact surface, a path (Figure 46) has been implemented on the contact surface of the hub (if the path was implemented on the contact surface of the shaft the results would be the same for equilibrium).

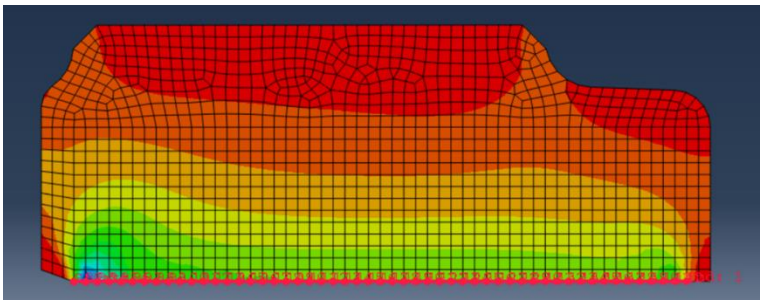

Figure 46 – Path implemented on the contact surface of the hub, used for the extraction of the radial stress S11

The real and average radial stress taken from the path is reported and compared with the minimum needed pressure in the following graph (Figure 47).

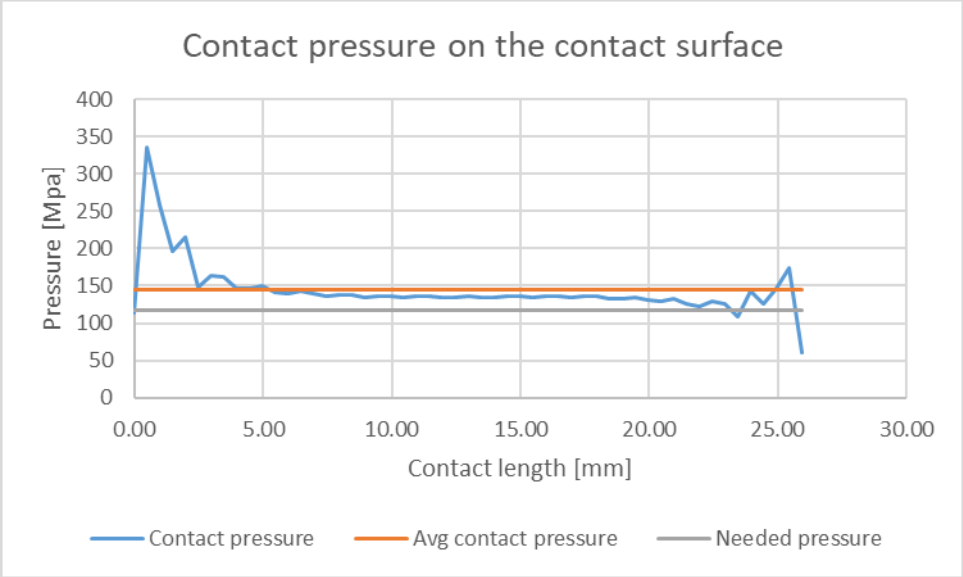

Figure 47 – Contact pressure trend with the minimum elastic interference

From the above graph, it is possible to see that the average contact pressure in higher than the minimum needed pressure (that has been doubled respect to the real needed value) but also the real contact pressure in higher than the needed one all over the contact surface. This means that the coupling can transmit the maximum torque.
The average contact pressure, the needed pressure and the doubled needed pressure (that is the one reported in the above graph) are in Table 14.

Table 14 – Contact pressure on the contact surface of the hub

Contact pressure on the contact surface of the hub		
Average contact pressure	Needed contact pressure	Doubled needed contact pressure
144 MPa	59 MPa	118 MPa

5.3.2 Static assessment of the crankshaft

The static assessment of the crankshaft is the procedure that ensure that the component works into the elastic field and so its integrity when the maximum loads are applied. So, since the forces are a function of the crank angle, it is necessary to find the most critical case. For better understanding the situation, the trend of the variable forces (those coming from the rod) as a function of the crank angle is reported in Figure 48, for the regime of 4000 rpm.

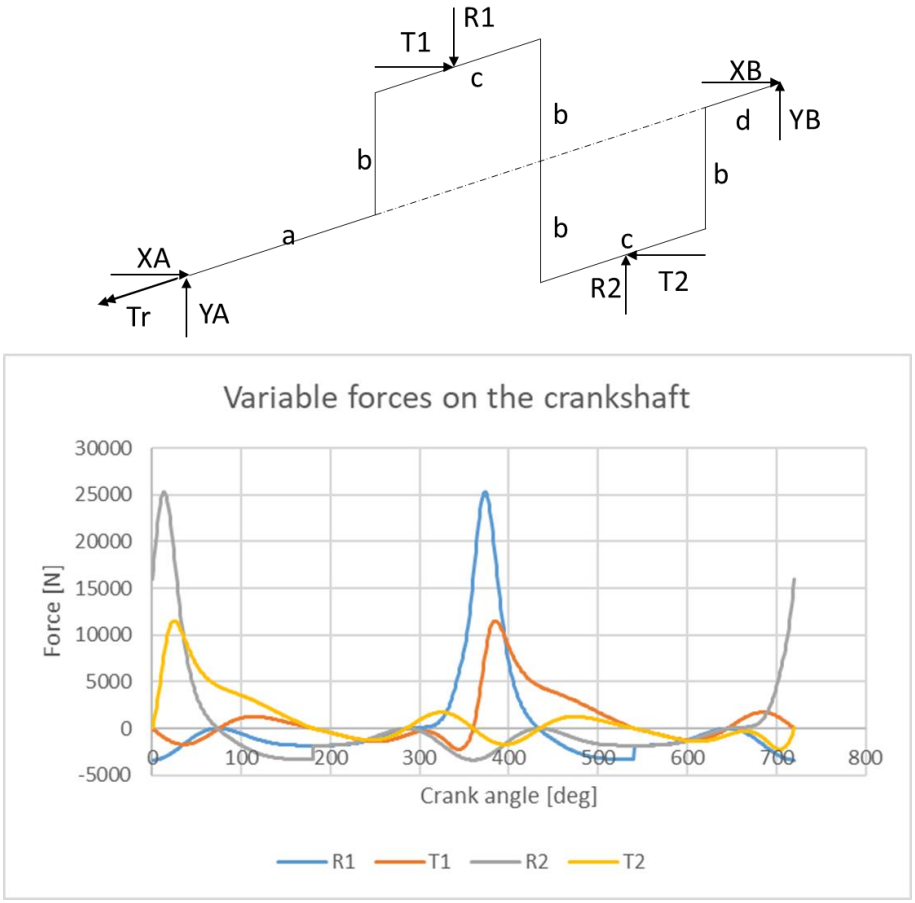

Figure 48 - Variable forces on the crankshaft @ 4000 rpm

As it is possible to understand from the above figure, the index 1 refers to the piston that acts on the posterior crank, while the index 2 refers to the piston that acts on the anterior crank.

The selected cases for the static assessments are those in which the forces assume the absolute maximum value. In particular, there are four critical situations, that are reported in the following table (Table 15).

Table 15 – Values of the forces of the critical cases

Critical cases used for the static assessment				
Crank angle [deg]	R1 [N]	T1 [N]	R2 [N]	T2 [N]
14	-3066.8	-1004.46	25266.31	8275.393
25	-2442.77	-1540.47	18230.87	11496.81
374	25266.31	8275.393	-3066.8	-1004.46
385	18230.87	11496.81	-2442.77	-1540.47

The values of the forces in the table have been taken from an Excel sheet and the cells highlighted are those who contain maximum absolute value for the related crank angle, and so are the reason of the selection of this latter one. In a nutshell: the crank angle of 14° has been selected because R2 reaches its maximum value, 25° has been selected because T2 reaches its maximum value, 374° has been selected because R1 reaches its maximum value and 385° has been selected because T1 reaches its maximum value.
Those forces do not take into consideration the contribution of the centrifugal force, so also this latter must be considered separately. Differently from what has been done in the force paragraph (5.2.2), the contribution of the crank plus the rod and the contribution of the equilibrium mass will be treated independently, for a more accurate assessment. The situation described is shown in Figure 49.

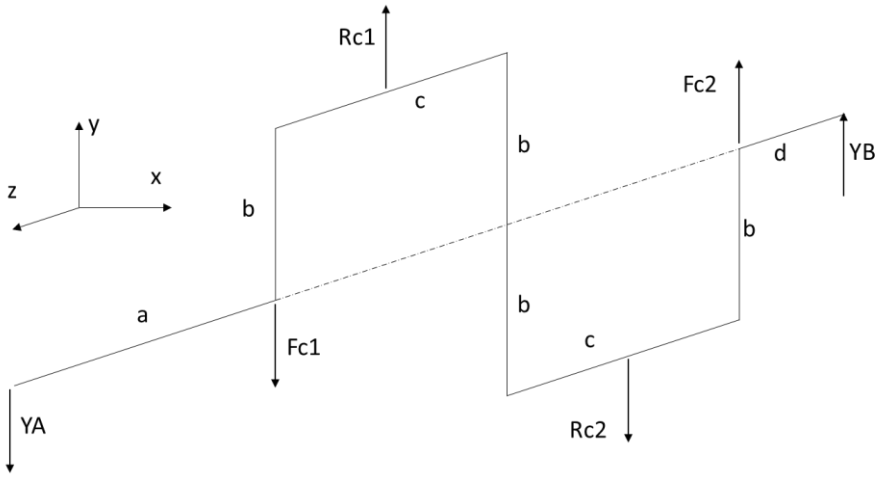

Figure 49 - Centrifugal forces on the crankshaft @ 4000 rpm

Remembering that the equilibrium masses that generate Fc1 and Fc2 are equal to 0.827 kg each one and the masses of the crank plus the rotational masses of the rod that generate Rc1 and Rc2 are equal to 0.412 kg each one, and that the crankshaft is spinning at 4000 rpm (419 rad/s), the values of the centrifugal forces are:

$$F_{c1} = F_{c2} = m_{eqm}\omega^2 r_w = 1065\ N$$

$$R_{c1} = R_{c2} = \left(m_{crank} + m_{rod,r}\right)\omega^2 r = 2218\ N$$

In the FEM analysis the centrifugal force is better implemented in a more accurate way, since by defining the density of the material and the rotational speed of the crankshaft, the software automatically assigns a centrifugal contribution to each node.

5.3.3 FE model of the crankshaft

In this paragraph, it is explained how the FE model of the crankshaft has been implemented in the FE software, that is Abaqus. In particular, the principal features of the model are explained here, those that are common in all the assessments that use this model. All the modifies to the here explained model will be specified when necessary.
For defining the model, the components of the crankshaft, that are the posterior crank, the central part of the crankshaft and the anterior crank, have been imported as parts from the CAD software (SolidWorks) to the FE software (Abaqus), in ".Step" format. They are shown in Figure 50.

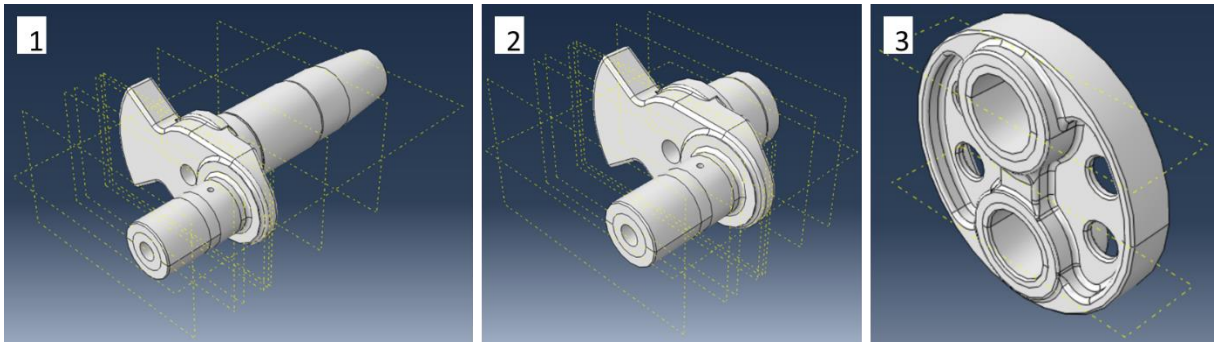

Figure 50 – Imported models of the posterior crankshaft (1), the anterior crankshaft (2) and the central part of the crankshaft (3)

The posterior and the anterior cranks are joined by means of interference fit to the central part of the crankshaft, and so the diameter of the holes of this latter component has been changed in the CAD software (before the importation), in order to provide the whole interference. The cases under analysis are two, the one with consider the maximum elastic interference, used for both the static and fatigue analysis and the one with the minimum elastic interference, used for the evaluation of the coupling state (absence of slippage). For the maximum elastic interference case (109 μm), the diameter of the holes is reduced from the nominal value, that is 30 mm, to 29.891 mm, while for the minimum elastic interference case (68 μm) the diameter is reduced to 29.932 mm. The coupling in Abaqus has been performed in the same way for both cases. All the other dimensions are the nominal ones. The drawings of the central part of the crankshaft, with the diameter of the holes in the two cases, are reported in Figure 51.

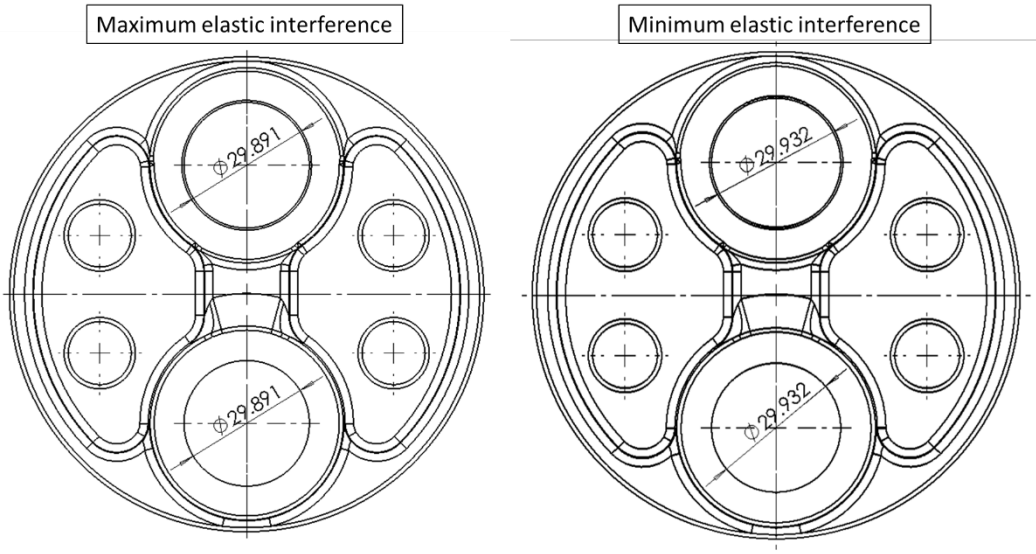

Figure 51 – Dimensions of the diameters of the two holes in the case of maximum elastic interference and minimum elastic interference

A very important thing to underline is that it has been necessary to partition in more cells all the components, for delimiting both some important surfaces (such as those used in the interaction section) and the critical zones that need a very fine mesh and a certain kind of reliable elements. The partitioning of the components has been done iteratively, by looking at the most stressed zones until an acceptable precision arose. The partition done since the first analysis are those related to the contact surfaces and to the constraint and forces distribution.

The material characteristics assigned for this analysis are both elastic properties (Young modulus and Poisson's ratio) and density, simulating the steel properties. The values used as input for the FE software are reported in the following table (Table 16).

Table 16 – Material properties used for the FEM analysis of the crankshaft

Material properties of the crankshaft			
Parameter	**Variable name**	**Value**	**Unit**
Young modulus	E	207000	MPa
Poisson's ratio	v	0.3	-
Density	ρ	7.8e-9	ton/mm^3

This material has been assigned to the whole model. No plastic properties, such as the yielding strength, has been defined, because the analysis is fully elastic. The density of the material is useful for the definition of the centrifugal force, as it will be shown later on. Once the material properties have been defined, the components have to be assembled in the assembly section, by putting them in the proper position to compose the complete crankshaft. In Figure 52 is reported the assembled model of the crankshaft.

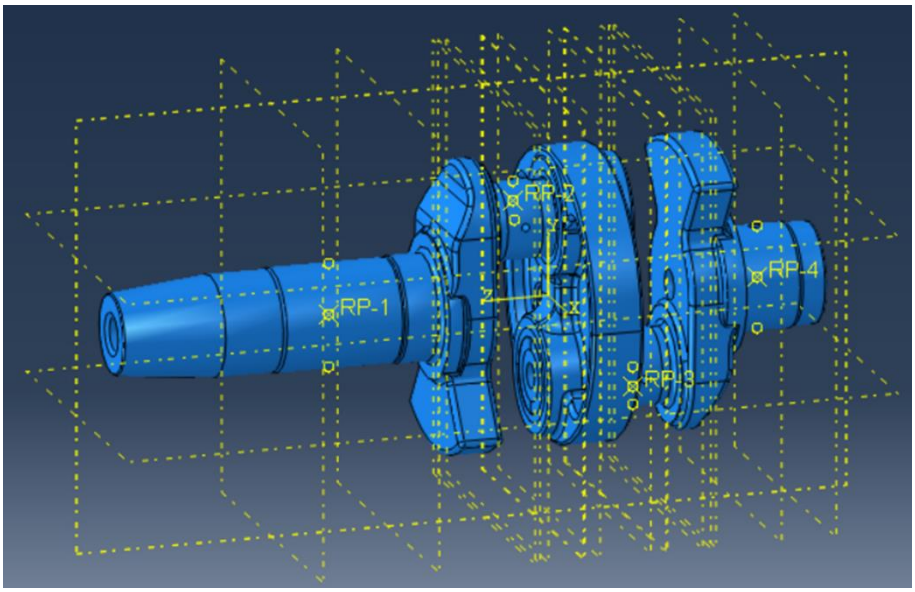

Figure 52 – Assembled model of the crankshaft

Then, two static general steps have been created, one only for the interference and one only for the rotation load, that are common for all the FEM analysis performed on the crankshaft. Each step is based on the precedence, in order to obtain the effects superposition. These two operations (the interference and the rotation) have been divided among the steps (and not all put in only one static general step) for avoiding computational error. Indeed, in the first attempt, the interference and the rotation were in the same static general step, and the software was not able to process the model.

After the definition of the steps, it has been necessary to proceed to the interaction section, for modelling the interference fit and for defining the zones in which the forces and the constrain are distributed. Indeed, the loads and the constants are not concentrated in points, as assumed in the analytic static strength assessment (to consider the forces as concentrated in points has given a more conservative result).

The two interference fit interactions have been modelled as a surface to surface contact in the first crated step (named Interference). The surface involved are the external

surfaces of the crank pins and the internal surfaces of the holes of the central part of the crankshaft. An example of this coupling is shown for the posterior crank, for which the external surface of the crank pin is set as slave surface, while the internal surface of the related hole of the central part of the crankshaft is set as master surface. The two surfaces are shown in Figure 53.

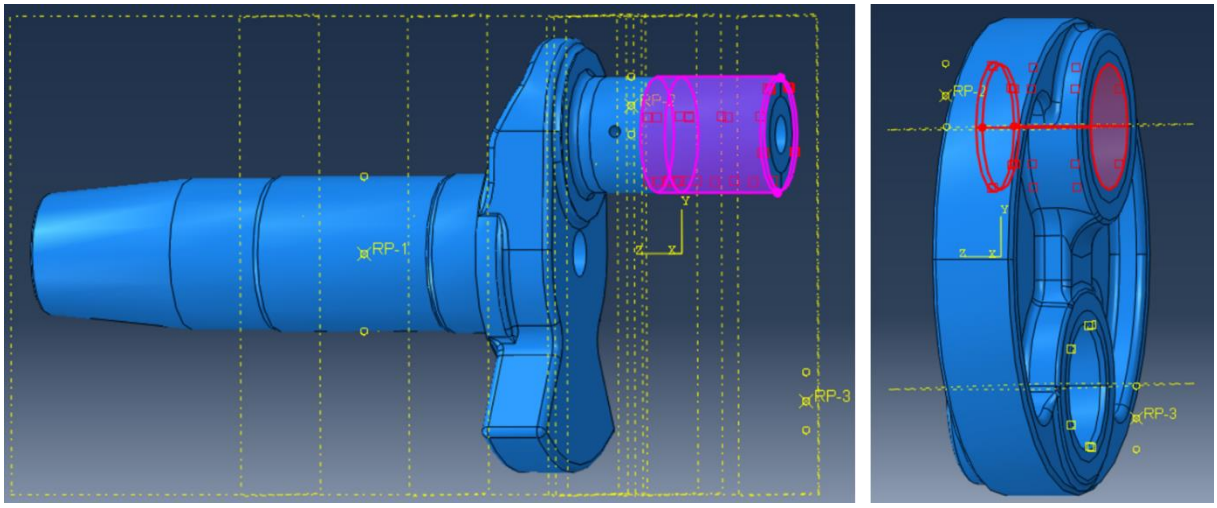

Figure 53 – Slave surface of the posterior crank pin (purple area on the left component) and master surface of the hole of the central part of the crankshaft (red area on the right component)

A section view of the coupling among the posterior crank and the central part of the crankshaft is shown Figure 54.

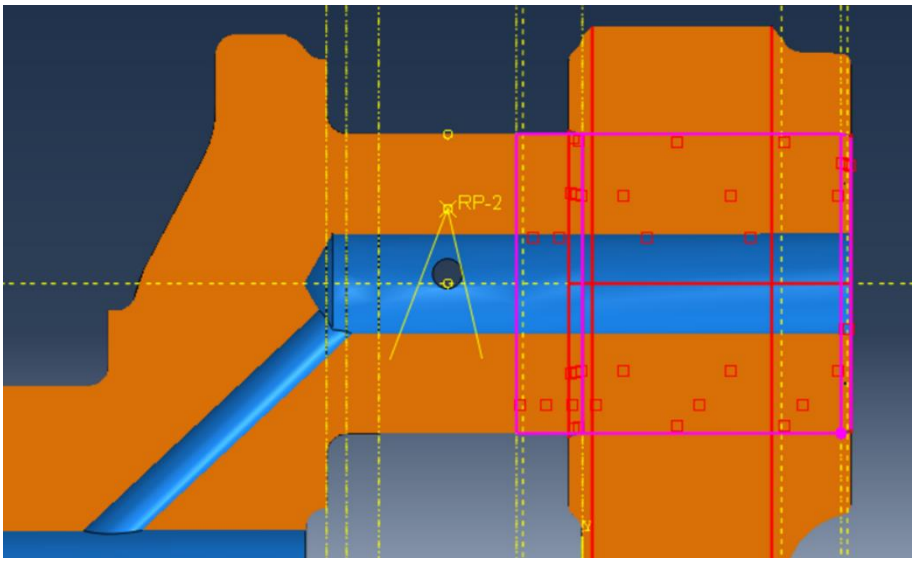

Figure 54 – Section view of the coupling among the posterior crank and the central part of the shaft

The properties of this interaction have been defined both for the tangential behaviour and for the normal behaviour. Concerning the tangential behaviour, it is necessary to specify that there is friction among the two components, and it has been implemented by the penalty friction formulation (Figure 55). The normal behaviour has been defined as an “Hard” contact, leaving all the parameters at their default status (Figure 55).

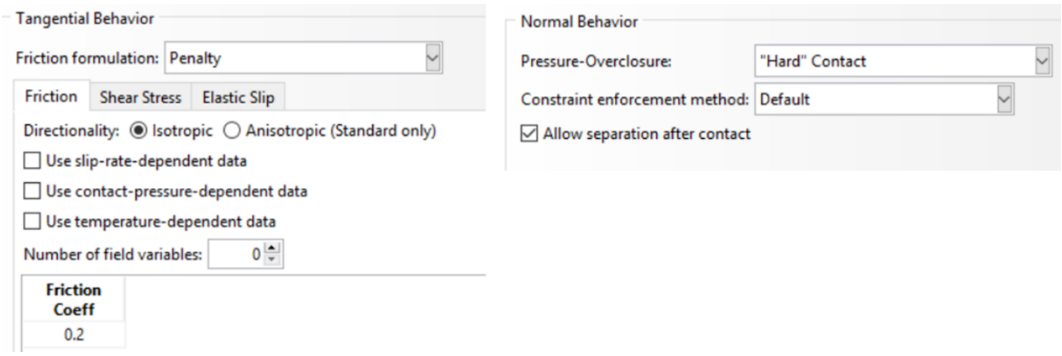

Figure 55 – Interaction properties defined for the interference fit

This procedure also applies for the interference fit between the pin of the anterior crank and the related hole of the central part of the crankshaft.
After the definition of the interference fit, some couplings among reference points and surfaces have been created. The aim of these couplings is to distribute the constraints of the crankshaft and the loads over a defined surface. The surface selected for the constraints is simply the surface of the bushing bearings of the bench while the surface selected for the loads is the surface of the bushing bearing of the head of the rod. The bushing bearings of the crankshaft are shown in Figure 56.

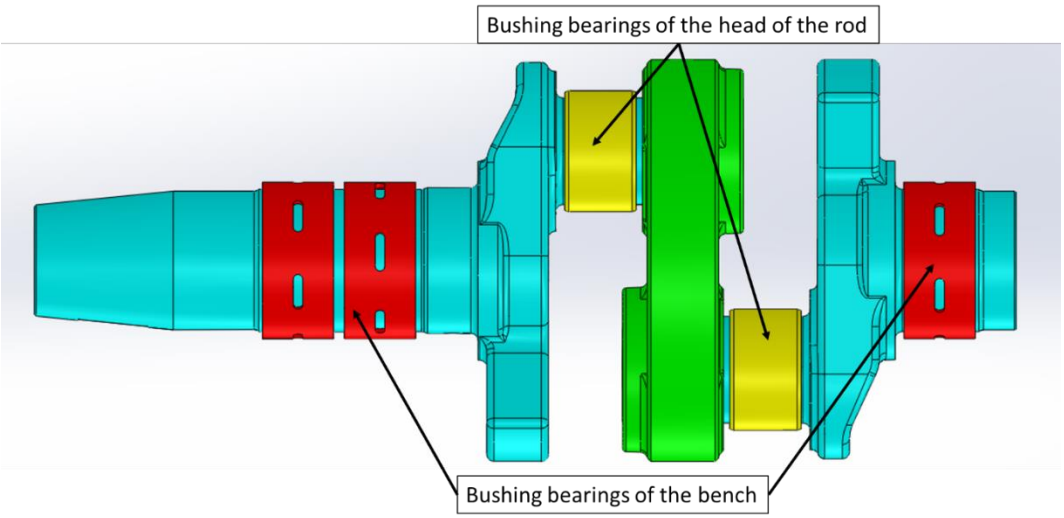

Figure 56 – Bushing bearings of the crankshaft that have been modelled in the FE model

For modelling the coupling, four reference points have been positioned in the middle of the zones that represent the bushing bearings, in which the boundary conditions and the loads will be applied. These reference points have been coupled with delimited surfaces, for distributing the constraints and the loads. In Figure 57 the position of the reference points and their related surfaces are illustrated. For being more conservative, the surface on which the loads are downloaded on the crankpin is lower than the real one. Moreover, all the coupling types are the kinematic.

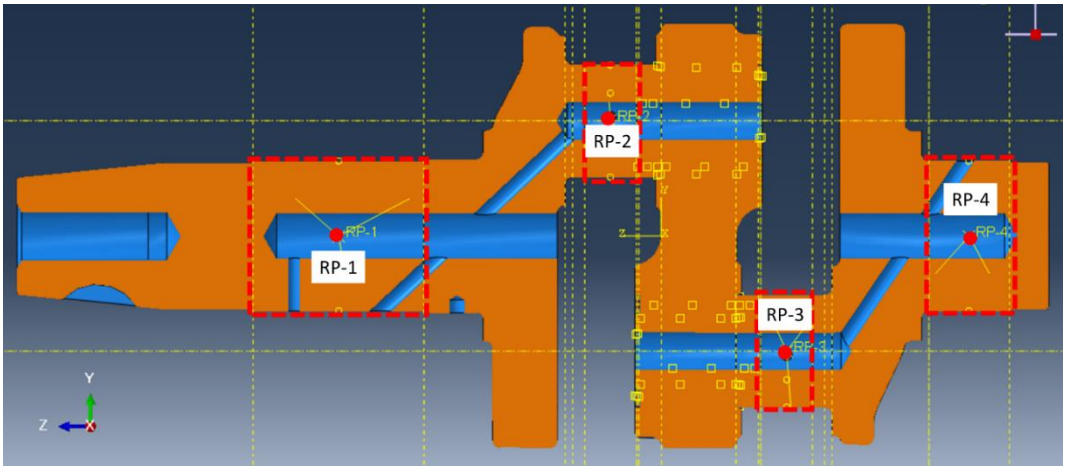

Figure 57 – Section view of the crankshaft in Abaqus, with the four reference points (red dots) coupled with their related surface (red dashed lines)

In the load section of Abaqus, both the boundary conditions and the loads have been defined, applying them to the reference points previously created. The boundary conditions have been applied to the reference point 1 (RP-1) and 4 (RP-4), in the initial step. In RP-1 the degrees of freedom constrained are the transversals (U1 is the x direction and U2 is the y direction), for simulating the roller behaviour, and the torque (UR3) for simulating the resistance torque (Figure 58).

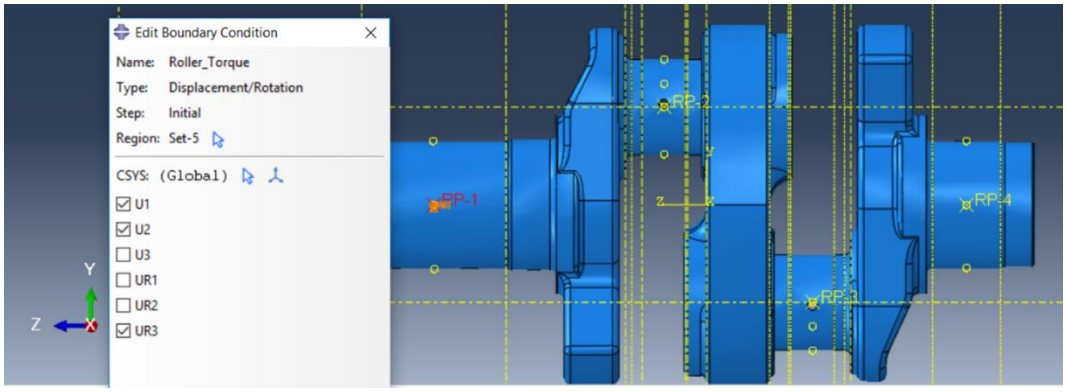

Figure 58 – Boundary condition positioned in RP-1 that simulates the roller (U1 and U2 blocked) and the resistance torque (UR3 blocked)

In RP-2 the degrees of freedom constrained are the two transversals (U1 and U2) and the axial one (U3), in order to simulate an hinge behaviour (Figure 59).

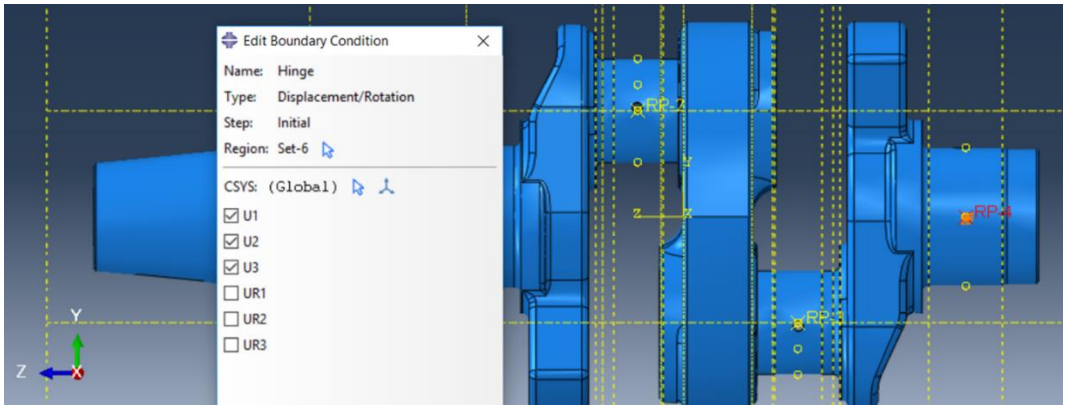

Figure 59 – Boundary condition positioned in RP-4 that simulates the hinge (U1, U2 and U3 blocked)

The loads that have been applied to the crankshaft FE model are the centrifugal force and those coming from the rods.
The centrifugal force has been implemented in the step that follows the interference step, by giving to the software the rotational speed and the axis of rotation to the FE software. The selected type of load is “Rotational body force”, and it requires the density of the material (defined with the material features), the axis of rotation and the angular speed. In Figure 60 the definition of this kind of load is illustrated.

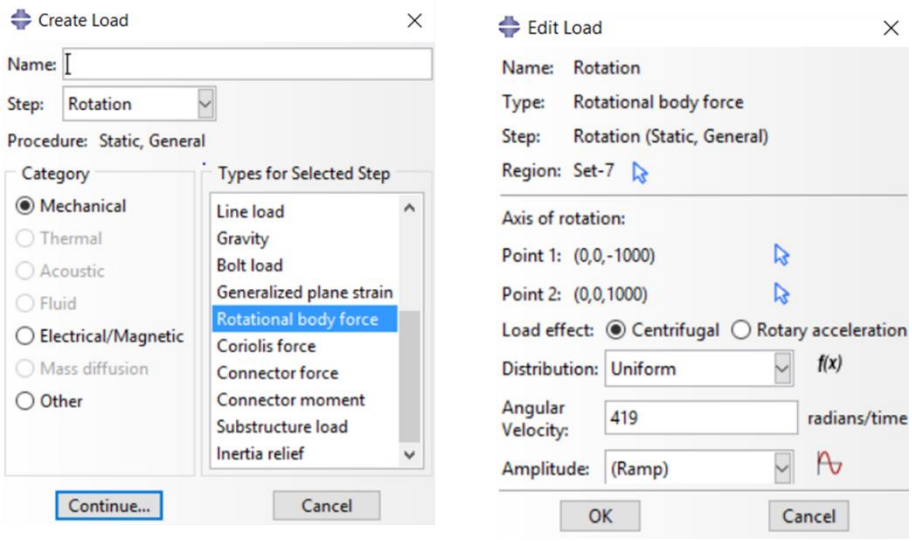

Figure 60 – Definition of the centrifugal force in the Rotation step, selecting the “Rotational body force” on the left and writing in the angular speed of 419 rad/s on the right

The centrifugal force is in this way applied on each element of the FE model, and not in determined points as in the beam model used for the analytical calculation. Due to this the results will be for sure more accurate from this perspective. This load applies for all the analysis performed with the FE model of the crankshaft. The appearance of the centrifugal force on the FE model is shown in Figure 61.

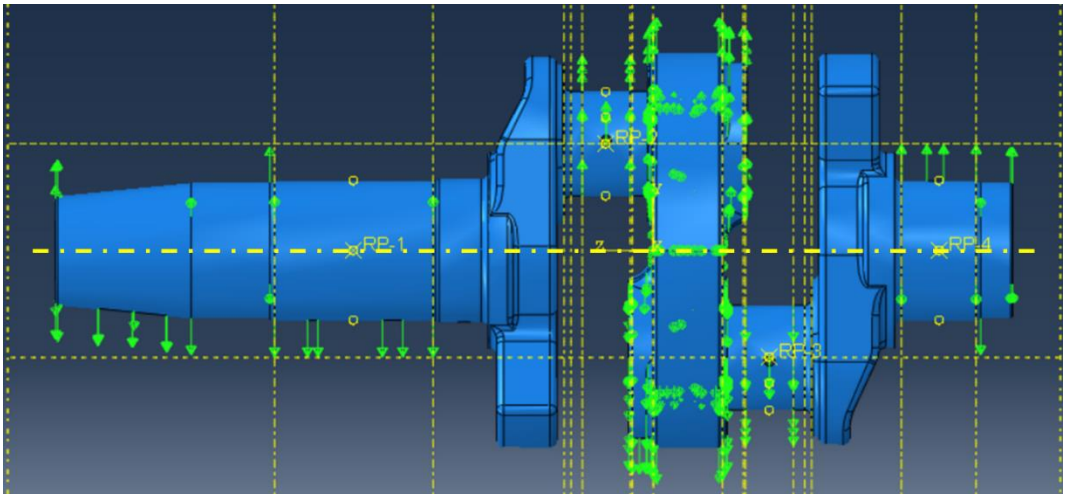

Figure 61 – Centrifugal force that appears on the model after the definition of this type of load

The forces coming from the rods, are defined as concentrated loads, because they have been directly applied to the reference point 2 (RP-2) and 3 (RP-3). Since this model has been used for analysing different loads configurations, each one representing a crank

angle, different steps have been created for the different load configuration. In particular, the crank angles simulated are reported in Table 17, specifying for which analysis have been used.

Table 17 – Crank angles used for the different analysis

Crank angle [deg]	Static assessment	Fatigue assessment	Slippage assessment
0	✗	✓	✗
14	✗	✓	✗
25	✗	✗	✓
180	✗	✓	✗
360	✗	✓	✗
374	✓	✓	✗

The forces that act on the pin of the posterior crank are named R1 and T1, while the force that act on the other pin are R2 and T2. Their values, related to the crank angles/steps, is reported in Table 18. The signs of the forces are coherent with the global reference system of Abaqus.

Table 18 – Values of the loads used in the different FEM analysis

Crank angle [deg]	R1 [N]	T1 [N]	R2 [N]	T2 [N]
0	3388	0	15959	0
14	3022	-1066	25094	-8848
25	2509	-1540	19144	-11497
180	1832	-23	-1832	23
360	-15959	0	-3387.25	0
374	-25094	8848	-3022	1066

In Figure 62 an example of the FE model with the loads applied for the crank angle of 374° (the related step is named Alpha_374) is illustrated.

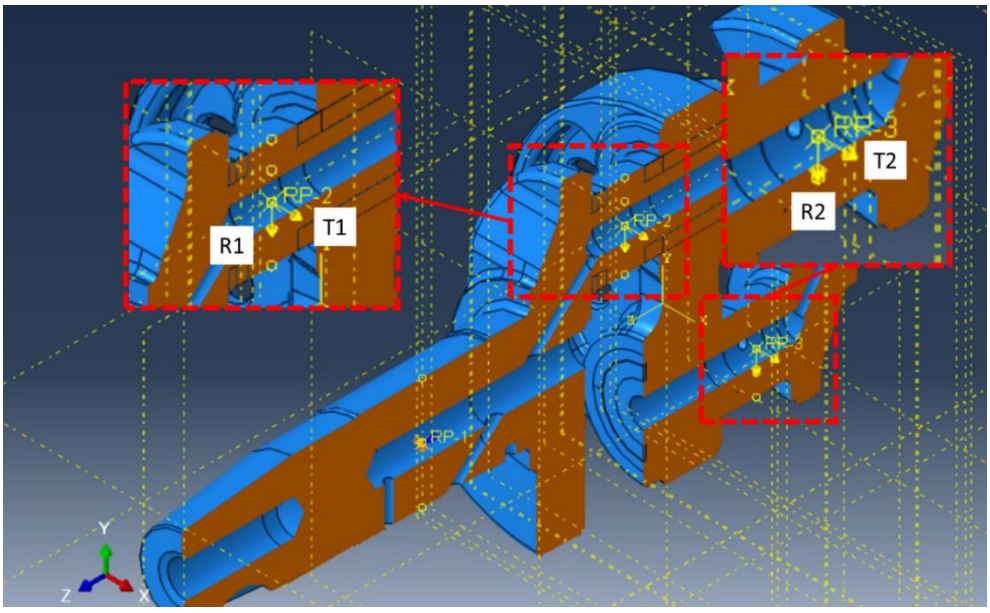

Figure 62 – FE model with the loads coming from the rods applied, in particular for the crank angle of 374° (step named Alpha_374)

Last but not the least, the elements type and the mesh have been defined for the whole model, and thanks to the partitioning of the components, it has been possible to use different elements and different mesh size for the partitions depending on their relevance. In the most relevant areas, such as the fittings, the elements used is the C3D20R (A 20-node quadratic brick, reduced integration), while in all the other zone the C3D10 (A 10-node quadratic tetrahedron) elements have been selected. In Figure 63 the different element types used are shown; the green and the yellow partitions are those for which a more precise analysis is required and so the C3D20R elements are used, while in the remaining cells (pink coloured) C3D10 elements are used.

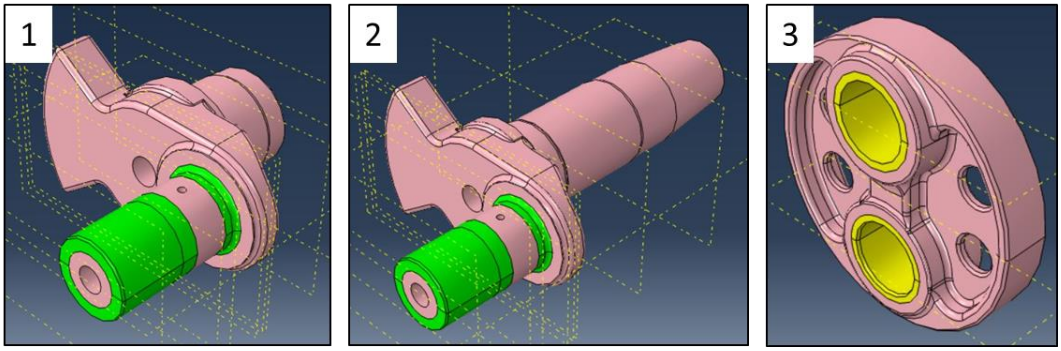

Figure 63 – Elements type used for the components of the anterior crank (1), posterior crank (2) and the central part of the crankshaft (3); the C3D20R are the green and the yellow zones while the C3D10 are the remaining pink zones

The dimension of the mesh depends on the partition in which it applies, going from a very fine grid in the green and yellow parts to a very coarse grid in the pink parts. A picture of the meshed FE model of the pin of the posterior crank is shown in Figure 64; from that image it is noticeable how the mesh effort has been focused on the fitting radius of the pin of the crank, and vice versa how the mesh is left coarse in the other parts.

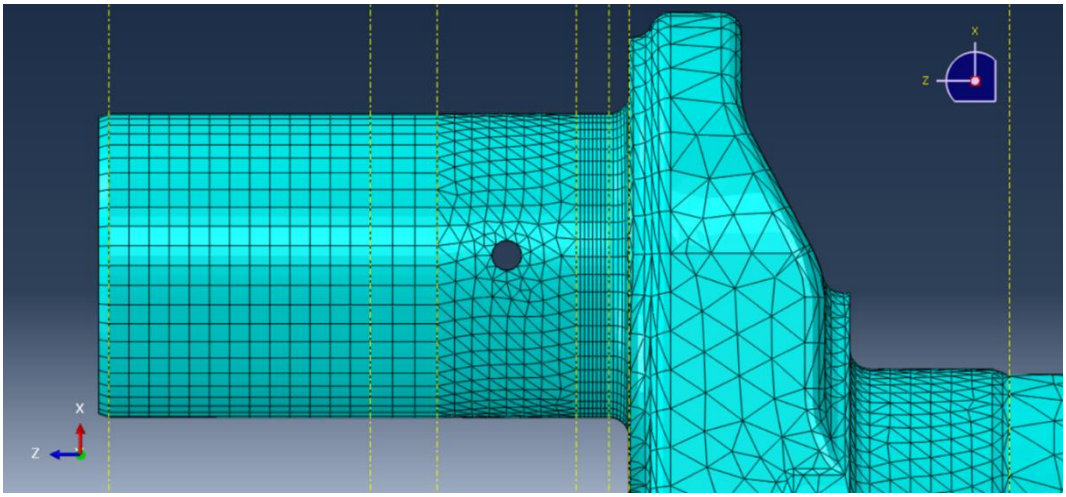

Figure 64 – Example of how the mesh has been implemented for the pin of the posterior crank

The FE model of the crankshaft, described up to now, has been developed iteratively during the FEM analysis phase, in order to obtain the best results in the zones of interest.

5.3.3.1 Analytical static strength assessment

The analytical static assessment has been performed as a preliminary analysis of the crankshaft, to assess that the section of the cranks (where the forces coming from the rod are applied) is not undersized and to identify the most critical loads condition. For the assessment, the beam model of the crankshaft has been used, and the internal actions have been computed for the 4 critical cases. In Figure 65 it is shown the beam model of the crankshaft, with all the loads applied and for a generic crank angle. The direction of the centrifugal forces Fcs and Rcs does not change during time, as well as their value (for a constant rotational speed), while the direction of all the other forces do; this means that when R1, T1, R2, T2 have positive sign, their direction is concord with the one reported in Figure 65 and vice versa, while the Fcs have the direction of Figure 65 independently from their sign.

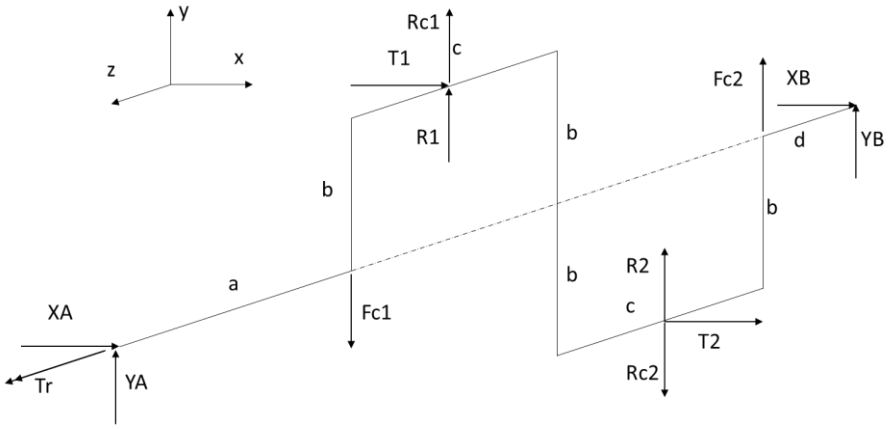

Figure 65 - Beam model of the crankshaft for a generic crank angle, with the loads applied.

The assessment has been performed only for the cranks (where the rod delivers the force) because they are the most stressed zones in terms of internal actions. All the other parts of the crankshaft have been statically assessed by means of the FEM analysis.
For the calculation of the internal actions, the forces have been divided among those that act in x-z plane and those that act in the y-z plane. Moreover, concerning the y-z plane, the variable internal actions have been computed separately from the constant internal actions.
The first internal action that will be computed is the bending moment generated by the constant force, in the plane y-z. The beam model with the constant centrifugal force and their related internal actions is in Figure 66 while the bending moment diagram is shown in Figure 67.

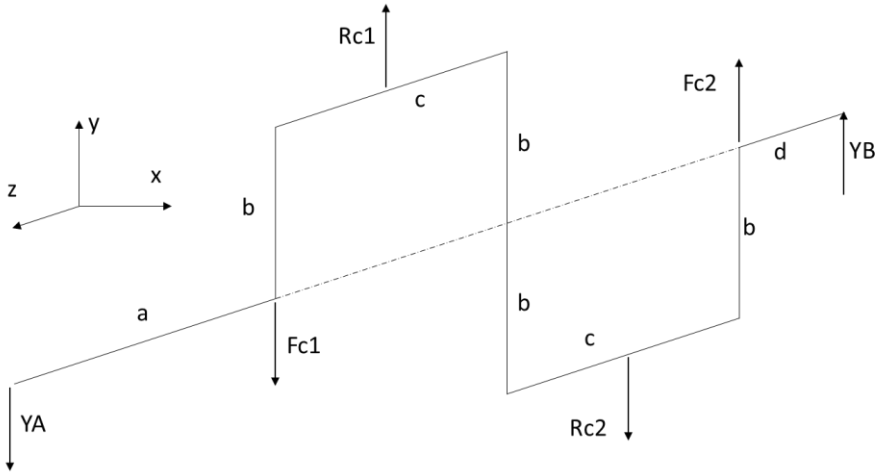

Figure 66 - Beam model of the crankshaft with the centrifugal forces applied

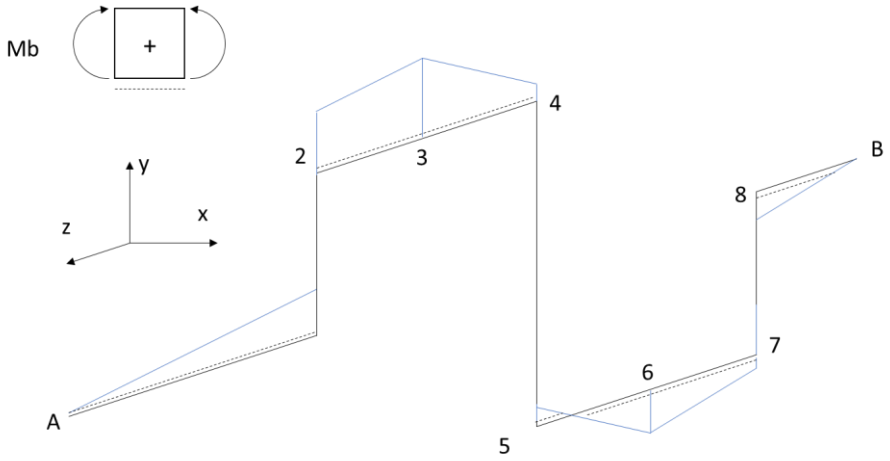

Figure 67 – Bending moment diagram related to the constant centrifugal forces

The bending moment values along the cranks, due to the constant centrifugal forces, are reported in Table 19 and the highlighted cell contains the highest one.

Table 19 – Bending moment values along the cranks due to the centrifugal forces

Bending moment along the cranks due to constant centrifugal forces						
Section point	2	3	4	5	6	7
Bending moment [Nmm]	1192	26250	298	298	25653	596

Then, even in this case for the plane y-z, the bending moment has been computed for the variable force, for all the 4 critical cases.The beam model of the crankshaft for the crank angles of 14° and 25°with the variable loads applied is reported in Figure 68 and in Figure 69 is qualitatively reported its bending moment diagram.

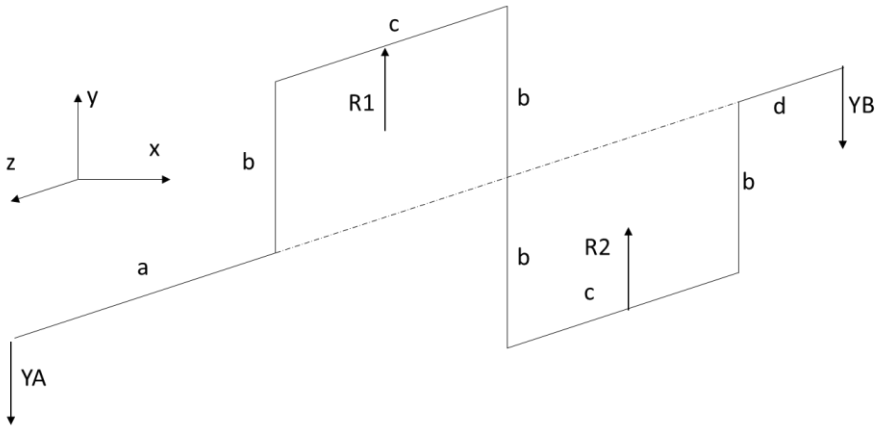

Figure 68 – Beam model of the crankshaft with the variable loads that act on the y-z plane applied, valid for the crank angles of 14° and 25°

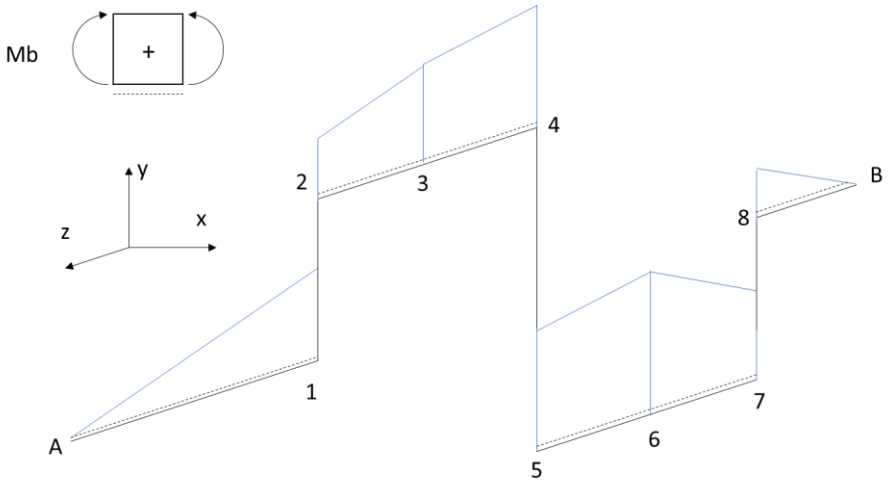

Figure 69 – Bending moment diagram in the plane y-z for the crank angles of 14° and 25°

The values of the bending moment in the two cranks for the angles of 14° and 25° are reported in the following table (Table 20), and the highlighted are the higher for the given angles.

Table 20 – Bending moments along the cranks for the crank angles of 14° and 25°

Bending moment [Nmm] along the cranks for crank angle of 14° and 25°						
Section point	2	3	4	5	6	7
α=14°	440229	646867	782969	782969	919070	474047
α=25°	324012	476099	572002	572002	667905	344499

The beam model of the crankshaft for the crank angles of 374° and 385°with the variable loads applied is reported in Figure 68 and in Figure 69 is qualitatively reported its bending moment diagram.

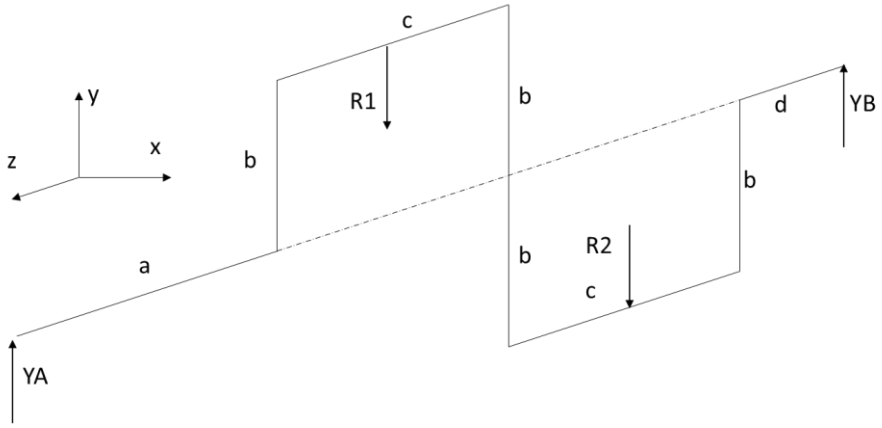

Figure 70 – Beam model of the crankshaft with the variable loads that act on the y-z plane applied, valid for the crank angles of 374° and 385°

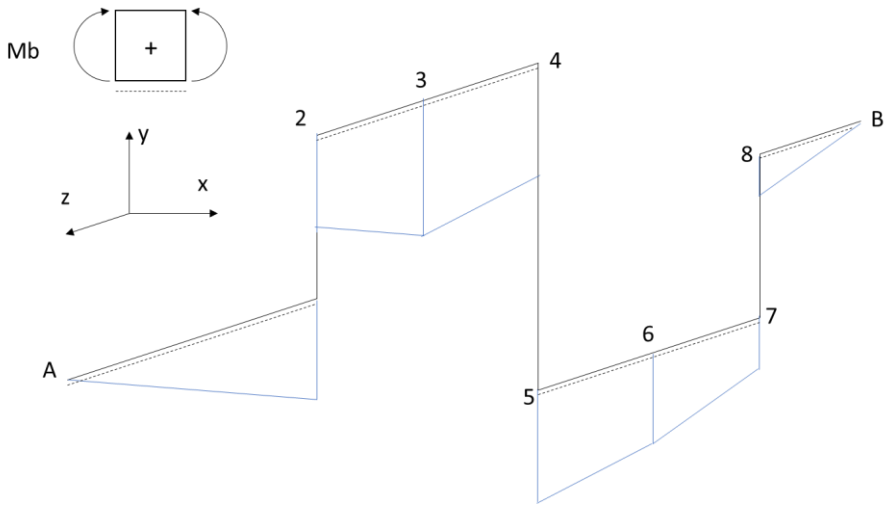

Figure 71 – Bending moment diagram in the plane y-z for the crank angles of 374° and 385°

The values of the bending moment along the cranks, for the crank angles of 374° and 385°, are reported in the following table (Table 21). The highlighted cells represent the highest values for the given crank angle in the related section point.

Table 21 – Bending moments along the cranks for the crank angles of 374° and 385°

Bending moment [Nmm] along the cranks for crank angles of 374° and 385°						
Section point	2	3	4	5	6	7
α=374°	742571	1091125	858554	858554	625983	322875
α=385°	539035	792051	625758	625758	459464	236987

The total values of the bending moments (constant contribution plus variable contribution) that act in the plane y-z are shown in the following table (Table 22).

Table 22 – Total bending moments along the cranks that act in the y-z plane

Bending moment [Nmm] of the y-z plane						
Section point	2	3	4	5	6	7
α=14°	441421	673116	783267	783267	893417	473451
α=25°	325204	502348	572300	572300	642252	343902
α=374°	741379	1064876	858256	858256	651636	323471
α=385°	537843	765802	625460	625460	485118	237583

From the previous table it is noticeable that the constant contribution of the centrifugal forces is almost negligible respect to the variable bending moments. Indeed, the highest values (highlighted cells) remain the same.
The internal actions in terms of bending moment have also been calculated in the plane x-z, considering only the variable contribution of T1 and T2.
Even in this case the bending moment has been evaluated in the most critical case and so for the crank angles of 14°, 25°, 374°, 385°. It is to be noted that the resistance torque will not be reported in the following beam models because it is useless for the evaluation of the bending moments along the cranks (it will be useful later on).
The beam model of the crankshaft for the crank angle of 14° and 25° with the forces that act in the x-z plane is reported in Figure 72 while the bending moment diagram for the same configuration is shown in Figure 73.

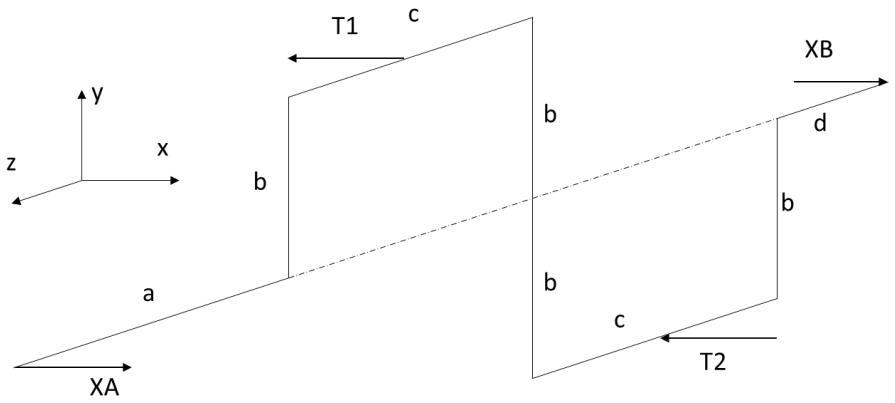

Figure 72 – Beam model of the crankshaft with the variable loads applied that act on the x-z plane applied, valid for the crank angles of 14° and 25°

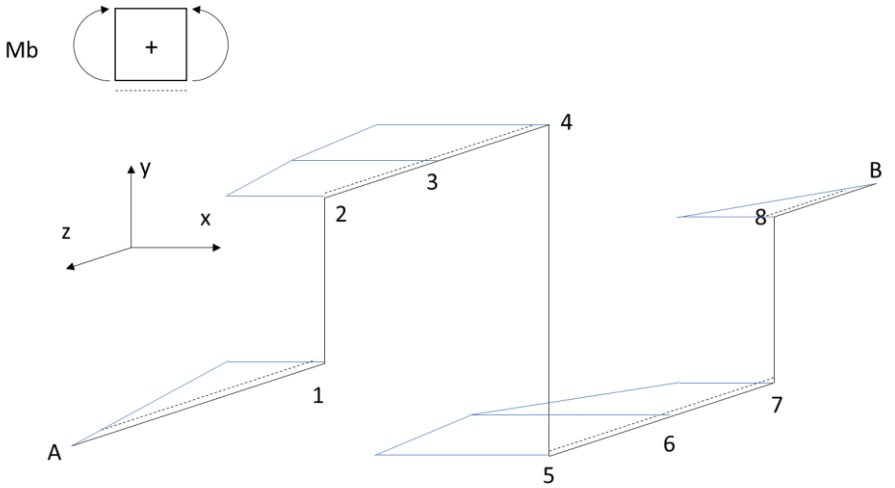

Figure 73 – Bending moment diagram in the x-z plane for the crank angles of 14° and 25°

The values of the bending moment in the x-z plane for the crank angles of 14° and 25° in the most critical points (the cranks) are reported in Table 23.

Table 23 – Values of the bending moment in the x-z plane for the crank angles of 14° and 25°

Bending moment [Nmm] along the cranks in the x-z plane for crank angles of 14° and 25°						
Section point	2	3	4	5	6	7
α=14°	144187	211866	256443	256443	301020	155263
α=25°	204329	300239	360718	360718	421197	217249

The beam model of the crankshaft for the crank angle of 374° and 385° with the forces that act in the x-z plane is reported in Figure 72 while the bending moment diagram for the same configuration is shown in Figure 75.

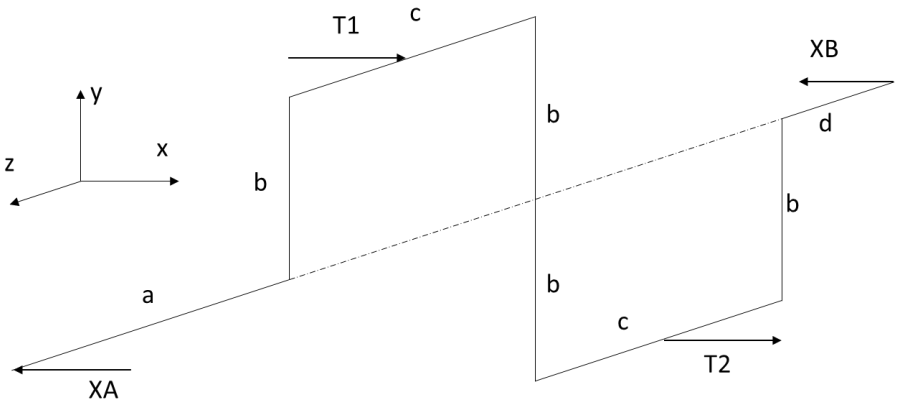

Figure 74 – Beam model of the crankshaft with the variable loads applied that act in the x-z plane for the crank angles of 374° and 385°

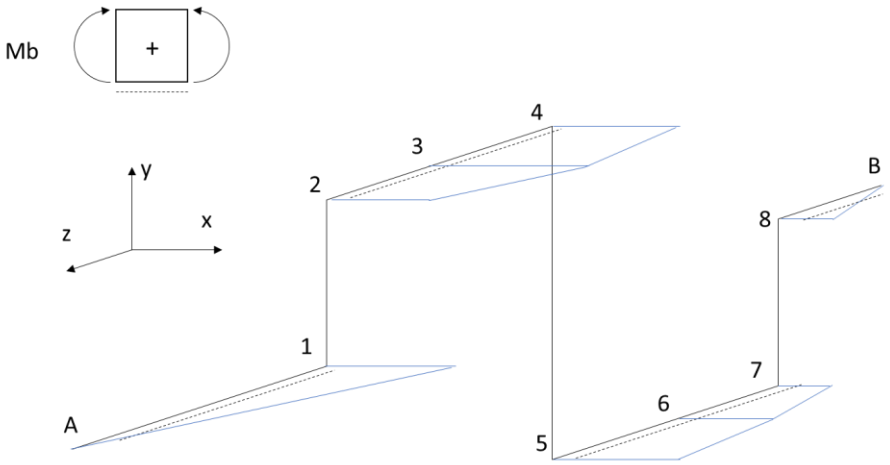

Figure 75 – Bending moment diagram in the x-z plane for the crank angles of 347° and 385°

The values of the bending moment in the x-z plane for the crank angles of 374° and 385° in the most critical points (the cranks) are reported in Table 24.

Table 24 - Values of the bending moment in the x-z plane for the crank angles of 374° and 385°

Bending moment [Nmm] along the cranks in the x-z plane for crank angles of 374° and 385°						
Section point	2	3	4	5	6	7
α=374°	243212	357373	281199	281199	205026	105750
α=385°	339928	499486	394617	394617	289749	149449

Once that all the bending moments have been evaluated for the two planes and for the most critical crank angles, the equivalent bending moment must be calculated for all the section points and for all the angles, with the Pythagoras theorem, as shown in the following formula.

$$M_{b,eq} = \sqrt{M_{b,yz}^2 + M_{b,xz}^2}$$

The equivalent bending moments are reported in the following table (Table 25).

Table 25 – Values of the equivalent bending moments along the cranks for all the crank angles

Equivalent bending moments [Nmm] along the cranks for all the crank angles						
Section point	2	3	4	5	6	7
α=14°	464373	705672	824178	824178	942765	498259
α=25°	384067	585232	676494	676494	768045	406775
α=374°	780253	1123244	903148	903148	683129	340319
α=385°	636259	914297	739542	739542	565061	280679

From the above table, it is clear that the most critical situation is the bending moment in section 3 for a crank angle of 374° (the highlighted cell in Table 25). Thus, the static analytic static assessment will be performed looking at that zone and considering a total yielding condition (without considering the stress concentration along the discontinuity). For the selected part, also the torque has been evaluated, for a more accurate analysis. The internal action of the torque, for a crank angle of 374° and given by T1 and T2, is shown in Figure 76.

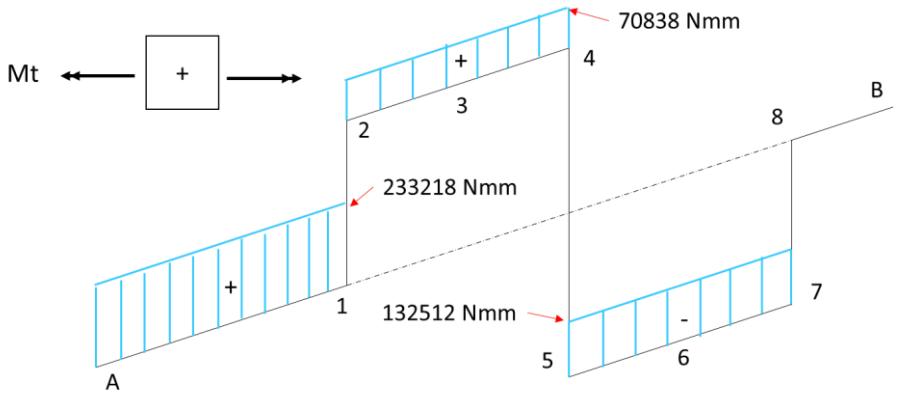

Figure 76 - Torsion diagram of the crankshaft for a crank angle of 374°

The value of the equivalent bending moment and of the torque in the section 3 are respectively:

$$M_{b,eq} = 1123244\ Nmm \qquad M_t = 70838\ Nmm$$

The dimensions and the inertia properties of the section under investigation (Figure 77) are reported in

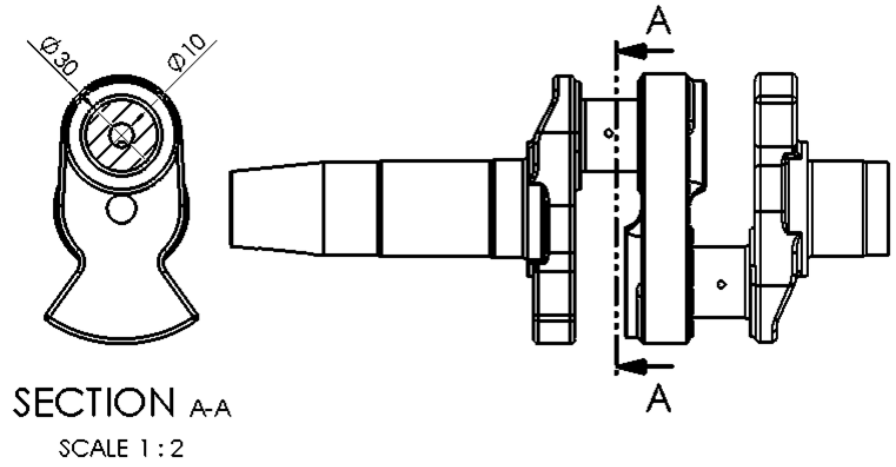

Figure 77 – Section view of the critical zone (section 3)

Table 26 – Properties of section 3

Section 3 properties			
Parameter	**Variable name**	**Value**	**Unit**
External diameter	de	30	mm
Internal diameter	di	10	mm
Moment of inertia about neutral axis	I_{xx}	39267	mm^4
Polar moment of inertia	J_p	78540	mm^4

Now, it is possible to evaluate both the normal and the shear stress in the most stressed part of section 3, which is situated on the surface of the crank, where the forces are applied. The criteria used for this static assessment is the Von Mises criteria, since the stress state is produced by a simple bending and torsion condition. The steps for the assessment, and so for the safety factor, are reported below.
The normal and the shear stresses are computed as follow.

$$\sigma_b = \frac{M_{b,eq}}{I_{xx}} \cdot \frac{d_e}{2} = 429\ MPa \qquad \tau = \frac{M_t}{J_p} \cdot \frac{d_e}{2} = 13.5\ MPa$$

Then, the Von Mises stress is calculated.

$$\sigma_{VM} = \sqrt{\sigma_b^2 + 3\tau^2} = 429.7\ MPa$$

And finally, the safety factor (remembering that the yielding strength is 735 MPa) of the section 3 considering a total yielding condition.

$$\eta = \frac{\sigma_y}{\sigma_{VM}} = 1.7$$

Since the value of the safety factor is higher than one, the crank is statically assessed.
Of course, in this analysis, the geometric discontinuities, in which the stress is concentrated, have not been taken into consideration. Due to this, a FEM analysis is mandatory for a more detailed assessment, to guarantee the integrity of the complete crankshaft.

5.3.3.2 FEM static strength assessment

The FEM static strength assessment has been performed using the FE software Abaqus, simulating the loads in the most critical case. The most critical case is the one found thanks to the analytical analysis, and in particular it is for a crank angle equal to 374°. This kind of evaluation takes into consideration all the geometrical details, since the used model is directly imported from the CAD software (SolidWorks) in ".Step" format. In this paragraph, it will be shown the FEM analysis on the crankshaft with the components at the first design attempt. Moreover, the FE model of the crankshaft is a little bit different from the one described in paragraph: the element type used in the most critical areas in the first analysis is C3D8R (An 8-node linear brick, reduced integration, hourglass control), that however are reliable elements. The last analysis is performed using C3D20R elements in the most critical zones. The result of the first static strength analysis performed by Abaqus is reported in Figure 78.

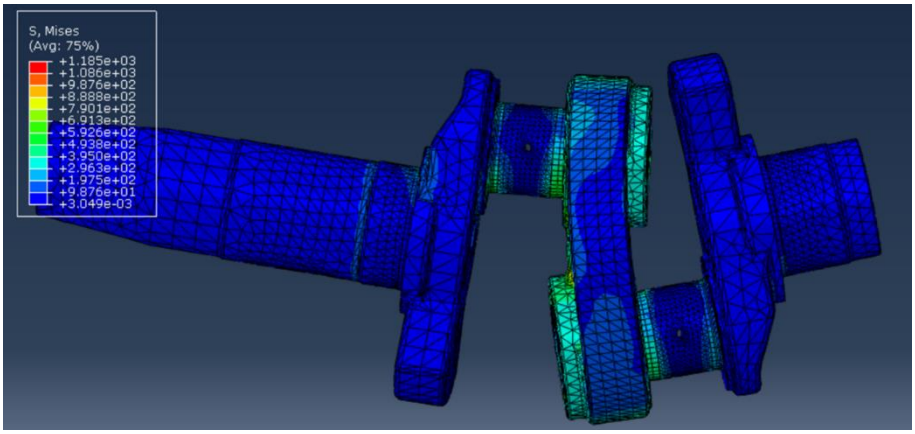

Figure 78 – FEM result of the first static strength analysis of the crankshaft

The first FEM analysis has highlighted that in all the components there are some zones in which the Von Mises stress is locally higher than the yielding strength. So, the stresses in the components will be analysed separately for better understanding some possible solutions.

POSTERIOR CRANK

The posterior crank has highlighted a Von Mises stress that is higher that the yield strength in the internal part of the crank pin. Such zone is shown in Figure 79.

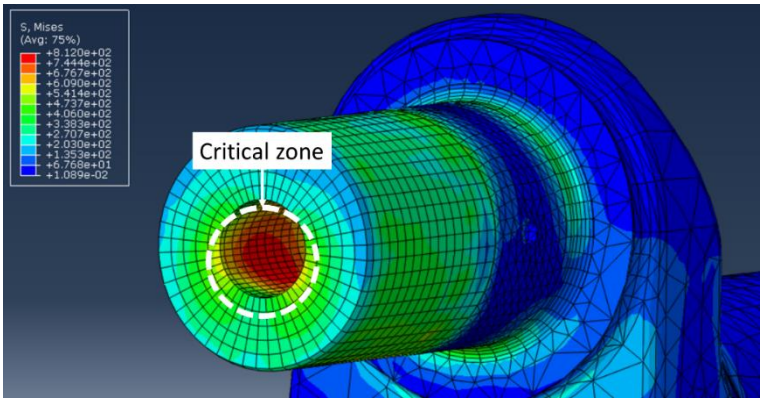

Figure 79 - Critical zone of the internal part of the posterior crank pin for a crank angle of 374°

The solution applied to the component has been to reduce the internal diameter, passing from 12 mm to 10 mm. Since the dimensions of the crank pin of the posterior and anterior cranks, the same change has been exported to the anterior crank, also because it presented the same problem. In Figure 80 is illustrated the path used for the extraction of the Von Mises stress in Abaqus, while in the graph in Figure 81 the reduction of the Von Mises stress from the first analysis (Von Mises 1) to the secondo analysis (Von Mises 2) after the changes.

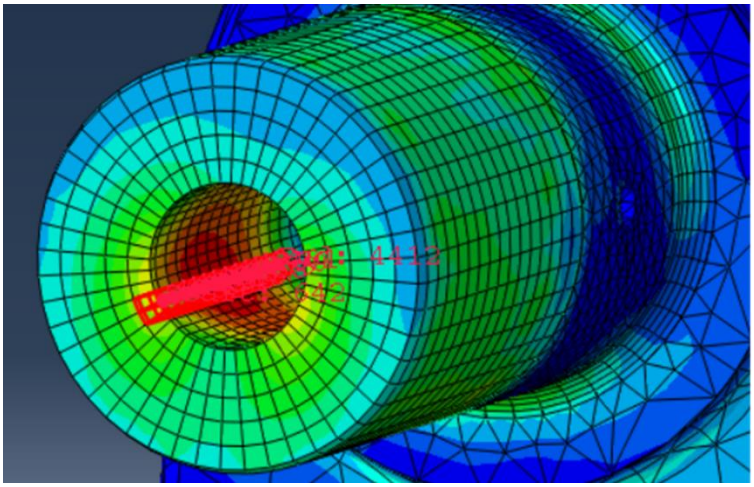

Figure 80 – Path used for the extraction of the Von Mises stress

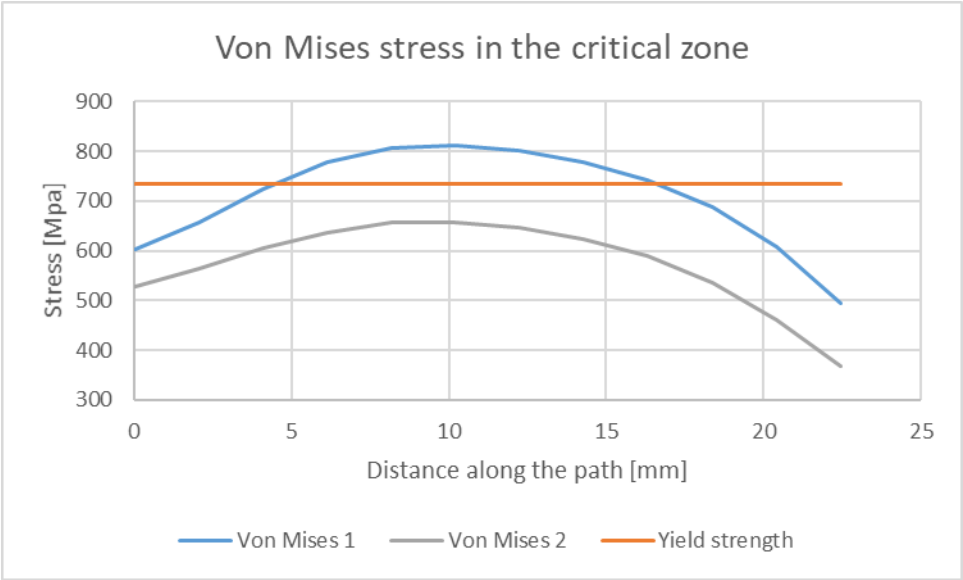

Figure 81 – Von Mises stress in the critical zone of the crank; Von Mises 1 is the stress carried out from the first analysis, while Von Mises 2 is the stress carried out from the second analysis, after the change of the internal radius

The last FEM analysis has been performed by using C3D20R elements and a refined mesh in the fillet radius zone of the pin of the crank (Figure 82). The result of such analysis shows a Von Mises stress higher than the yielding due to the notch effect.

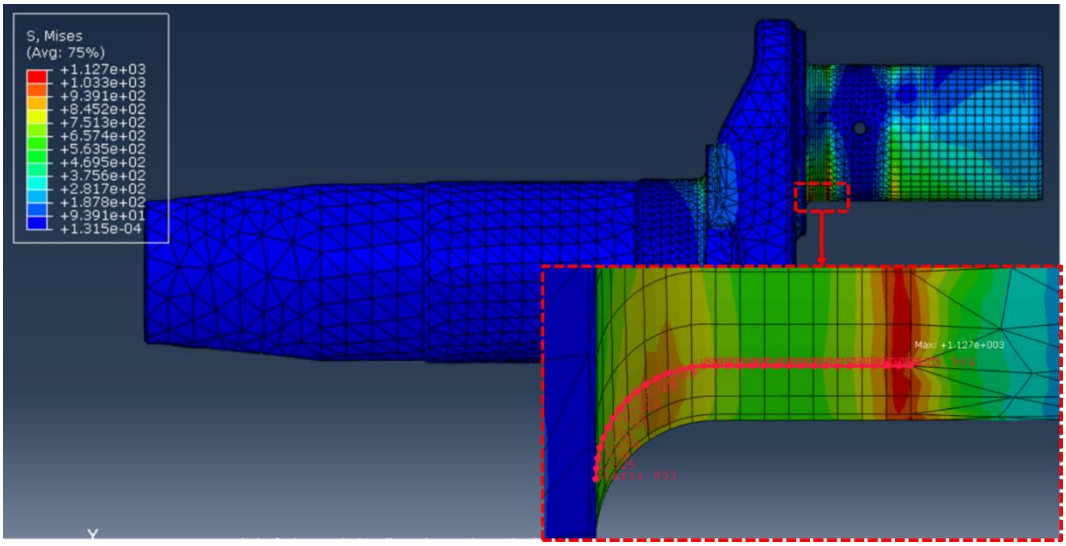

Figure 82 – Fillet radius zone of the pin of the posterior crank that shows a Von Mises stress higher that the yielding limit; moreover, the path used for the stress extraction is shown

The value of the Von Mises stress in the critical zone and taken from the path shown in Figure 82 is reported in the following graph (Figure 83).

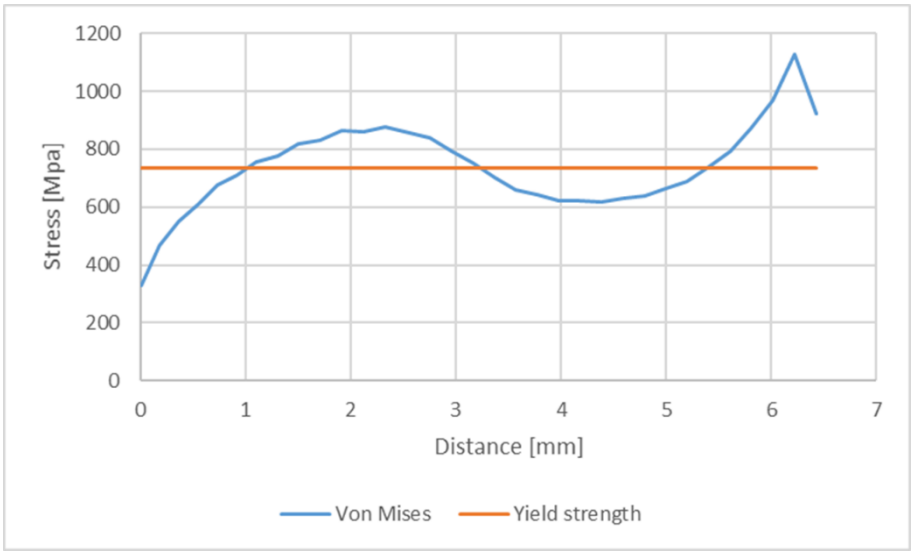

Figure 83 – Von Mises stress along the path on the fillet of the pin of the posterior crank versus the yielding limit

The left part of the graph shows the typical behaviour of the stress due to the notch effect, while on the right part there is a very sharp peak due to the kinematic coupling for the force distribution. Such a peak is not so reliable because it could be caused by a numerical error due to the sudden numerical discontinuity. Moreover, such discontinuity is in the reality given by a bushing bearing that has its own stiffness and it can not give a stress peak like that.

To solve this stress concentration due to the notch is mandatory, mainly because it is a cyclical effect and of course it will be a big problem for the fatigue life. Indeed, in this condition the component works in low cycle fatigue condition.

The principal solutions that can be adopted are two: the first is to increase the fillet radius in order to reduce the notch effect and the second is to reduce the nominal stress by increasing the moment of inertia of the section keeping constant the notch effect. Of course, a combination of both the solution can be implemented.

Among the two solutions, the best one in terms of weight saving and fatigue life is of course the first.

CENTRAL PART OF THE CRANKSHAFT

The central part has shown a Von Mises higher than the yield strength in a part in which a notch is present and in the zone that has already been highlighted in the FEM analysis of the interference fit (paragraph 5.3.1.3). The result of the FEM analysis is shown in Figure 84; the deformed shape has been intentionally left, to highlight that such part is in a compression state.

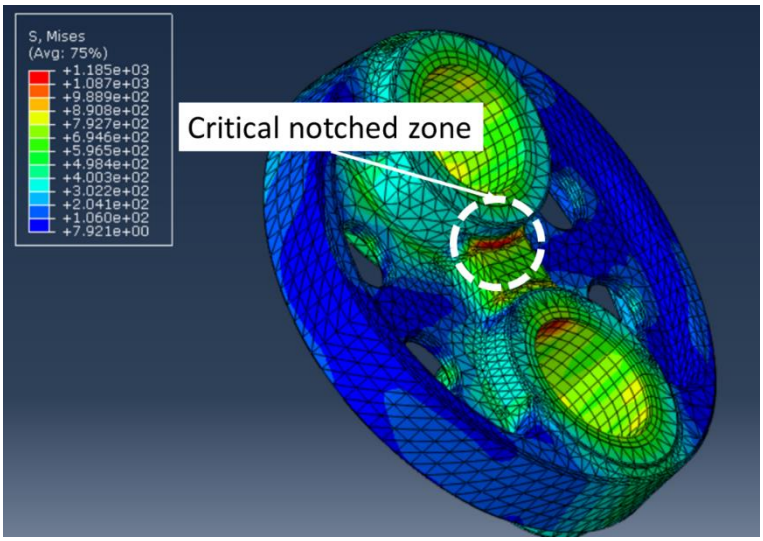

Figure 84 – Critical notched zone of the central part of the crankshaft for a crank angle of 374°

Since from the deformed shape in Figure 84 the critical zone seems to be in compression, that notched part has been analysed in terms of maximum and minimum principal stress. Their values are respectively reported in Figure 85 and in Figure 86, showing that the state of stress is compressive.

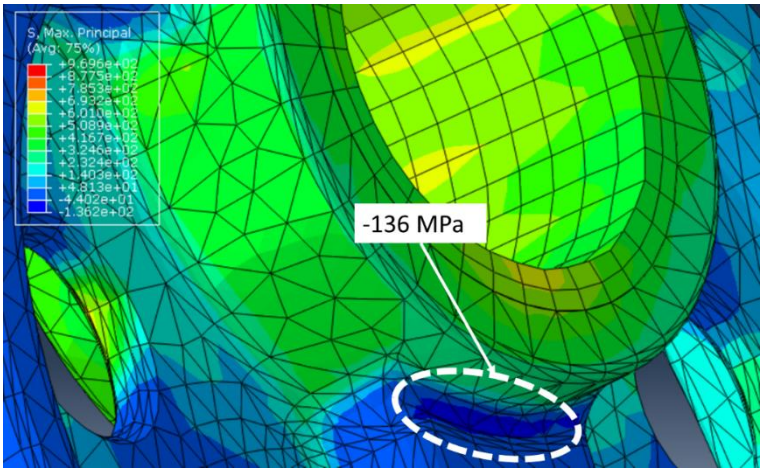

Figure 85 – Maximum principal stress concentrated in the notch of the central part of the crankshaft for a crank angle of 374°

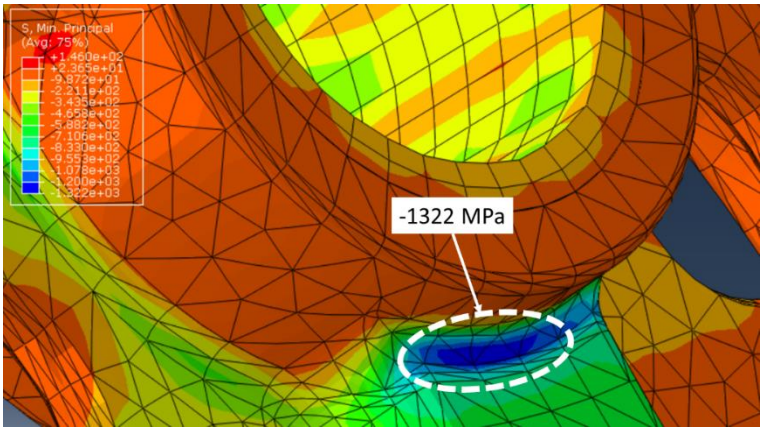

Figure 86 – Minimum principal stress concentrated in the notch of the central part of the crankshaft for a crank angle of 374°

Anyway, even if in general the compressive stress states are not dangerous for metals (steel in this case), it has been decided to change the fitting radius, passing from 2 mm to 9 mm. However, also after having done this change of the fillet radius, the Von Mises stress is higher than the yielding limit as shown in Figure 87.

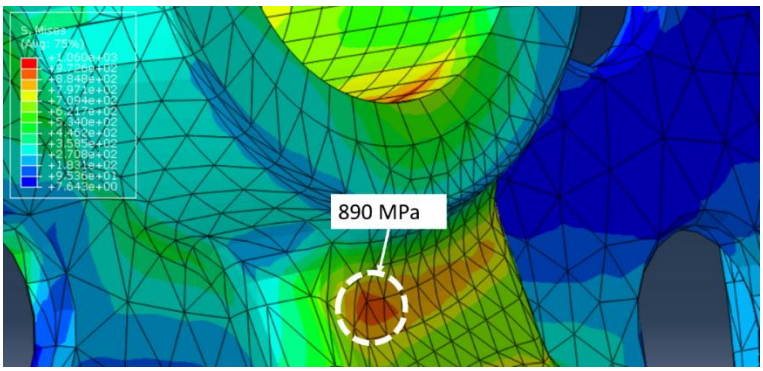

Figure 87 – Von Mises stress in the critical zone of the central part of the crankshaft, higher than the yielding limit even after the increasing of the fitting radius

No more changes have been done after this latter analysis, but a possible solution for reducing the Von Mises stress is to increase the moment of inertia of the section respect to the neutral axis; moreover it is important to underline that this concentrated yielding zone is not a problem for a static point of view (mainly because is a compressive stress state) but it will be a problem for the fatigue life, since in that zone there is a cyclic stress state.

5.3.3.3 FEM slipping analysis

The FEM slipping analysis has been performed by using the FE software Abaqus for evaluate the absence of slipping of the two interference fits that joint the crankshaft. If the two surfaces slip one on the other, the crankshaft can modify its geometry causing a malfunction and then a failure of the engine. If the slipping is present but in a very small amount, the fretting phenomenon can arise, that is a kind of fatigue wearing due to the relative motion among two surfaces in contact with friction.
This analysis has been done simulating the maximum torque condition, which is given by the crank angle equal to 25°. Moreover, the used interference among the pins and the holes of the internal part of the crankshaft is the minimum elastic one, that is equal to 68 μm.

The results, in terms of contact status (CSTATUS) that is an output variable of Abaqus which allows to evaluate the relative motion of the contact surfaces, are shown in Figure 88. The red colour means that the contact is closed and sticking, the green colour means that is closed but there can be slipping while the blue colour means that the contact is open. So, for being sure that there will not be slipping problem, all the contact surfaces area must be red.

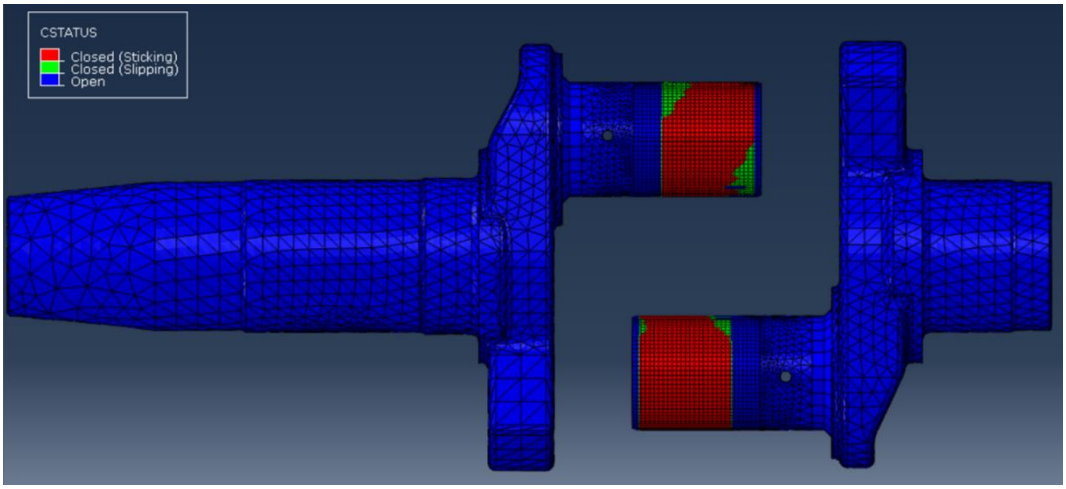

Figure 88 – Results of the FEM slipping analysis in terms of contact status (CSTATUS)

Unfortunately, the above picture shown that there is some green and even some blue in the contact surface areas. In Figure 89 a detailed view of the two contact surfaces is shown. From these results, it is possible to conclude that the crankshaft should not change its geometry even in case of minimum elastic interference, because there is a closed loop red surface around both the pins. Anyway, the possible issue can be given by the fretting, since there are more than one evident green areas, but only an experimental test can give the final outcome.

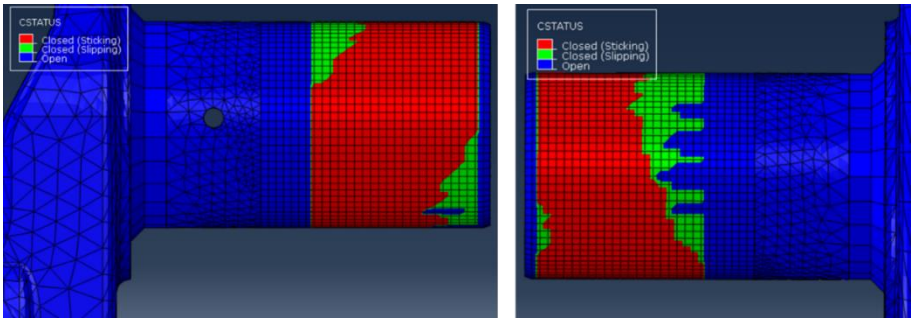

Figure 89 – Detailed view of the CSTATUS of the pin of the posterior crank (left) and of the pin of the anterior crank (right)

5.3.4 Modal analysis of the crankshaft

The modal analysis of the crankshaft is a very important assessment to be performed, for ensuring that the first six harmonics of the rotational speed (that causes a sinusoidal loading condition) do not excite any eigen-frequencies of the component. The analysis has been performed in Abaqus, on a 3D model of the crankshaft, in which the three components (anterior crank, posterior crank and central part of the crankshaft) have been merged together. The element used for the whole model are the C3D10 and the boundary conditions are the same as those used for all the other FEM assessment on the crankshaft. Of course, the step definition sees a linear perturbation procedure type for the extraction of the frequencies of the system.
The rotational speed of the shaft during its phase of operation is equal to 4000 rpm, and so all the harmonics are an integer multiple of such frequency. The first one is computed as follow:

$$f_1 = \frac{4000\ rpm}{60} = 66.67\ Hz$$

All the successive harmonics are computed in this way:

$$f_2 = 2f_1 \qquad f_3 = 3f_1 \ \ldots\ f_n = nf_1$$

The upper frequency limit for finding the vibrational modes has been set equal to 2500 Hz. The selected limit has allowed to find the first 5 eigen-frequencies of the crankshaft, whose value is reported in the following table (Table 27).

Table 27 – Eigen-frequencies of the first 5 vibrational modes of the crankshaft

1° mode	2° mode	3° mode	4° mode	5° mode
594 Hz	667 Hz	877 Hz	931 Hz	2137 Hz

The modal shapes of the crankshaft are shown in Table 28.

Table 28 – Modal shapes of the crankshaft

Modal shapes of the crankshaft	
1° mode	**2° mode**
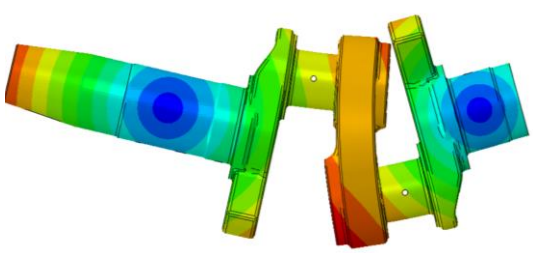	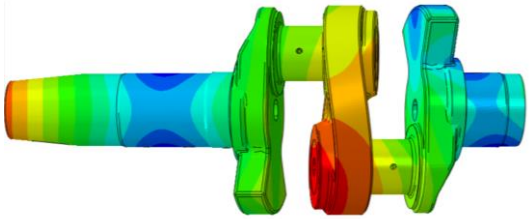
3° mode	**4° mode**
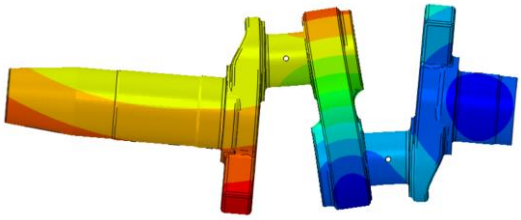	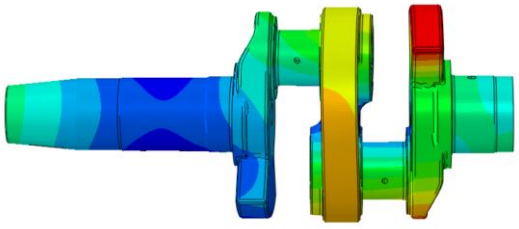

5° mode
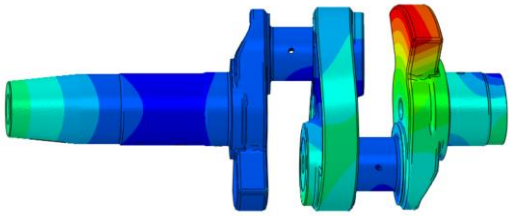

The results have been analysed using the Campbell diagram (Figure 90), which allows to graphically describe the interaction between the eigen-frequencies of the vibrational modes with the frequencies of the harmonics of the loads. In the Campbell diagram, the horizontal lines represent the eigen-frequencies of the vibrational modes, that in this case are the first 5. The straight lines that start from the origin and that have different slopes, are the harmonics as a function of the rotational speed of the engine. When one of the harmonics interact with an eigen-frequency the system may works in resonance condition, which is dangerous for the engine. Thanks to the Campbell diagram, this interaction can be easily detected as the points where the harmonics intersect the modes.
The red points in Figure 90 represents the interaction between the eighth harmonic (x8) and the first vibrational mode, that happens for a regime of about 4450 rpm. This condition is not dangerous for the crankshaft because the maximum rotational speed of the engine is 4000 rpm and because the harmonics higher than the sixth are not harmful. Indeed, on the left side of the red dashed vertical line that represents the maximum speed of 4000 rpm, no interaction exists.

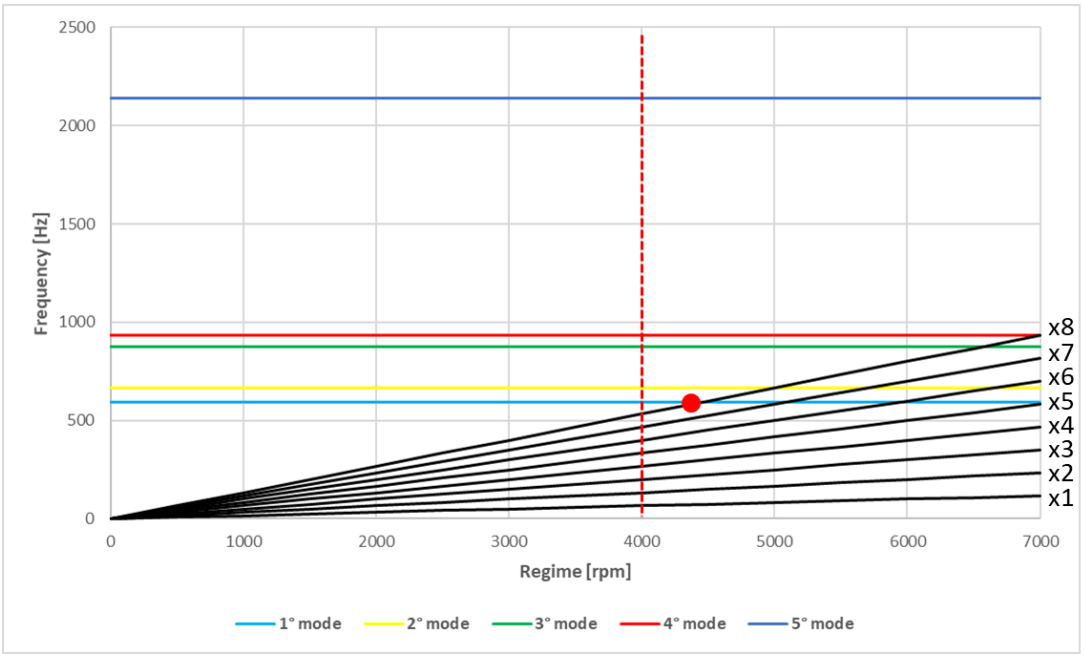

Figure 90 – Campbell diagram

5.4 Connecting rods design

The mechanical design activities of the connecting rods involve the static and fatigue assessments and a fretting analysis. All these analyses have been performed with Abaqus and the fatigue assessment also with MatLab.

5.4.1 FE model of the rod

In this paragraph, the implementation of the finite element model of the rod using the finite element software Abaqus will be explained. In particular, the principal features of the model are here explained, those that are common in all the FEM assessment in which the FE model of the rod is involved. The components involved in this model are of course the rod, and the pin that joints the piston and the rod together. The pin has been implemented for better simulating the reality. The layout of the connection that involves the rod, the pin and the piston is shown in Figure 91.

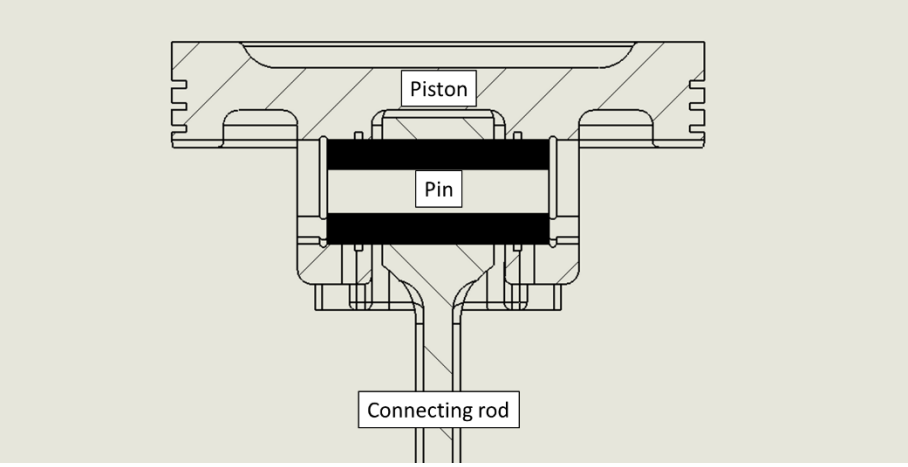

Figure 91 – Section view of the joint among the piston and the rod, thanks to the pin (black component)

The rod has been directly imported, as a part, in ".Step" format from the CAD software (SolidWorks) to the finite element software (Abaqus), while the pin has been created in Abaqus as a 3D analytical rigid revolved shell. In Figure 92 the two components involved in the present FE model are shown.

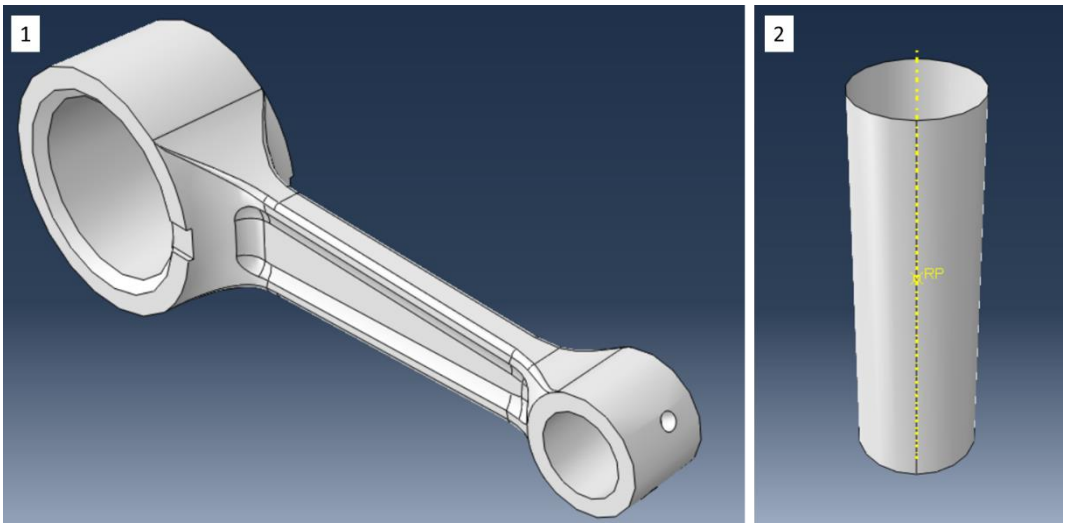

Figure 92 – Imported rod (1) and drawn pin (2) used in the FE model of the connecting rod

In the property module of Abaqus, the elastic properties of the material of which the connecting rod is composed have been set. In particular, the needed parameters are the Young modulus and the Poisson's ration, and since the rods are made of steel, their values have been set for simulating such material. In Table 29 the used values for the elastic parameter of the material are reported.

Table 29 – Material properties of the connecting rod

Material properties of the connecting rod			
Parameter	**Variable name**	**Value**	**Unit**
Young modulus	E	207000	MPa
Poisson's ratio	v	0.3	-

The material of the pin has not been defined since it is an analytical rigid part, and it does not require any specification.
After the definition of the material properties and the assignation of the section, it has been necessary to assemble the connecting rod and the pin. The pin is inserted into the hole of the foot of the rod. In Figure 93 the assembled model of the connecting rod with the pin is illustrated.

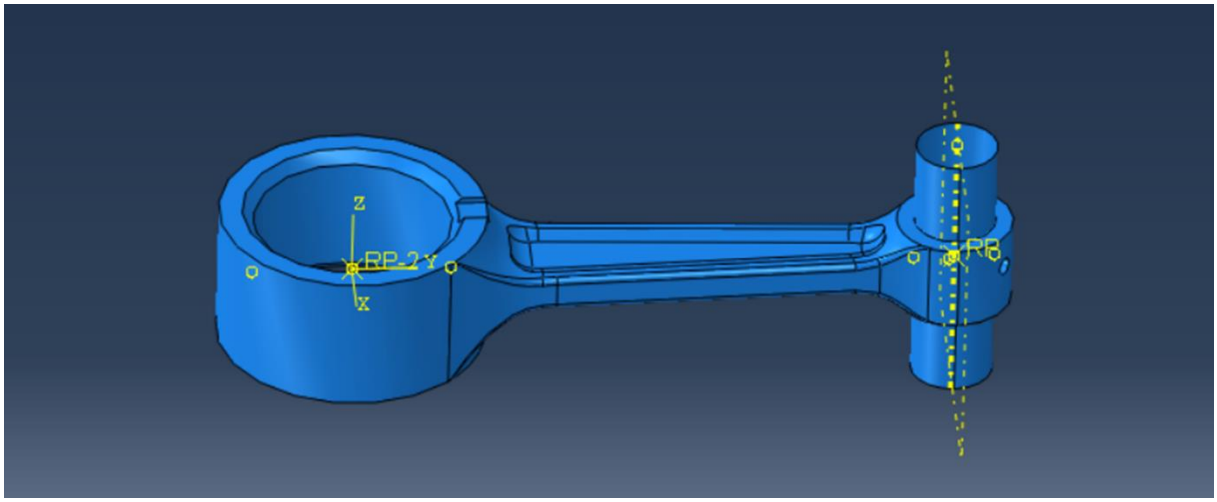

Figure 93 – Assembled model of the connecting rod and the pin

Then, four static general steps have been defined, the first one for the definition of the contact among the pin and the foot of the rod and the other three for the definition of the loads in different conditions. Other specification regarding the steps will be reported in the chapters that concern the assessments on the connecting rod.
In the interaction module, the contact among the pin and the foot of the rod has been implemented, as well as some coupling constraints for distributing the boundary conditions or the loads.
The interaction among the pin and the rod has been defined as a surface to surface contact in the step used for that purpose. The surfaces involved are the external one of the pin, set as master surface, and the internal one of the foot of the rod, set as slave surface. The only property defined for this interaction is the frictionless tangential behaviour. The surfaces involved in the interaction and the property are shown in Figure 94.

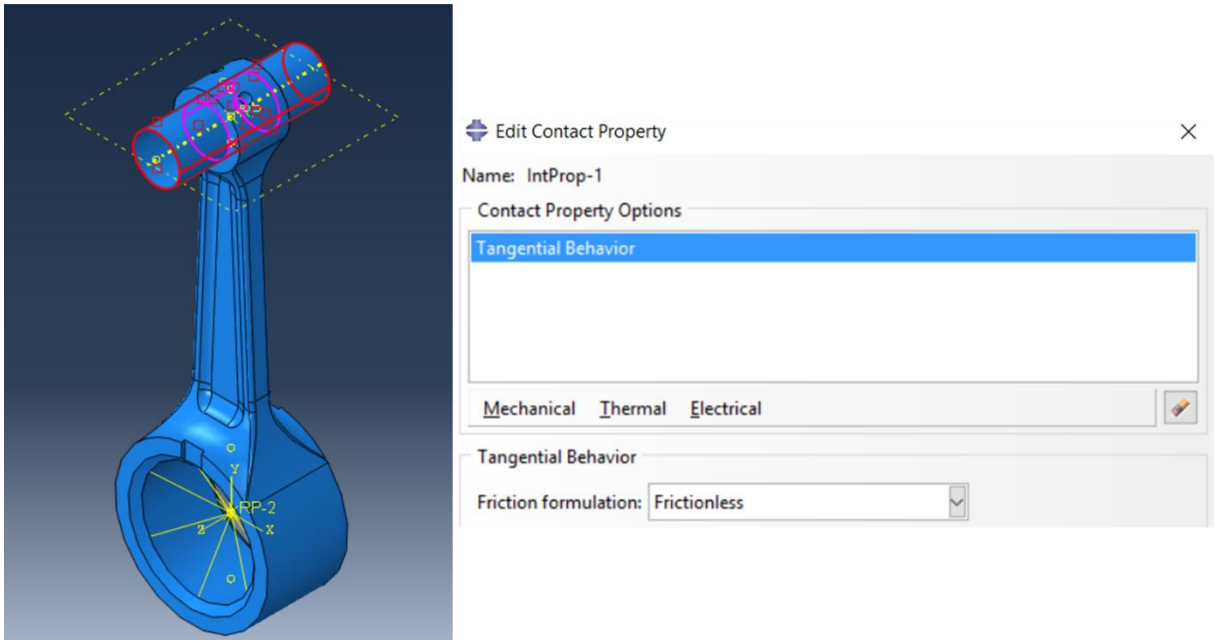

Figure 94 – Interaction defined without friction among the pin and the connecting rod

Then, for distributing the boundary conditions of the connecting rod, two couplings have been implemented for simulating the bushing bearing applied to the head of the rod and the pin applied to the foot of the rod (despite the pin is already present in the FE model). For defining the couplings, two reference points have been put in the middle of the head and of the foot of the rod, and then they have been coupled with the related surface. The type of both these coupling is the kinematic one, with all the degree of freedom constrained. In Figure 95 the position of the reference points and their related surfaces are shown. In particular, RP-1 is the reference point that controls the foot of the rod and RP-2 is the reference point that controls the head of the rod.

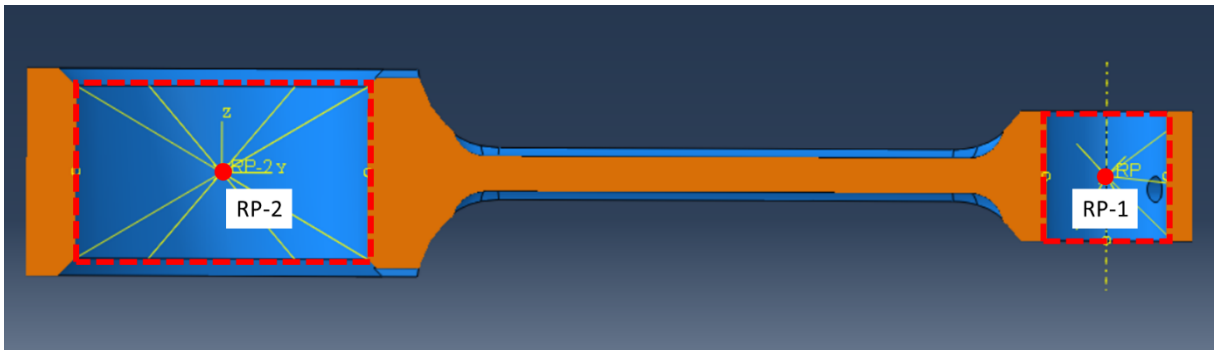

Figure 95 – Section view of the connecting rod in Abaqus, with the two reference points (red dots) and their related surfaces (red dashed lines)

For the pin, a reference point positioned in the middle has been defined in the part definition, and then constrained with a rigid body constraint to its external surface. The purpose of this latter constraint is to apply the force and boundary conditions application to this component. The region type selected, as illustrated in Figure 96, is analytical surface.

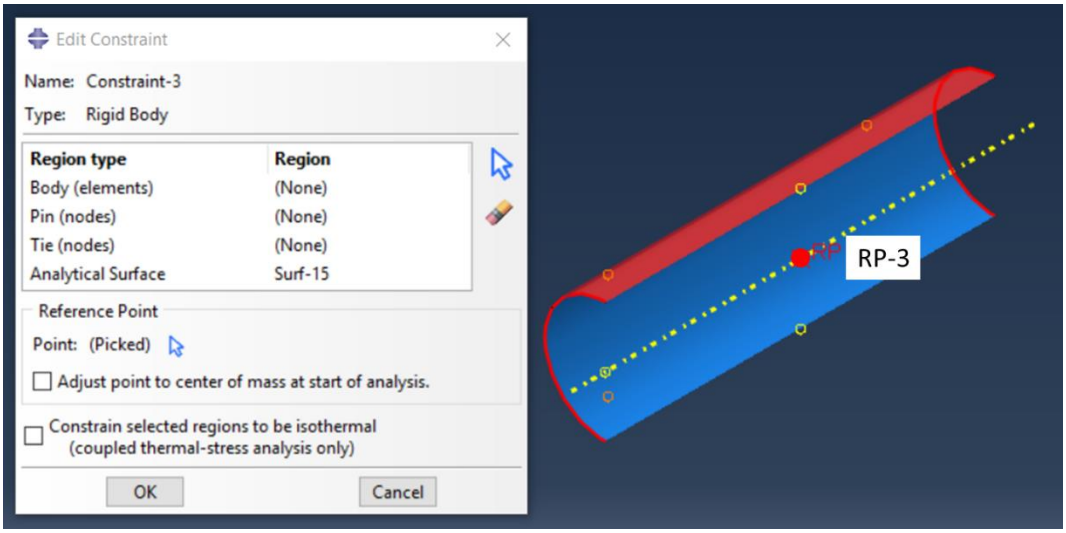

Figure 96 – Section view of the pin in Abaqus, with the reference point (red dot) and their related surface (red surface)

After the interactions definition, in the load module all the boundary conditions and the forces have been implemented. The boundary conditions of the rod simulate a roller in the foot and a hinge in the head. They have been respectively applied to the reference point 1 (RP-1) and to the reference point 2 (RP-2). In RP-1, the constrained degrees of freedom are the two directions transversal to the rod's axis (U1 in x direction and U3 in z direction), while in the RP-2 all the 3 main directions have been constrained (U1, U2, U3). The degrees of freedom constrained in Abaqus are shown in Figure 97.

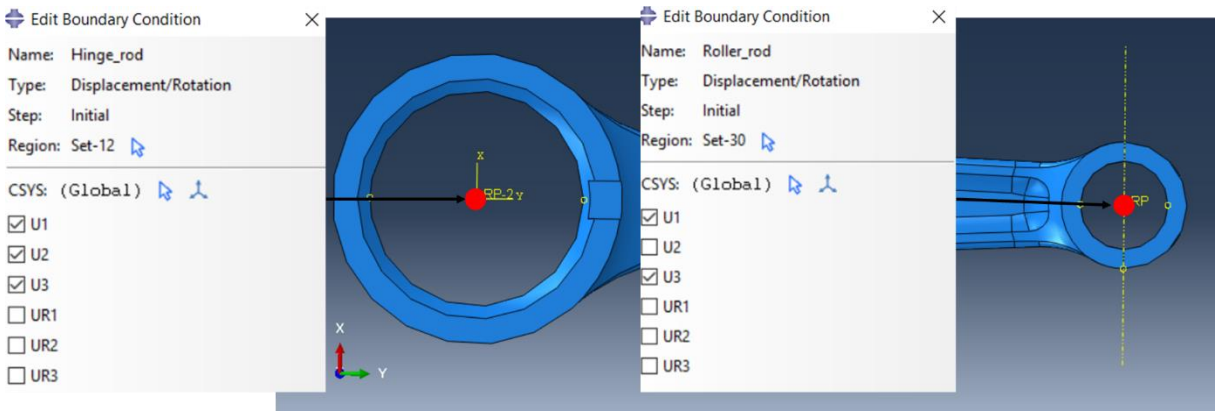

Figure 97 – Boundary conditions applied on the rod; on the left the hinge with U1, U2, U3 constrained and on the right the roller with U1 and U3 constrained

Also the pin needs some boundary conditions in RP-3 and in particular all the degrees of freedom, both linear and rotational, have been constrained except the linear one directed with the axis of the rod. Indeed, that degree of freedom is those that allows to evaluate the stress in the rod, since it is stretched and compressed only in that direction. In Figure 98 the boundary conditions applied on the pin in Abaqus are illustrated.

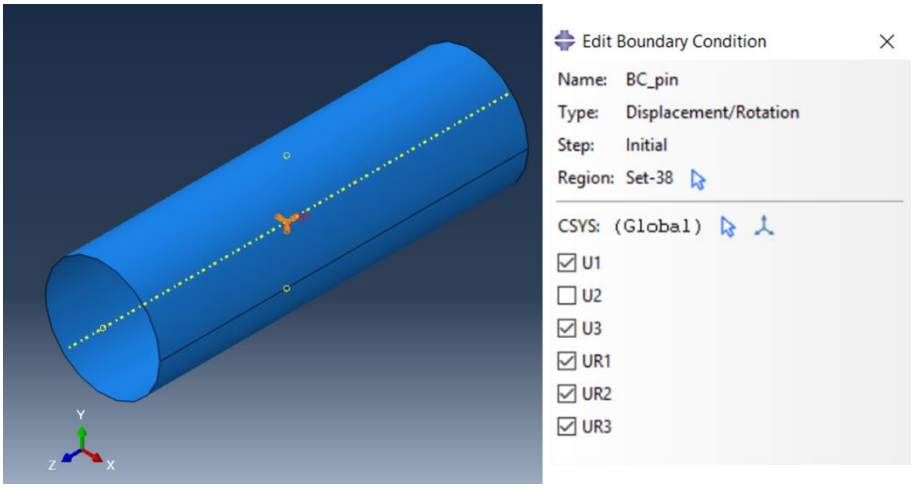

Figure 98 – Boundary conditions applied on the pin

The force F has been applied on RP-3, thus on the pin, in the direction of the free degree of freedom (U2 that is directed with the axis of the rod). Its value and direction depends on the condition to simulate. The load cases and the assessment for which they have been used are reported in Table 30.

Table 30 – Load cases and assessments for which they have been used

Load case	Static assessment	Fatigue assessment	Fretting assessment
Max compression at starting	✓	✗	✗
Max compression @ 4000 rpm	✗	✓	✗
Maximum traction @ 4000 rpm	✗	✓	✓

For each one of these cases, the force F assumes a different value and direction. In Table 31 the values of the force F are reported for the different load cases. The positive sign means traction, while the negative sign means compression, from the rod point of view.

Table 31 – Values of the loads used in the different load cases

Load case	F [N]
Maximum compression at starting	-29815
Maximum compression at 4000 rpm	-26608
Maximum traction at 4000 rpm	3388

In Figure 99 a section view of the complete FE model with all the boundary conditions and the load applied in the case of maximum compression at starting is shown.

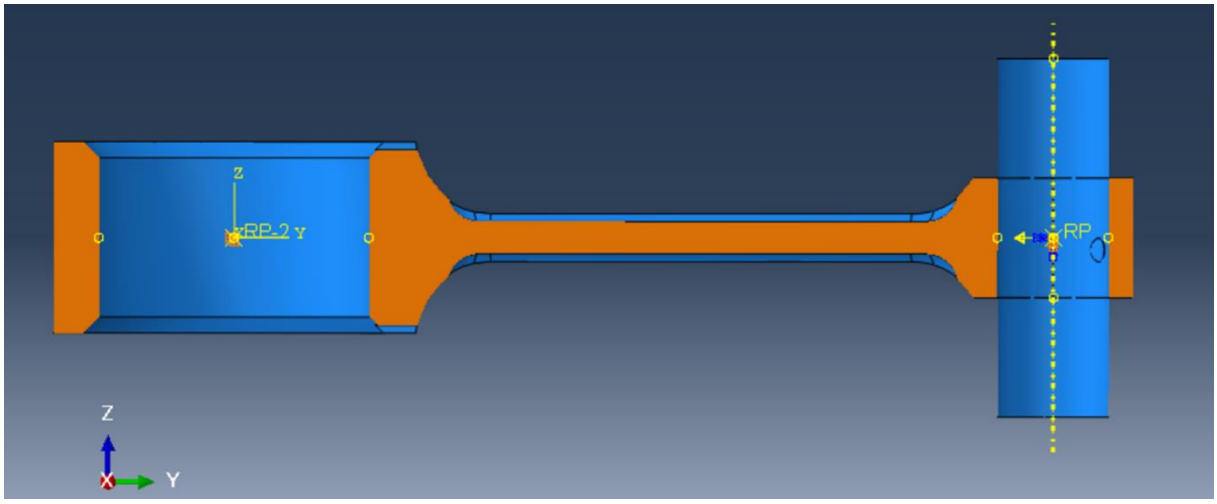

Figure 99 – Section view of the FE model with the boundary conditions and the load applied in the maximum compression at starting case

The final step of the FE model implementation procedure is the elements type and mesh definitions. These two things do not concern the pin, because it has been defined as analytical rigid and it does not require any mesh as well as any material. Regarding the rod, the elements type used for the whole part is C3D10 (A 10-node quadratic tetrahedron), due to its complex geometry that makes difficult to create cells that are adapt to the structured elements. Anyway, the mesh grid has been made very fine in the zones of interest, that are located just under the foot of the rod, where the section changes the geometry (Figure 100).

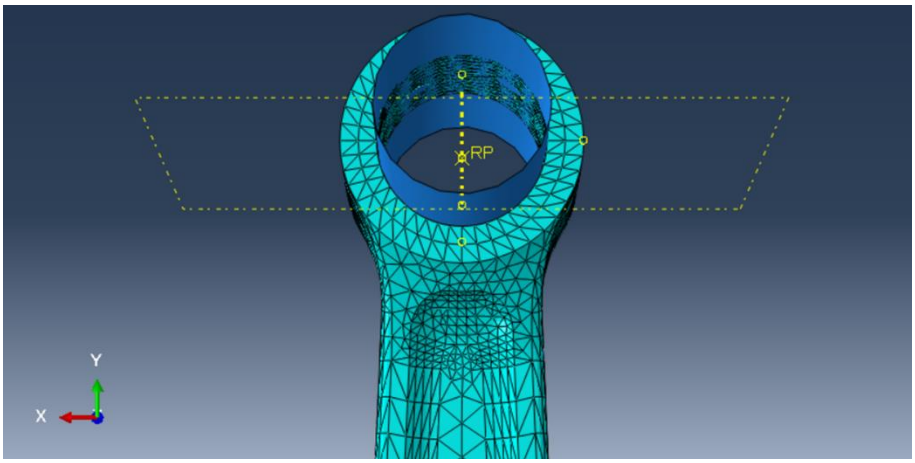

Figure 100 – Zoom on the fine mesh of the zone of interest

All the procedure described up to know has been developed iteratively, starting from easy and simple analysis that have been refined during the assessments.

5.4.2 FEM static strength assessment

The FEM static strength assessment on the rod has been performed simulating the starting condition, in which the rod is subjected to the maximum compression due only to the pressure in the combustion chamber. This case is the most critical because it does not take into consideration the inertia force acting on the rod, that reduce its load. In Figure 101 the trend of the force generated by the pressure in the combustion chamber, that acts on the piston, as a function of the crank angle is shown.

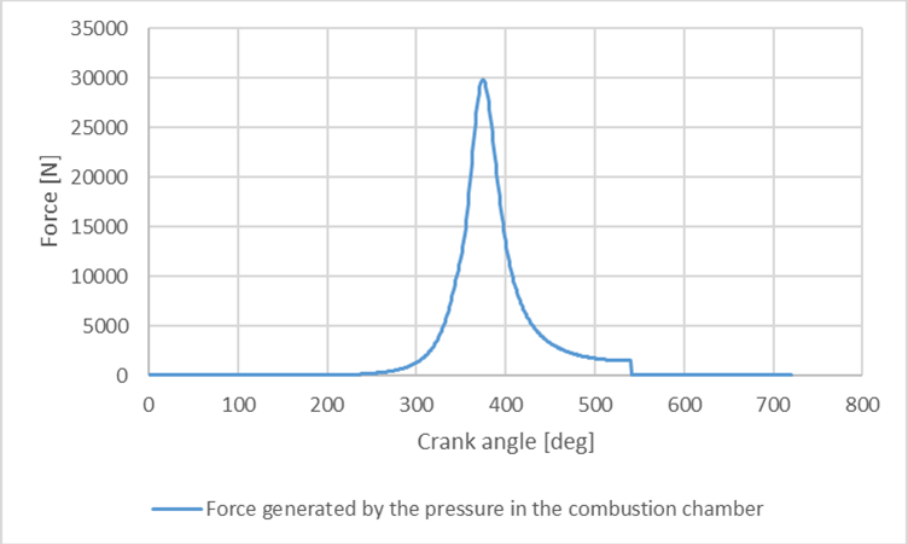

Figure 101 – Force generated by the pressure in the combustion chamber as a function of the crank angle

For the present assessment, the peak value of the force present in the above graph has been applied to the foot of the rod. The peak value is $F = 29815\ N$.
The results of the FEM analysis performed in this load condition, are reported in Figure 102, in terms of Von Mises stress.

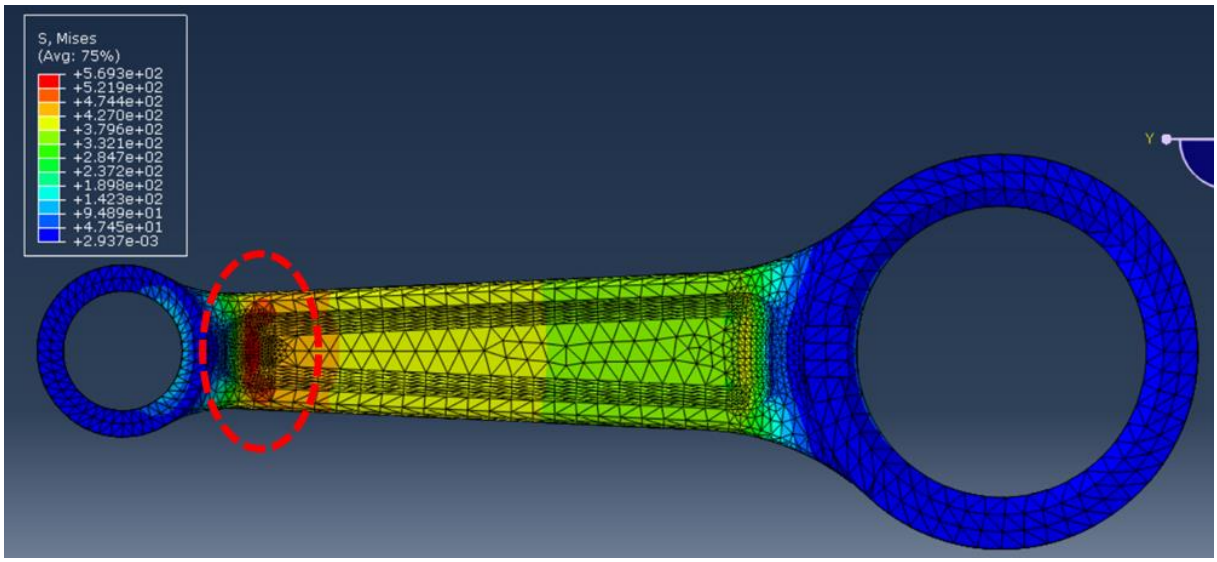

Figure 102 – Von Mises stress results of the FEM analysis performed on the rod in the maximum compression case

The red dashed line of the above figure indicates the most critical zone, for which the Von Mises stress has been extracted thanks to a path.

The value of the Von Mises stress extracted from the path shown in Figure 103, is lower than the yield strength, hence the rod is statically safe. Its trend is reported in Figure 104.

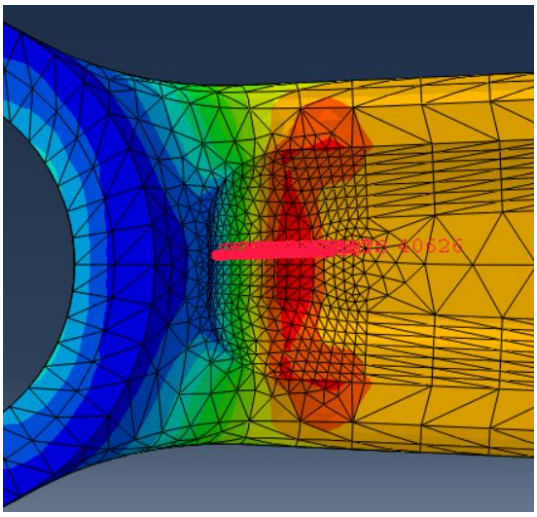

Figure 103 – Path used for the extraction of the Von Mises stress in the most critical zone of the rod

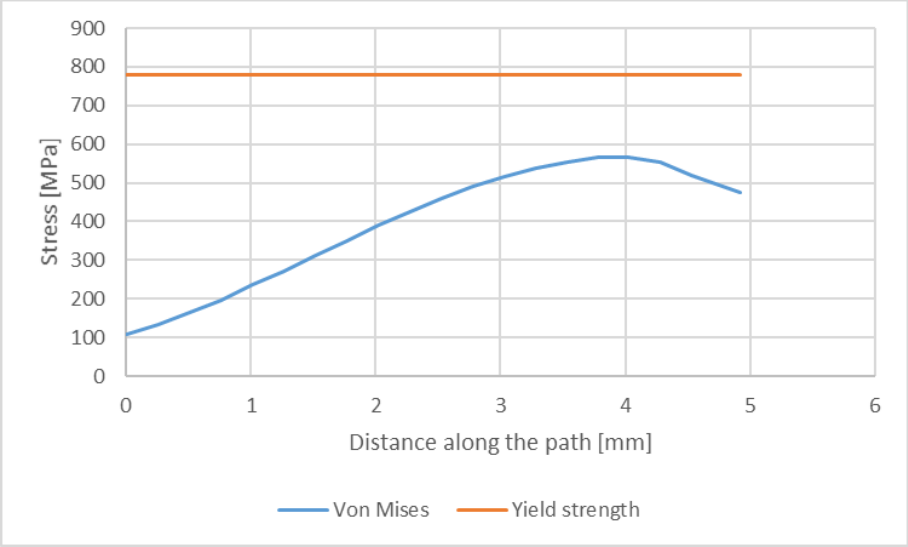

Figure 104 – Trend of the Von Mises stress versus the yield strength along the path

The maximum value of the equivalent Von Mises stress and the safety factor are reported below, remembering that the yield strength σ_y of the rod is 780 MPa.

$$\sigma_{VM,MAX} = 567\ MPa \qquad \eta = \frac{\sigma_y}{\sigma_{VM,MAX}} = 1.37$$

It is possible to conclude that the rod will not fail from a static point of view.

5.4.3 Fretting assessment

The fretting phenomenon is a kind of fatigue wearing due to the alternating tangential loads that are transferred by means of a contact among two surfaces. Such cyclic loads can cause local slipping, that during the time enhance the nucleation of fatigue cracks. The fretting phenomenon is very complex and involves both physicals (friction, wearing, adhesion, etc.) phenomena and chemicals reaction that happen in the interface zone.
Due to the complexity of the fretting fatigue, the attempts for the definition of a criterion for the assessment have been a lot, most of them with contradictory results. However, all the attempts have given a common output: the surfaces that undergo to fretting are subjected to an high multiaxial stress gradient.
Some of the principal criteria for the fretting assessment are [21]:

- Funk criterion
- Ruiz criterion
- Ziaei criterion (modified Ruiz criterion)

In this case, the involved surfaces are the internal one of the rod head and the external one of the bushing bearing of the rod head. This latter is forced in the hole of the rod's head for being rigidly constraint to the rod's head (Figure 105). The interference fit among the bushing and the rod is not aimed at transmitting a tangential stress, so the fretting fatigue should not be present. Anyway, it could happen that when the connecting rod undergoes to traction, the two surfaces in contact locally detach, causing after a certain number of cycle the nucleation of cracks and so the fretting fatigue.

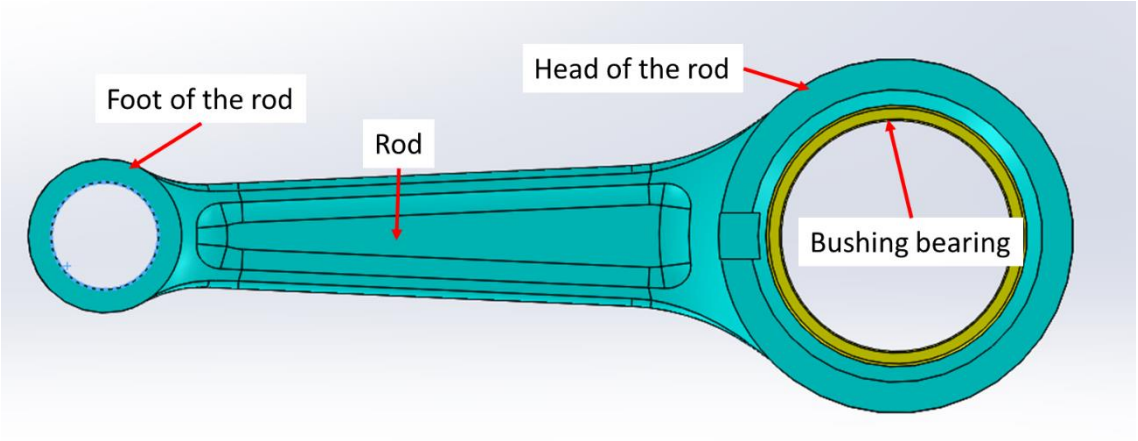

Figure 105 – Layout of the rod with the bushing bearing coupled with the head of the rod

The assessment has been performed by applying the maximum traction load to the foot of the rod in the maximum constant rotational speed condition, that is equal to 3388 N. The bushing bearing (Figure 106) has been modelled in the FE software Abaqus, in order to give to him an external diameter that guarantees the needed minimum interference that should be at least of 20 μm.

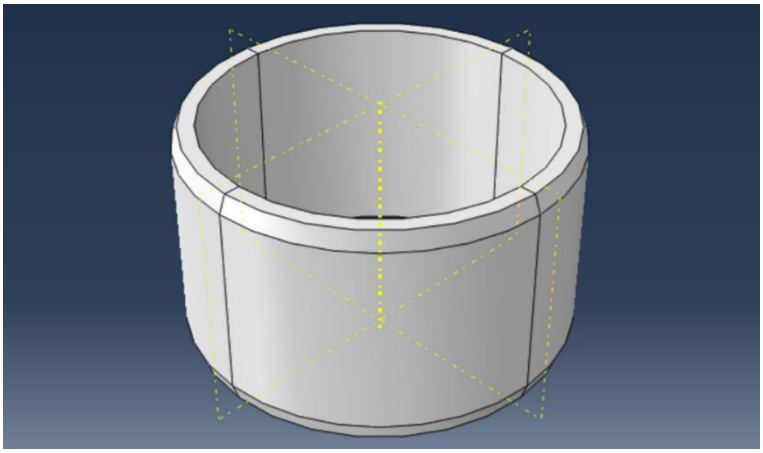

Figure 106 – Model of the bushing bearing created in Abaqus

The FE model of the rod is the same used for the other assessment, but in this case, it is necessary to define the interference among the bushing bearing and the head of the rod. Since the contact surfaces are both made of steel, (the bushing bearing has a thin external steel layer) the friction coefficient used in the interaction property is equal to 0.2. Another difference is in the boundary condition implementation, because the hinge here is positioned in the internal surface of the bushing bearing instead of the internal surface of the head of the rod. This change allows the internal surface of the head to deform and even to separate from the other surface of the coupling. If this condition happens, the coupling can undergo to the fretting phenomenon.

The elements of which the model of the bushing is made of are C3D10 (A 10-node quadratic tetrahedron).

The bushing bearings are not definitely chosen, but their material composition is known and shown in Figure 107. Since the 80% of its composition is represent by the Cu8Sn4Bi alloy (bronze), the elastic properties used for the FEM analysis are those of such material and they are reported in Table 32.

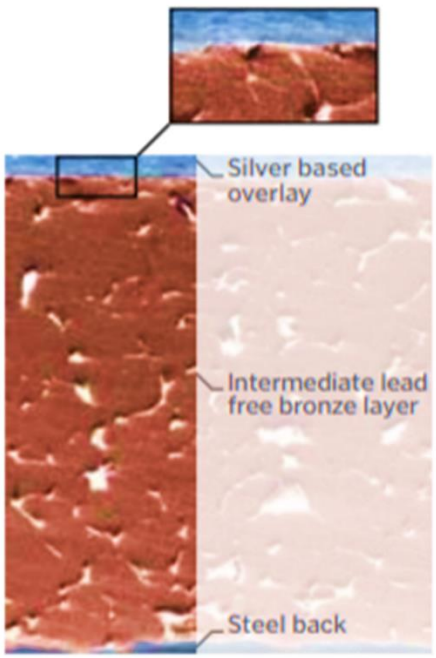

Figure 107 - Section of the reference bushing bearing made of K-796 and produced by KING (source: http://www.kingbearings.com/catalog/)

Table 32 – Elastic properties of the bushing bearing used for the FEM analysis

Property	Variable name	Value	Unit
Young's modulus	E	96000	MPa
Poisson's ratio	v	0.34	-

The results of the FEM assessment have been analysed in terms of contact status (CSTATUS), an output variable of Abaqus that allows to evaluate if the surfaces are in contact without slippage, in contact with slippage and if they are separated. These two latter conditions are the critical from a fretting point of view, since the relative motion of the two surfaces generates this kind of fatigue wearing.
In Figure 108 the results of the fretting analysis are shown for the external surface of the bushing bearing. The colour red means that the contact is closed and sticking, the colour green means that it is closed but there can be slippage and the blue colour means that it is open. Since all the contact surface is red, a perfect contact without slipping should be guaranteed.

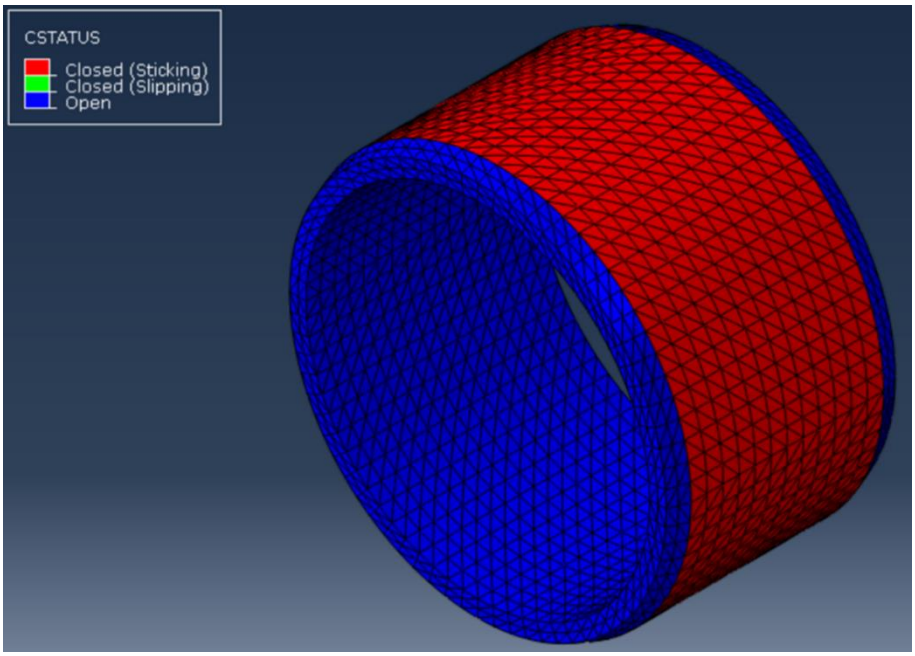

Figure 108 – Results of the FEM fretting analysis in terms of contact status (CSTATUS)

5.5 Electric generator design

The electric generator (Figure 109) is the component which transform the mechanical energy provided by the engine into electric energy for charging the batteries. It is composed by two main components, the rotor and the stator. The configuration is the external rotor one.

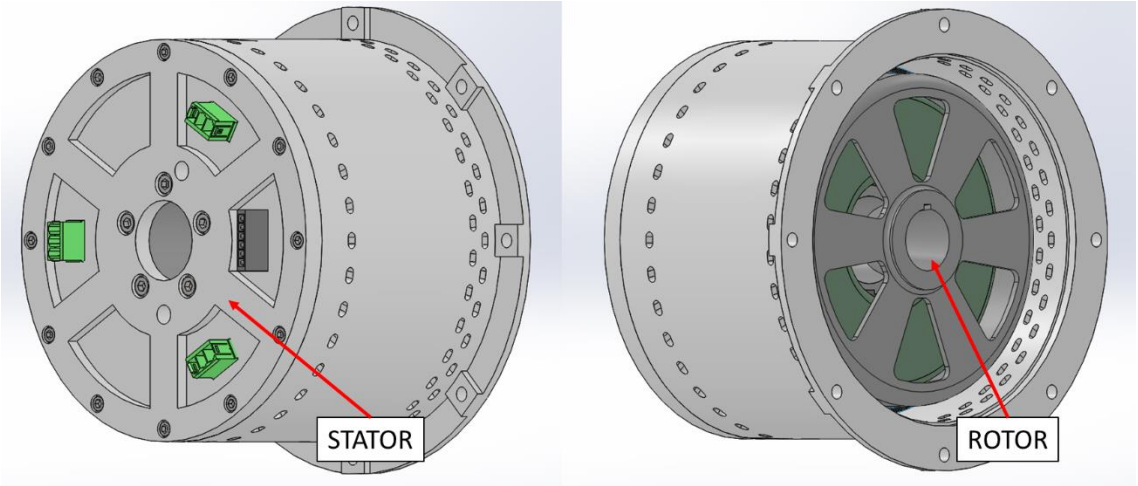

Figure 109 – Electric generator

The rotor is subjected to the torque coming from the output shaft of the internal combustion engine, while the stator is subjected to a reaction torque equal and opposite to that given by the rotor. The stator receives the torque thanks to the magnetic reaction force that is downloaded on the magnets from the windings. Moreover, the idea is to use the electric generator also as starter, and in this case, it is subjected to a torque that is about the 300% of the nominal torque of the engine at the constant rotational speed of 4000 rpm. The starting torque value, that has been set as design hypothesis, is of 100 Nm and since the structure of the stator is made of aluminium alloy 6060, some assessment has been done on the stator of the electric generator. The problem concerns the bolted joint among two of the components of the stator, which is subjected to the reaction torque of 100 Nm. This joint connects the magnets carrier, on which the torque is downloaded, to the cover plate (Figure 110). It is realized with five M8 screws, radially disposed at 35 mm from the axis of magnets carrier, that are preloaded to keep constrained the two components without slipping. The components that take part to the assessments on the stator are reported in Figure 111.

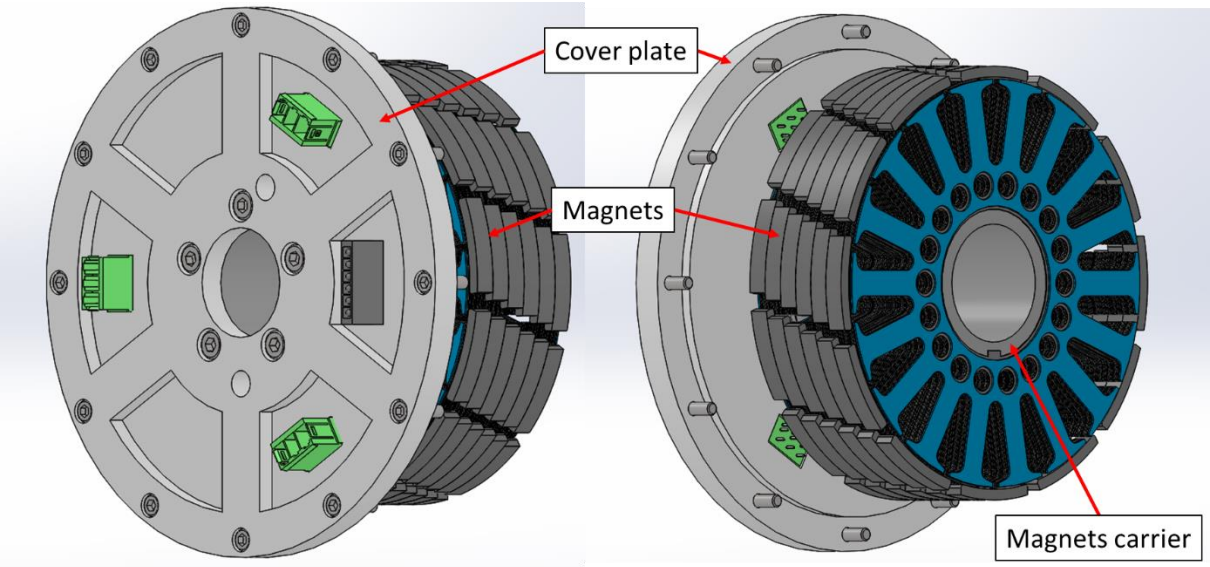

Figure 110 – Stator of the electric generator with the critical components

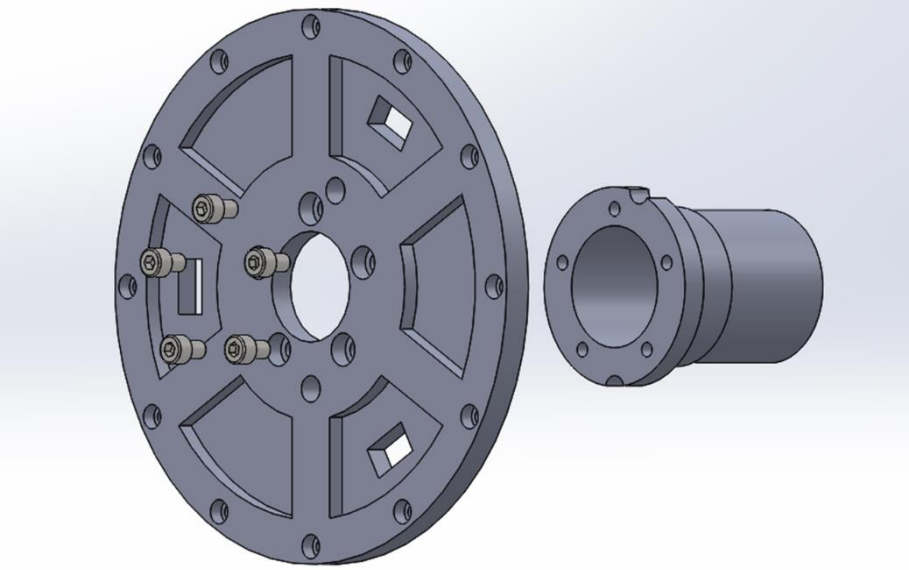

Figure 111 – Components that take part to the assessment on the stator

Since the screws are disposed with a relative low radius, the force that is downloaded on each one can be harmful for the aluminium holes, and it has been decided to assess the joint, both for evaluating the stress along the wall of the holes (Hole plastic deformation) and for evaluating the presence of relative slipping among the two components.

5.5.1 FE model of the stator

A FE model of the components of the stator involved in the assessments has been developed. The cover plate and the magnets carrier have been imported from the CAD software (SolidWorks) in ".Step" format, while the screws has been drawn directly in the FE software Abaqus. The three components are illustrated in Figure 112.

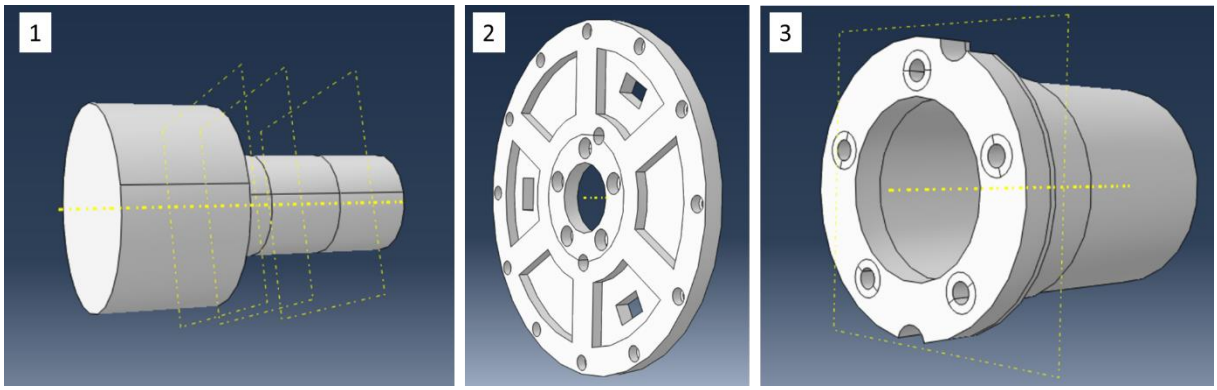

Figure 112 – Components used for the assessments in Abaqus; the screw (1), the cover plate (2) and the magnets carrier (3)

The involved materials are the steel, for the screws, and the aluminium alloy 6060 for the cover plate and the magnets carrier. Since one of the target of the assessments was to evaluate the plastic deformation of the holes, if present, also the yielding strength of the aluminium alloy 6060 has been defined in the plastic properties of such material. Anyway, only the region around the holes of the magnets carrier has been modelled with an elastic-plastic material. The elastic and plastic parameters of these materials, implemented in Abaqus are reported in Table 33.

Table 33 – Properties of the materials used for the FE model of the stator

Aluminium alloy 6060			
Parameter	**Variable name**	**Value**	**Unit**
Young modulus	E	69000	MPa
Poisson's ratio	v	0.33	-
Yielding strength	σ_y	60	MPa
Steel			
Parameter	**Variable name**	**Value**	**Unit**
Young modulus	E	207000	MPa
Poisson's ratio	v	0.3	-

After the material definition, the three components have been assembled (Figure 113), and then three steps have been created. The first step is used for applying the bolt loads on each screw, simulating the preloads, the second step is used for fixing the length of the screws, in order to maintain the preloads, and the third step is used for applying the torque to the magnets carrier. This procedure allows to simulate the real situation and to perform a complete and accurate analysis.

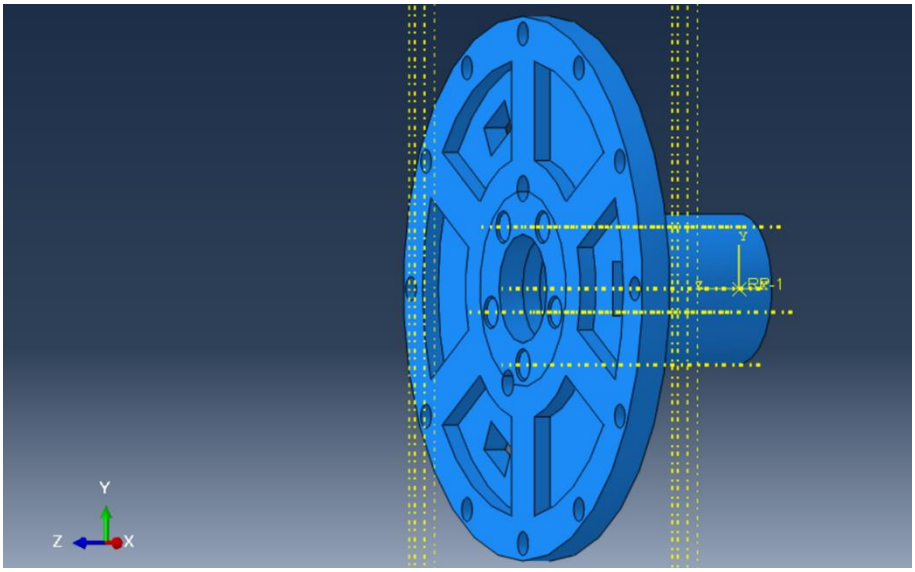

Figure 113 – Assembled model of the stator implemented in Abaqus

In the interaction module, all the contacts among the surfaces and a coupling constraint have been defined. The contacts are between the cover plate and the magnets carrier and between the screws and both the two other components; indeed, the head of the screws is in contact with the cover plate, while the threaded shanks are in contact with the threaded holes of the magnets carrier. To be noted that the thread has not been modelled, since it was not requested to analyse it. The coupling constraint, that is of kinematic type, has been created among a reference point that lies on the axis of the magnets carrier and the internal surface of this latter. The reference point is used for applying the torque and the boundary conditions of the magnets carrier.
In the load section, the loads and the boundary conditions have been implemented. All the boundary conditions have been created in the initial step, while the loads have been created in the related steps. The cover plate, is constrained to engine by means of a bolted joint that has been modelled as a rigid encastre located on the perimetric surface. None load is directly applied on the cover plate. On the magnets carrier, an hinge boundary condition has been applied in the reference point cinematically coupled with the internal surface of the component. Moreover, the torque of 100 Nm is applied on the same reference point, but it has been created in the last step, after the preloading and length fixing of the screws. Also on the screws, the boundary conditions have been applied, in particular the linear degree of freedom along their axis and the rotational degree of freedom around the two transversal (transversal to the longitudinal axis of the screws) directions have been constrained. The boundary conditions on the screws are applied on the bottom surface of the shank. Then, a bolt load has been applied on each screw in the first step after the initial one, applying it on the transversal surface in the middle of the threaded shank. Such load is then modified in the step, by fixing the length of the screws and removing the force applied in the first step. This procedure creates the condition for the application of the torque in the last step. In Figure 114 location of the boundary conditions and the load applied on the screw is shown.

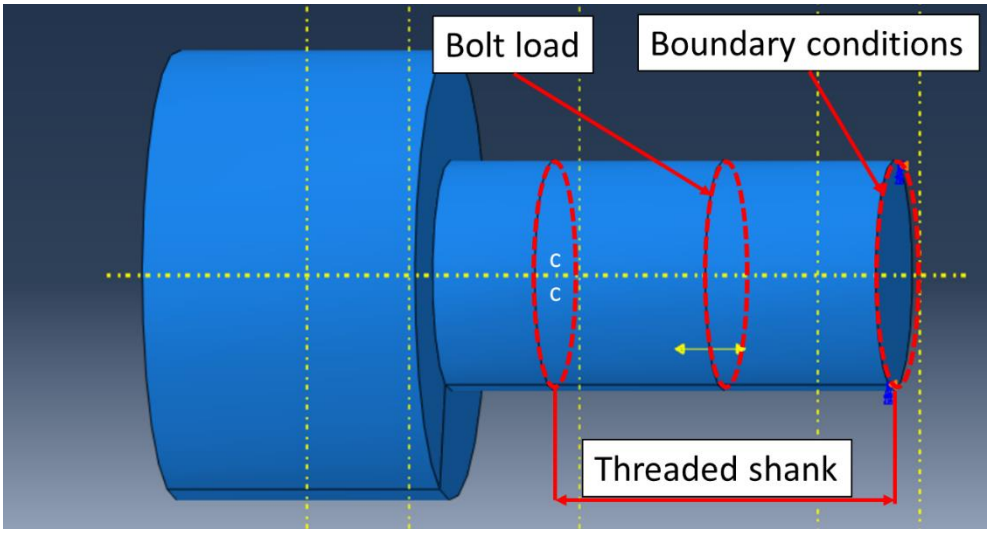

Figure 114 – Boundary conditions and bolt load position in the screw modelled in Abaqus

The M8 screws hypnotized for the analysis belong to the class 6.6 and according to the standard UNI 4535-64 have the following characteristics (Table 34).

Table 34 – Parameters of the M8 screws class 6.6 according to the standard UNI 4535-64

M8 screws class 6.6 according to UNI 4535-64			
Parameter	**Variable name**	**Value**	**Unit**
Nominal diameter	d_n	8	mm
Tensile area	A_{res}	36.6	mm^2
Ultimate tensile strength	UTS	600	MPa
Yielding strength	σ_y	360	MPa
Admissible stress	σ_{adm}	240	MPa

According to the data of the screws used for the joint, the limit preload has been calculated in the following way:

$$F_{preload} = \sigma_{adm} \cdot A_{res} = 8784\ N$$

None safety factor is needed because it is already embedded in the admissible stress value.
Then, in the mesh module, the mesh has been implemented and the type of elements have been selected for the different zones of the components. As usual, for the areas under investigation, the elements selected are the C3D20R (A 20-node quadratic brick, reduced integration), while for all the remaining zones the C3D10 (A 10-node quadratic tetrahedron). In Figure 115 the elements used for the screws (1), the cover plate (2) and the magnets carrier (3) are shown; in particular, the green and yellow areas indicate the presence of C3D20R elements, while the pink areas indicate the C3D10 elements.

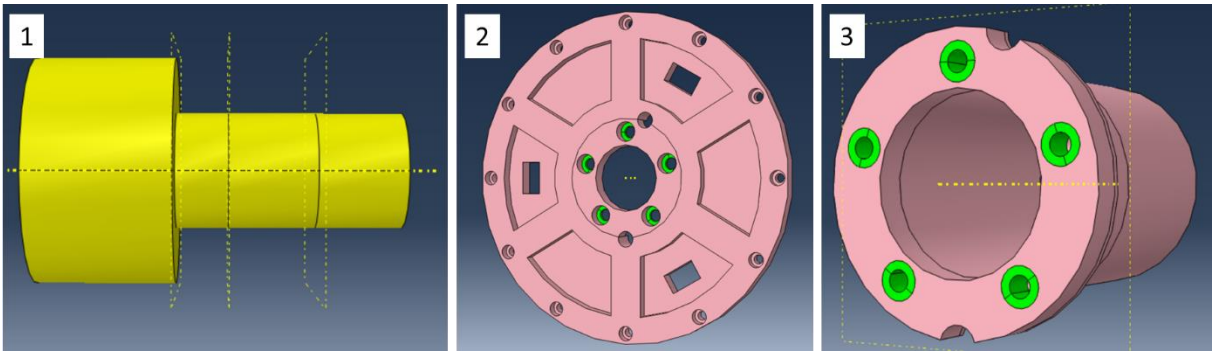

Figure 115 – Elements type used for the different components; the green and yellow areas indicate the C3D20R elements, while the pink areas indicate the C3D10 elements

Moreover, the mesh grid dimension has been made smaller for the critical areas, such as the region around the holes of the magnets carrier, which has the elastic-plastic material properties assigned, and in general the whole contact surface among the cover plate and the magnets carrier. The complete meshed model is reported in Figure 116.

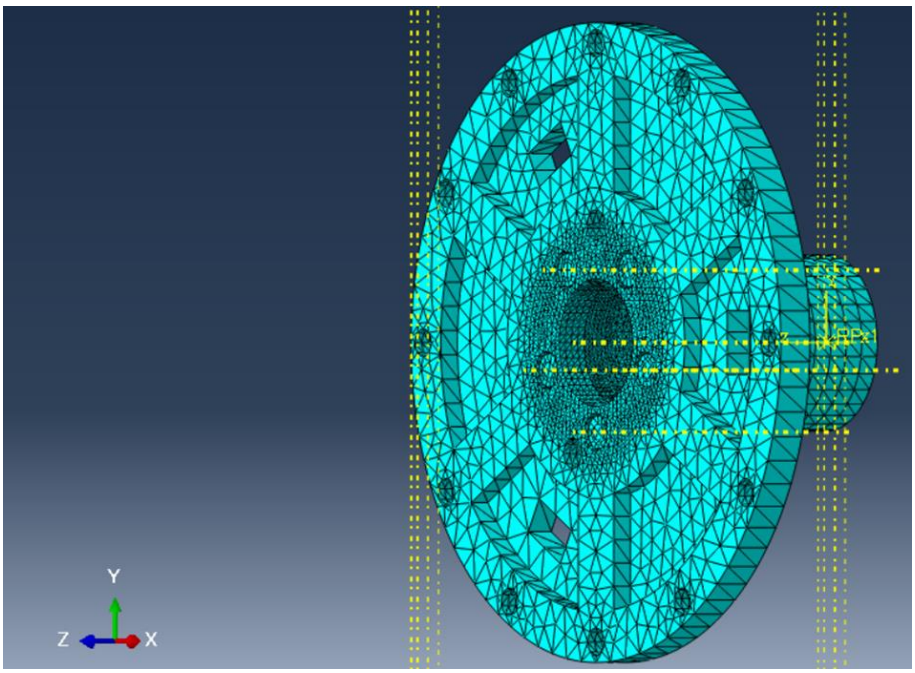

Figure 116 – Meshed model of the stator

The assessments performed on the components of the stator are two:

- Plastic analysis on the wall of the holes of the magnets carrier
- Slipping analysis of the friction joint

5.5.2 FEM plastic analysis on the holes of the stator

This analysis has been performed using the FE model implemented in Abaqus and the results of interest is the equivalent plastic strain (PEEQ) of the holes of the magnets carrier, those which are in contact with the screws. The problem arose because the aluminium alloy 6060 of which the magnets carrier is made of, is less stiff than the screws and this can cause a plasticization of the holes. So, the region around the holes has been modelled as elastic-plastic.
The results of the FEM analysis demonstrate that there is not any plasticization around the holes, as shown in Figure 117.

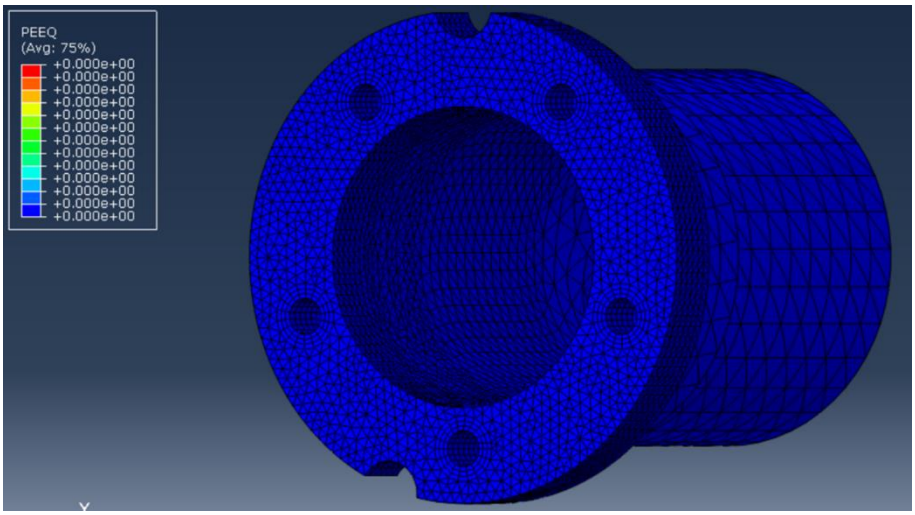

Figure 117 – Results in terms of PEEQ of the plastic analysis performed on the stator

From an analytic point of view, with a torque T of 100 Nm and knowing that the distance r at which the centres of the holes are located respect to the axis of the magnets carrier is 35 mm, it is possible to calculate the tangential force that is downloaded on each screw (n=5), with the hypothesis of equal distribution:

$$F_s = \frac{T}{r \cdot n} = 571.5\ N$$

Then, knowing that the depth t of the holes is 10 mm and their diameter d measures about 6.65 mm, the pressure that is downloaded on their wall is:

$$p = \frac{F_s}{t \cdot d} = 8.6\ MPa$$

Since the yielding strength of the aluminium alloy 6060 is equal to 60 MPa, also from an analytic point of view the holes will not plasticize in any point.

5.5.3 FEM slipping analysis of the contact surfaces of the stator

This FEM analysis was necessary and more important than the plastic analysis, since this is a friction joint and so there must not be any slipping among the two contact surfaces, kept in contact by the preload of the screws. If the two surfaces are not perfectly constrained to each other, some issues arise, like the contact among the holes of the cover plate and the shank of the screws, making the joint a shear one instead of a friction one. The results in this case have been analysed in terms of contact status (CSTATUS), in order to evaluate the presence or absence of slipping due to the torque even with the preload applied on the screws.
In Figure 118 the surface of the magnets carrier that is kept in contact with the surface of the cover plate by means of the five M8 screws is shown, highlighting the status of the contact. The colour map indicates that the red means closed sticking contact, that is the positive situation, the green means closed and slipping contact and the blue means opened contact. Since the surface is almost completely red, and most of all there are not green elements, the joint works with friction and the two components are perfectly constrained. The blue area is due to the fact that the pressure cannot be uniformly distributed all over the surface, because the flange has not an infinite stiffness.

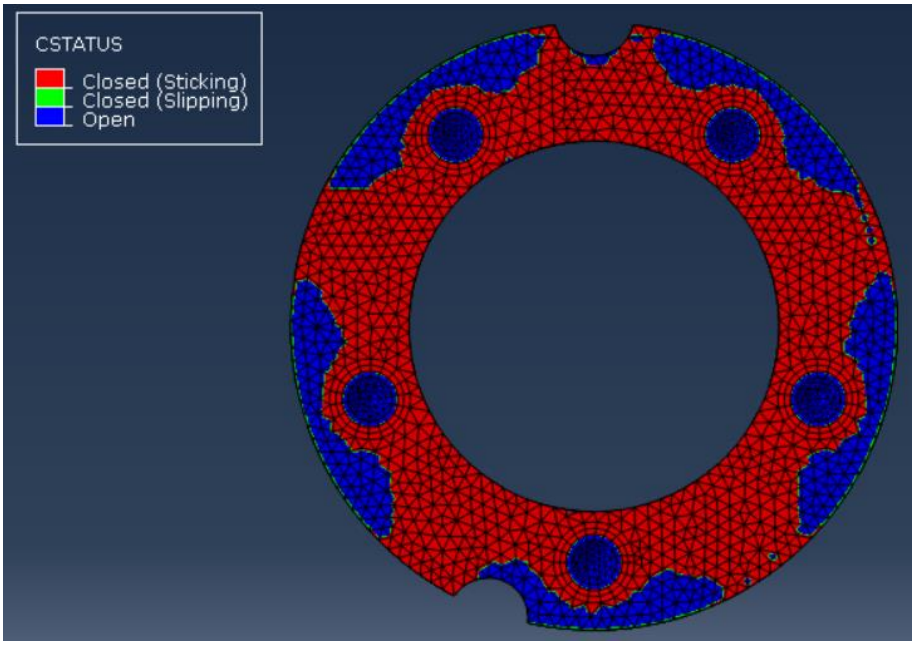

Figure 118 – Results in terms of CSTATUS of the slipping analysis performed on the stator

It can be concluded that the joint among the magnets carrier and the cover plate is rigidly constrained thanks to the friction generated by the preload of the screws, that is of 8784 N on each one.

6 Fatigue design

The fatigue assessments have been performed on the crankshaft and on the rod, that are the most stressed and novel components. The used fatigue design criterion is the infinite life one, hence the equivalent fatigue stress used for the assessments has to be lower than the endurance limit in all the points. The fatigue "index" is the Sines equivalent stress. For performing these assessments, more static FEM analysis done with Abaqus on each component and in specific load cases (two per component) have been combined for the evaluation of an equivalent fatigue stress to forecast their life. The procedure consists of taking the values of the 3D stresses in each node from the single static FEM assessments and compose a stress tensor in MatLab. With this latter software all the post process of the data for the fatigue assessments has been done. The principal operations to do are the definition of the tensor of the principal stresses, the calculation of the mean and average stresses and the computation of the Sines equivalent stress for each node. Finally, the Sines stress is compared to the endurance limit and graphic feedback of the of the nodes is done in MatLab, highlighting the critical ones.
The general procedure is here described, while the results are reported in the paragraphs related to the fatigue design of the components.
The staring data for the fatigue assessments are those coming from the reports of the Abaqus analysis, that contain the averaged value of the stresses evaluated for all the nodes. A graphic example of a report (for the first 10 nodes) is reported in Figure 119.

Node Label	S.S11 @Loc 1	S.S22 @Loc 1	S.S33 @Loc 1	S.S12 @Loc 1	S.S13 @Loc 1	S.S23 @Loc 1
1	-215.101	-130.773	-46.0039	5.58540	-4.36910	-48.2876
2	-313.012	-251.225	-119.191	27.2939	11.3955E-03	79.9149
3	-276.855	-138.478	-157.843	27.8594	-427.020E-03	-86.9124
4	-169.018	-21.9906	-106.399	2.78074	-3.82574	13.9698
5	-281.344	-141.567	-61.6823	9.58939	-7.98301	46.1010
6	-158.953	85.8844	17.0075	4.40442	-2.38273	-39.1489
7	-93.6449	61.6026	14.4888	1.39971	1.05063	30.2909
8	-177.256	-86.5201	-28.7627	458.182E-03	1.95782	-17.0569
9	-139.057	-51.1965	208.910	-11.9429	-25.5231	-43.8358
10	-280.434	-169.213	-200.494	-10.0564	45.5132	73.2382

Figure 119 – Example of the report file extracted from Abaqus with the stress values in each node (for the first 10 nodes)

Then, the remaining part of the fatigue design belongs to the MatLab script that has been developed during the present thesis work. This script has a main part which calls the function for extracting the stress values from the Abaqus report and the function for the extraction of the nodal coordinates from an Excel file. The Excel file is created importing the nodal coordinates from the input (.inp) generated by Abaqus. Moreover, the whole algorithm for the data process is implemented in the main of the script. In the next part of the paragraph, these operations will be explained in a more detailed way, reporting some lines of the code when considered necessary. The whole MatLab code is reported in Appendix 1.
First of all, the data of the material used for the fatigue assessment must be defined, and they are the same for both the crankshaft and the rod. These data are the ultimate tensile strength, the surface finishing and the dimensional coefficients, whose values are reported in the following table (Table 35).

Table 35 – Material data of both the crankshaft and the rod used for the fatigue design

Parameter	Variable name	Value	Unit
Ultimate tensile strength	UTS	980	MPa
Surface finish coefficient	b2	0.8	-
Dimensional coefficient	b3	0.8	-

Then, the fatigue endurance limit is compute by considering the properties of the material (UTS) and of the component (b2 and b3).

$$\sigma_e' = 0.5 \cdot UTS \cdot b2 \cdot b3 = 313.6\ MPa$$

The notch effect is not considered in the evaluation of the endurance limit because it is already embedded in the Abaqus results. Indeed, this is a local approach for the fatigue assessment, where the stresses are directly taken from the FE software.
For the fatigue design, it is useful to create a stress tensor for each node, rearranging the stresses of the report file into matrix. The matrix form for each node k is reported below.

$$[S_{ij}]_k = \begin{bmatrix} S11 & S12 & S13 \\ S21 & S22 & S23 \\ S31 & S32 & S33 \end{bmatrix}$$

The MatLab code implemented for creating the stress tensor in each node of the crankshaft, for a crank angle of 374°, is here reported.

```
sigma_374=[];

for i=1:1:(N)
    shear_stress=TENSOR_374(i,4:6);
    tensor_i=diag(TENSOR_374(i,1:3));
    tensor_i(1,2:3)=shear_stress(1:2);
    tensor_i(2,[1 3])=shear_stress([1 3]);
    tensor_i(3,1:2)=shear_stress(2:3);
    sigma_374=[sigma_374; tensor_i];
end
```

Then, from the generic stress tensors in the nodes, the principal stress tensors are generated. A tensor of the principal stress for the k-esim node has the following form.

$$[\sigma_i]_k = \begin{bmatrix} \sigma_I & 0 & 0 \\ 0 & \sigma_{II} & 0 \\ 0 & 0 & \sigma_{III} \end{bmatrix}$$

The principal stresses in the k-esim node are extracted from the generic tensor as eigenvalues, and then rearrange as the diagonal of new matrix, operation repeated for all the nodes. Below, the part of the script aimed for doing this operation is reported for the crankshaft in the case of the crank angle equal to 374°.

```
princ_stress_374=[];
l_374=size(sigma_374);

```

```
14.  for i=1:3:l_374(1)
15.      k=i+2;
16.      A=sigma_374(i:k,:);
17.      princ_stress_374=[princ_stress_374; eig(A)'];
18.  end
```

Once that for each node a tensor of the principal stresses is defined, it is necessary to recognise the alternate and mean contribution of each principal stress.

$$\sigma_{i,a} = \frac{\sigma_{i,max} - \sigma_{i,min}}{2} \qquad \sigma_{i,m} = \frac{\sigma_{i,max} + \sigma_{i,min}}{2}$$

The obtained matrices are so composed by the alternative and mean part of the principal stresses and they are composed as follow.

$$[\sigma_{i.a}]_k = \begin{bmatrix} \sigma_{I,a} & 0 & 0 \\ 0 & \sigma_{II,a} & 0 \\ 0 & 0 & \sigma_{III,a} \end{bmatrix} \qquad [\sigma_{i.m}]_k = \begin{bmatrix} \sigma_{I,m} & 0 & 0 \\ 0 & \sigma_{II,m} & 0 \\ 0 & 0 & \sigma_{III,m} \end{bmatrix}$$

Finally, once these matrices are defined, the equivalent stress for the Sines criterion in all the k-esim nodes can be evaluated. The two-principal quantity to be computed are the Sines equivalent stress and the firs invariant. The Sines equivalent stress is computed with only the alternating components of the principal stresses in each node in the following way.

$$\sigma^*_{s,k} = \sqrt{\sigma^2_{I,a} + \sigma^2_{II,a} + \sigma^2_{III,a} - \sigma_{I,a}\sigma_{II,a} - \sigma_{II,a}\sigma_{III,a} - \sigma_{I,a}\sigma_{III,a}}$$

The first invariant is on the contrary evaluated only considering the mean components of the principal stresses as follows.

$$I_{m,k} = \sigma_{I,m} + \sigma_{II,m} + \sigma_{III,m}$$

Once that these two quantities have been calculated, the fatigue criterion can be applied, and its formulation is here illustrated.

$$\frac{\sigma^*_{s,k}}{1 - \frac{I_{m,k}}{UTS}} \leq \frac{\sigma'_e}{\eta}$$

If the Sines criterion is not verified, the component does not last for infinite life, and so a failure may happen after a certain number of cycles. The results of the fatigue assessment have also been illustrated in a graphic way, by plotting the nodes in three dimensions thanks to the function “scatter3” of MatLab, highlighting both the nodes that do not last for infinite life and the nodes with the lower safety factor. More details will be given in the paragraphs where the results are shown.

6.1 Fatigue assessment on the crankshaft

The fatigue assessment on the crankshaft has been performed by analysing the two most critical cases taken from the FEM results. The FE model of the crankshaft is the one described in the paragraph 5.3.3 and the components are those that have already been modified after the static assessment. The critical cases have been selected among five load cases, that were considered of interest from a fatigue point of view.
The load cases under investigation could also have been chosen by looking at the internal action diagrams shown in the paragraph of the analytical static assessment (5.3.1.2), selecting the two cases with the maximum bending moments in the opposite side (α=14° and α=374°). Indeed, in general for the fatigue life of a component, the more the amplitude of the stress cycle, the less the expected duration.
Anyway, due to the complexity of the geometry and for making sure that the most critical cases are the two cited before, the load cases analysed have been five:

- α=0° selected because R1 assumes its lowest value during a complete cycle
- α=14° selected because R2 assumes its highest value during a complete cycle
- α=180° selected because all the forces have a low value
- α=360° selected because R2 assumes its lowest value during a complete cycle
- α=374° selected because R1 assumes its highest value during a complete cycle

In Figure 120 the forces that are applied to the crankshaft (remember that the index '1' is referred to the piston 1 while the index '2' is referred for the piston 2) are shown as a function of the crank angle, with reference to the local reference system.

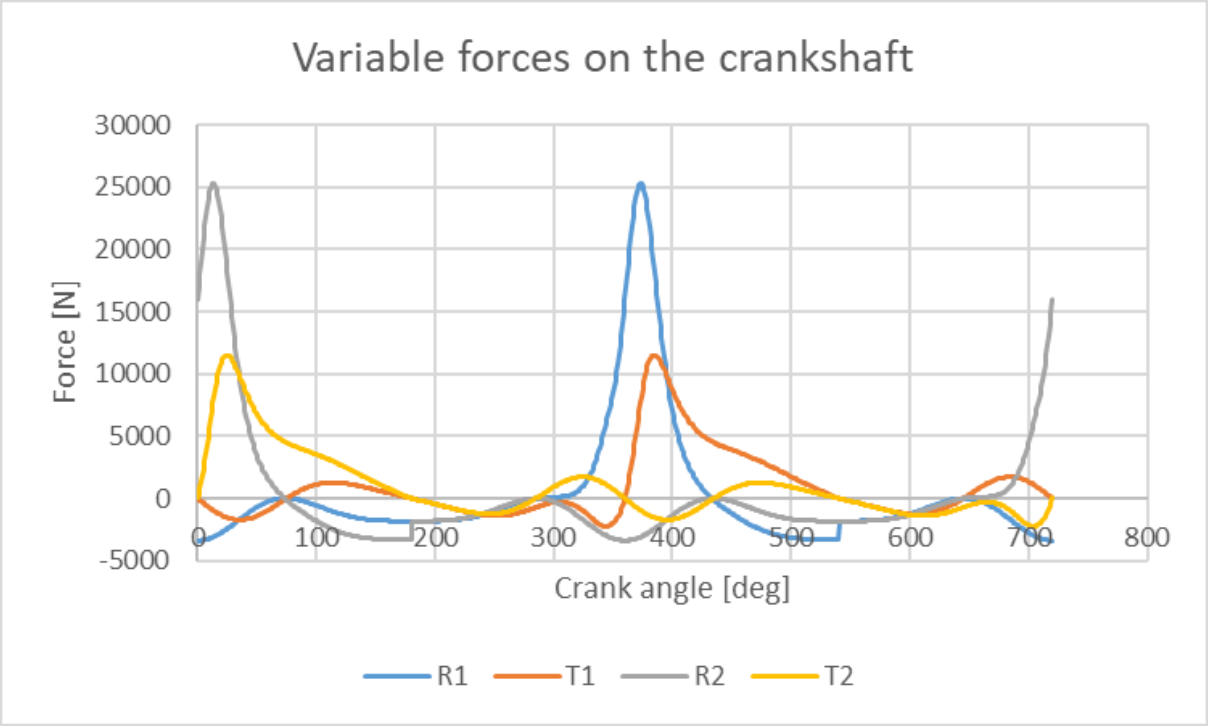

Figure 120 – Forces on the crankshaft as a function of the crank angle

The values of the forces are reported in Figure 120, already transformed for the global reference system for being used in Abaqus.

Table 36 – Values of the forces that acts on the crankshaft for the selected load cases

Crank angle [deg]	R1 [N]	T1 [N]	R2 [N]	T2 [N]
0	3388	0	15959	0
14	3022	-1066	25094	-8848
180	1832	-23	-1832	23
360	-15959	0	-3387.25	0
374	-25094	8848	-3022	1066

The results of the FEM analysis performed with the chosen load cases are reported in Table 37 in a qualitative way, for showing the deformed shapes.

Table 37 – Deformed shapes of the crankshaft for the load cases analysed with the FEM

Deformed shapes of the crankshaft for the load cases analysed with the FEM	
α=0°	**α=14°**
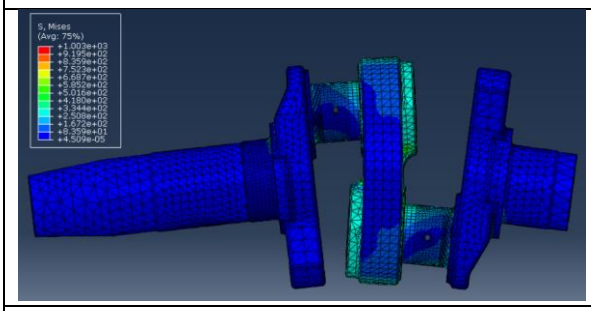	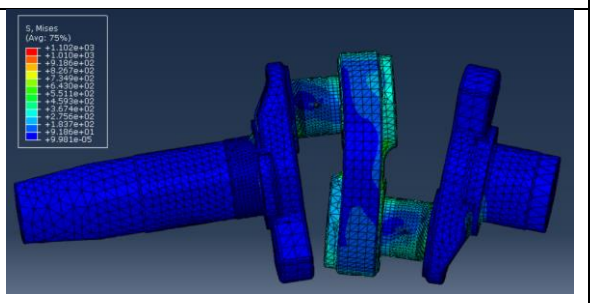
α=360°	**α=374°**
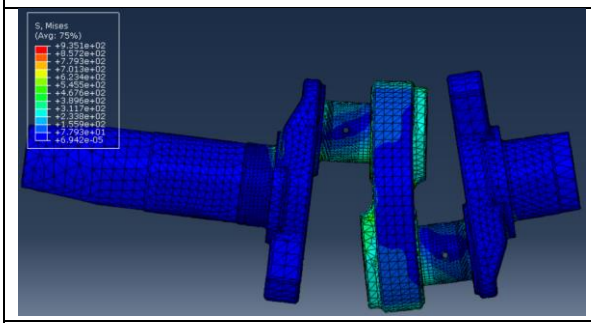	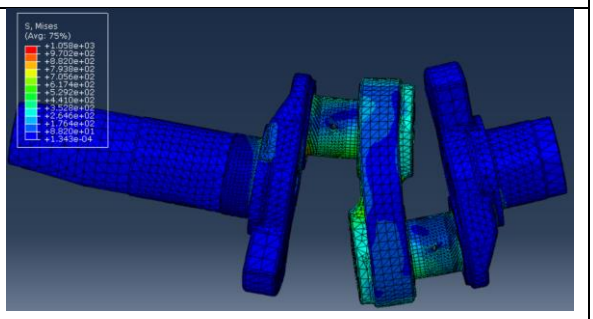
α=180°	
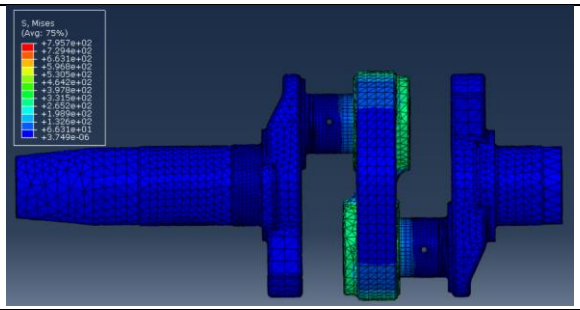	

As predicted, the most critical cases are those with the maximum opposite bending moment, that are for the crank angles of 14° and 374°. Thus, the fatigue assessment has been performed by assuming a sinusoidal load condition, taking as maximum stresses those for the crank angle equal to 374° and as minimum stresses those for the crank angle equal to 14°.

The fatigue assessment has been done for the anterior and posterior cranks, while it has been considered useless for the central part of the crankshaft since it is not even statically assessed in the most critical zones. Moreover, the results of the fatigue assessment of the anterior and posterior cranks are considered reliable only if the FEM results in the considered nodes are reliable. For example, all the nodes that belong to the boundary of the kinematic coupling are not taken into consideration in the analysis of the MatLab results; they can be recognized thanks to the graphical representation of the results.
The outcomes of the fatigue assessments performed on the posterior and anterior cranks, are respectively shown in Figure 121 and in Figure 125, where the red points represent the nodes for which the Sines criterion is not satisfied. The reliable results have also been highlighted with a black dashed line.
The posterior crank presents two critical zones, both located on fillets that create a notch effect; one of them also reaches the yielding, according to the FEM static strength assessment performed before (the upper one in the figure below).

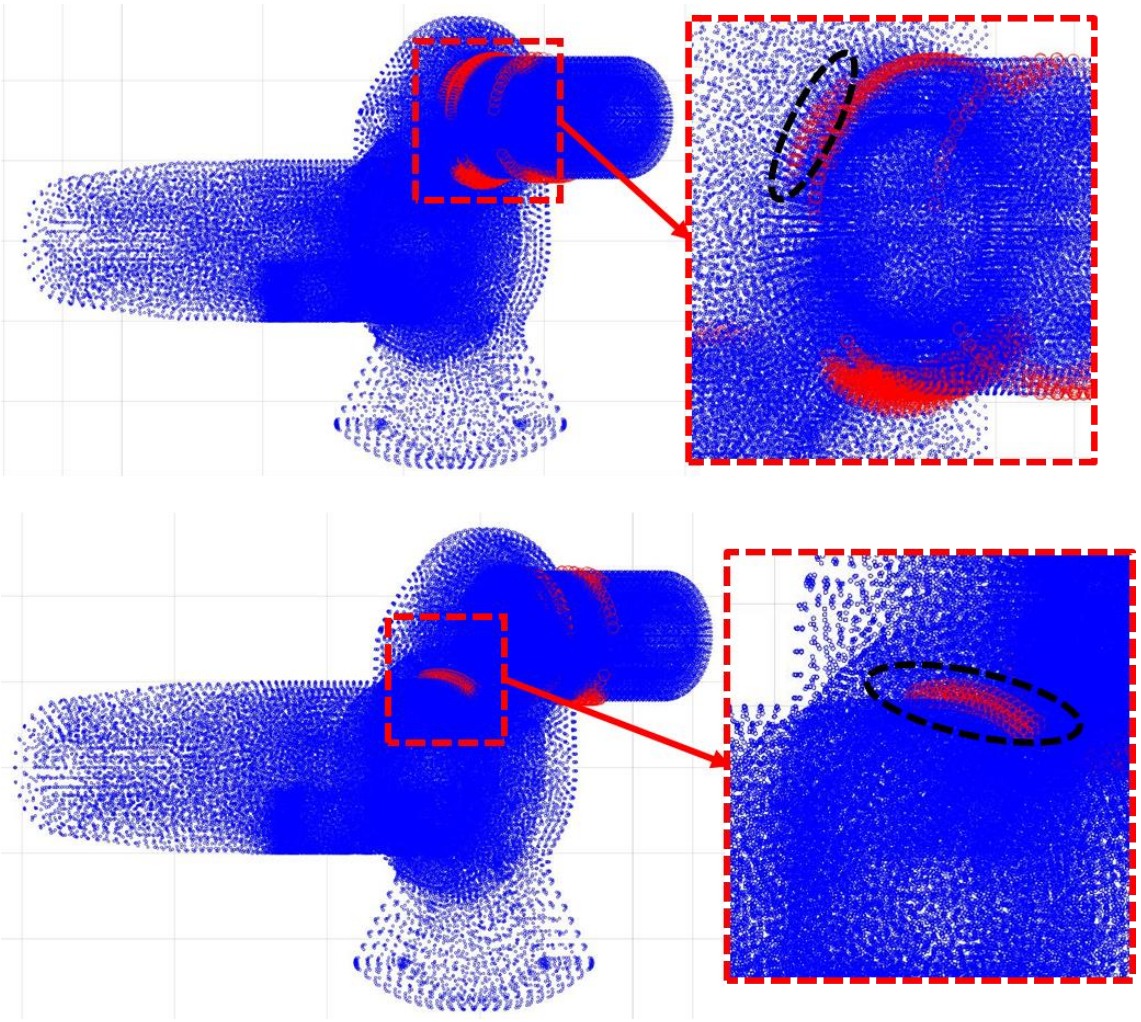

Figure 121 - Results of the fatigue assessment performed on the posterior crank; the black dashed line indicates the reliable results

A deeper analysis on the posterior crank has been done in the critical zone show in the bottom part of Figure 121, to quantify the entity of the equivalent stress used for the Sines criterion and consequently to evaluate the safety factor. For doing this, it has been

necessary to do another FEM analysis, focusing the resources on that fillet by using C3D20R and a very fine mesh, as shown in Figure 122. The mesh in the non-relevant zones has been relaxed, for saving computational time.

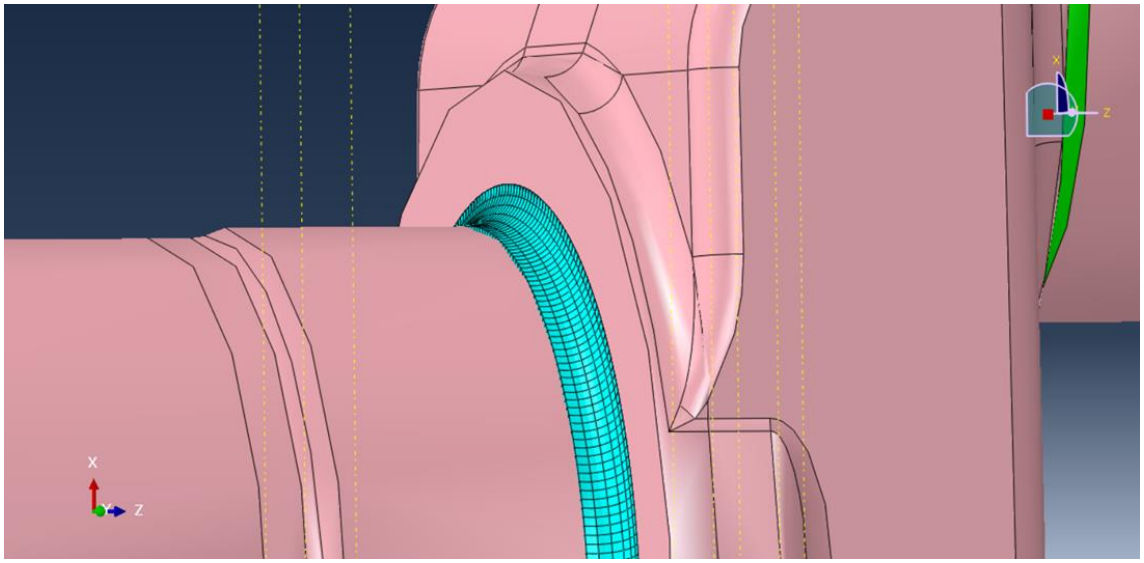

Figure 122 – Refined mesh with C3D20R elements of the critical part of the posterior crank

The results of the FEM analysis, that has been performed for the crank angles of 374° and 14°, and the path used for the stresses extraction are shown in Figure 123.

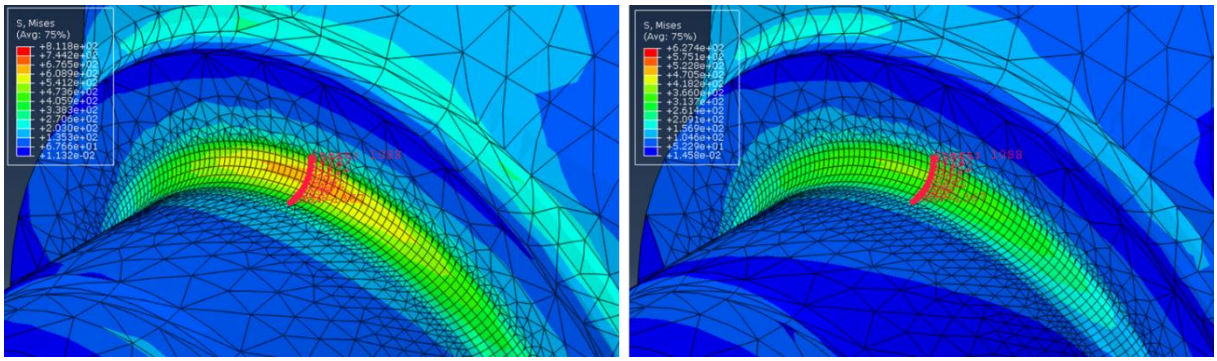

Figure 123 – Results of the FEM analysis performed for the two crank angles of 374° (left) and 14° (right)

Thanks to the stresses extracted from the path in the two configurations, a fatigue assessment using the Sines criterion has been done on such location. The results are illustrated in Figure 124, while in the following table (Table 38) the results of the fatigue assessment in the critical zone are reported.

Table 38 – Results of the fatigue assessment in the critical zone of the posterior crank

Endurance limit	Maximum equivalent stress	Safety factor
313.6 MPa	536.1 MPa	0.58

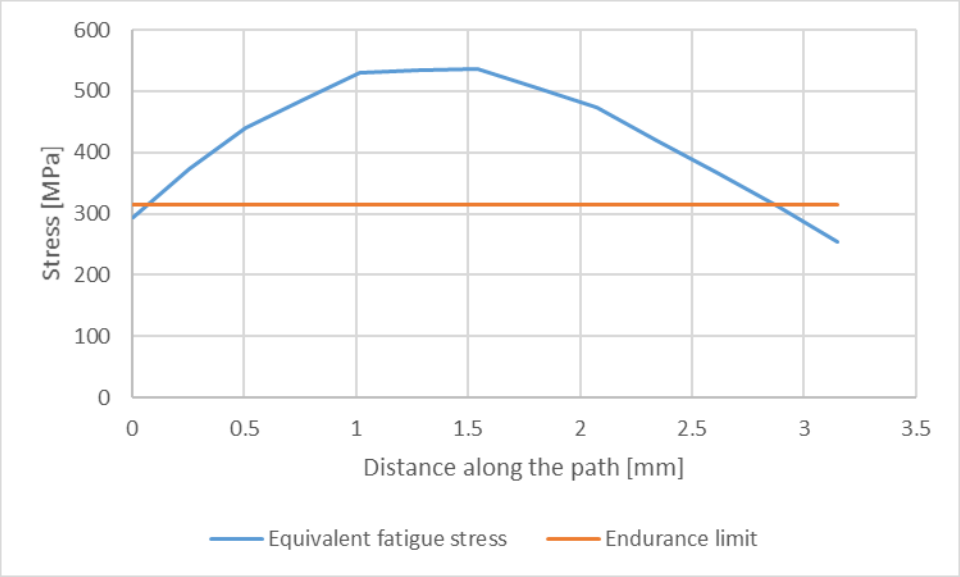

Figure 124 – Equivalent stress used for the Sines criterion in the critical zone of the posterior crank

The anterior crank presents one critical zone, even in this case located in correspondence of a fillet radius, that allow a stress concentration.

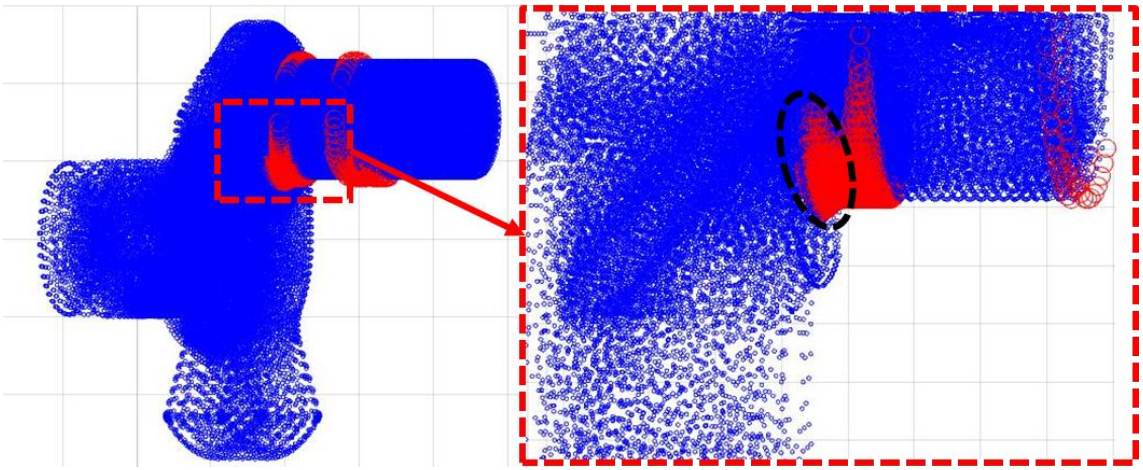

Figure 125 – Results of the fatigue assessment performed on the anterior crank; the black dashed line indicates the reliable results

The only solution for reducing this the stress concentration in correspondence on the notch is to increase the fillet radius. In this way the notch effect will be reduced, increasing the fatigue life of the components.

Then, also the safety factors between 1 and 1.5 have been plotted in the graphic model of MatLab, to look for the nodes that, despite they satisfy the infinite life design criterion, are not so much safe. This procedure has highlighted some critical zones for both the components other than those which do not last for infinite life. The results of the posterior crank are shown in Figure 126 while those of the anterior crank are shown in Figure 127. The posterior crank presents a single node in a location different from those found from the Sines criterion that has a safety factor among 1 and 1.5. Since it is a single node, it is supposed to be safe and with a safety factor near 1.5.

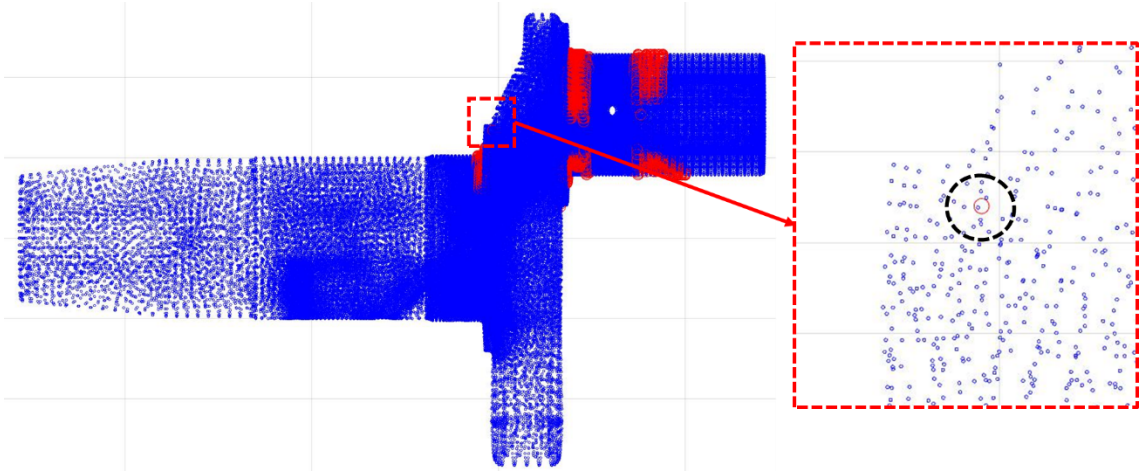

Figure 126 - Safety factors between 1 and 1.5 of the nodes of the posterior crank

The anterior crank presents some nodes with a safety factor among 1 and 1.5 located in a different zone respect to the nodes that do not satisfy the Sines criterion. In particular, as shown in Figure 127, there are two groups of such nodes that are highlighted with a black dashed line. The lower group is in a position that correspond to a fillet, and since the specular fillet in the posterior crank does not satisfy the Sines criterion, its radius will be increased even for the anterior crank in any case. The upper group is composed by few nodes, so it is supposed to be a safe zone, with a safety factor near 1.5.

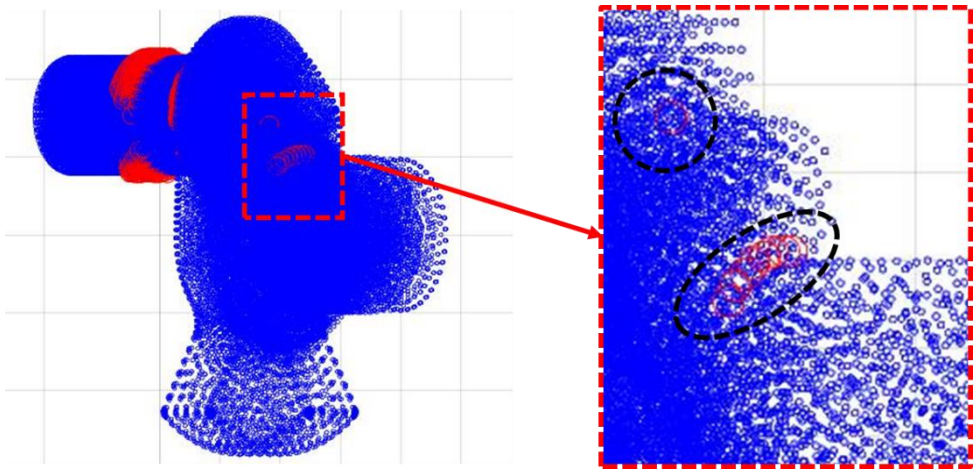

Figure 127 – Safety factors between 1 and 1.5 of the nodes of the anterior crank; the black dashed line indicates the reliable results

In the following picture (Figure 128), a recap of the results of the fatigue assessment performed on the posterior and anterior cranks with a cooperation of Abaqus and MatLab is reported. The parts that do not last for infinite life are those highlighted with red colour, while those with a safety factor comprised the values of 1 and 1.5 are highlighted with orange colour.

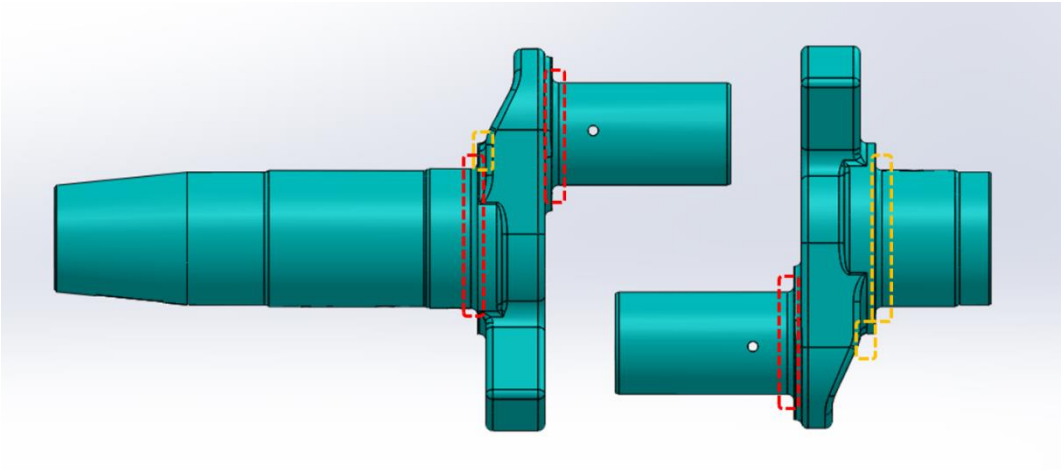

Figure 128 – Critical zones for the fatigue life of the posterior and anterior cranks

6.2 Fatigue assessment on the rod

The fatigue assessment on the rod has been performed among the conditions of maximum traction and of maximum compression, present at the maximum rotational speed of 4000 rpm. The two critical load conditions have been simulated in Abaqus, and then the results have been processed with MatLab for applying the Sines criterion to each node.
The graph in Figure 129 shows the trend of the total force that acts on the rod at the regime of 4000 rpm. The force used for the fatigue assessment are the upper (compression) and the lower (traction) bounds, and their values is reported in Table 39, already transformed for the global reference system of Abaqus.

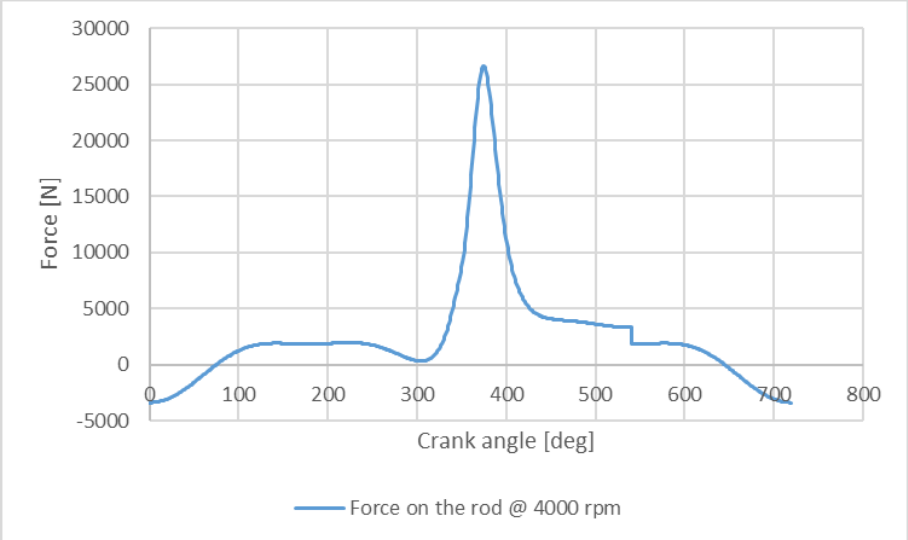

Figure 129 – Force on the rod @ 4000 rpm as a function of the crank angle

Table 39 – Force used for the fatigue assessment on the rod

Load condition	Force value	Unit
Maximum compression	-26608	N
Maximum traction	3388	N

The results of the fatigue assessment in terms of Sines criterion are illustrated in a graphical way in Figure 130. Since the red points indicate the nodes that do not satisfy the

Sines criterion, it is possible to state that the rod will last for infinite life, since all the point are blue. The maximum equivalent stress found for the Sines criterion is equal to 216 MPa.

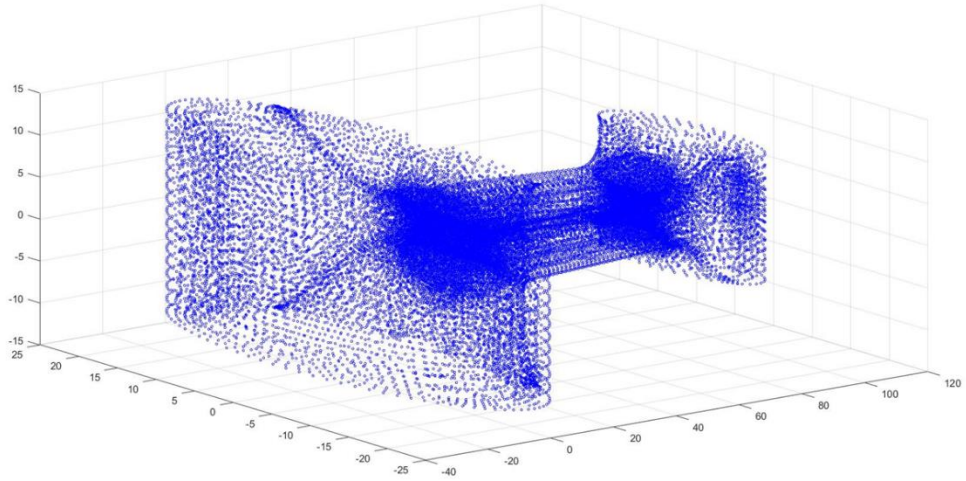

Figure 130 – Graphic result of the fatigue assessment on the rod

Then, for evaluating the most critical areas of the rod, even the safety factor for all the nodes has been plotted in the 3D graph (Figure 131). The red points represent the values of the safety factor that are comprised between the minimum value (1.45) and 2; the upper limit of the safety factor (2) has been arbitrarily selected. The zone with the lowest safety factor is located near the foot of the rod, where the section has the minimum area and it is changing its geometry, causing a notch effect. However, the minimum safety factor is equal to 1.45 and so the rod is safe.

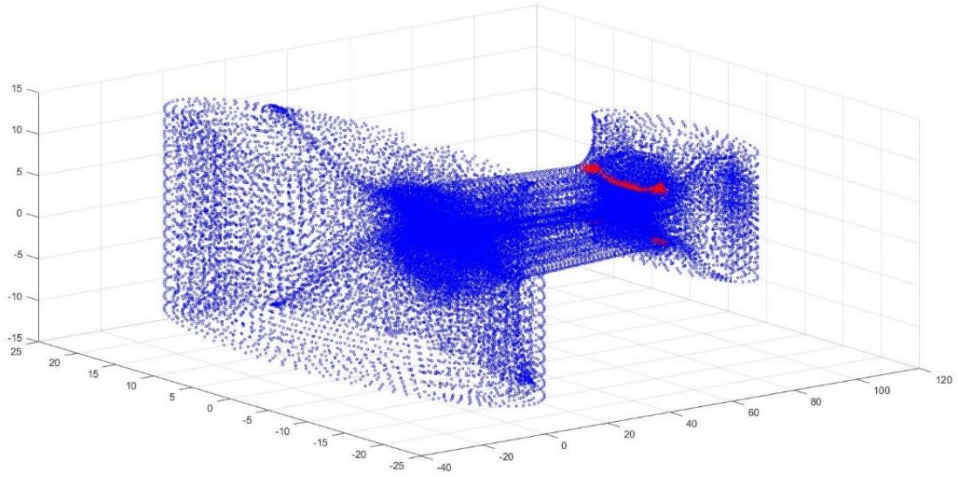

Figure 131 - Safety factors of the fatigue assessment of the rod; the red points represent the values within the minimum safety factor (1.45) and 2

Concluding, it is possible to say that from an analytical point of view, the rod will last to infinite life.

7 Conclusions

The purpose of this work was to assess the main components of a new internal combustion engine used as range extender on the electric vehicle. For doing it, the pieces designed with the first attempt geometry have been used as inputs for the assessments, to check their behaviour under the loads for which they were designed. Some of them are resulted properly sized, while others show some critical points that can cause failures. For these latter has been necessary to propose corrective actions, some of which already made and others to be done.
The main activities and results of this thesis can be summarized in the following points:

- Materials qualitative analysis for assessing the environmental impact of the internal combustion engine.
- Fuel consumption estimation for a first comparison with the range extender mounted on the BMW i3.
- Determination of the tolerance of the interference fits for joining together the components of the crankshaft and the related assessments, with positive results
- Static strength assessment of the crankshaft, that has highlighted some critical zones; after it, the inner radius of the crankpin and the fillet radius of the central part of the crankshaft have been modified, for reducing the Von Mises stress. The fillet radius of the crankpin is a critical point, but it has not already been modified.
- Slipping assessment of the interference fits of the crankshaft performed with the minimum elastic interference and the maximum torque; the FEM result can be considered positive, since the slipping is absent, but some fretting problem may arise.
- Fatigue assessment of the crankshaft, performed even if not all the zones work in the elastic field (the static assessment is not completely satisfied) for finding other critical issues; two fillet radii of the crankshaft (that statically work in the elastic field) show a finite life, making necessary some changes for reducing the stress concentration. The critical fillet radii are those of the main bearing journals.
- Modal analysis of the crankshaft, whose result ensure that it works far from resonance conditions.
- Static strength assessment and fatigue assessment of the connective rods, which ended with a positive result.
- Fretting assessment of the bushing bearing of the head of the connecting rods, with a positive result.
- Elasto-plastic analysis and slipping analysis of the friction bolted joint that connects the two components of the stator of the electric generator, with a positive result.

Concluding, it is possible to say that the development of the range extender is proceeding respecting the scheduling, but some changes to the critical components are necessary before starting with the testing phase.

Bibliography

[1] AA. VV., *Manuale dell'ingegnere meccanico*, Hoepli

[2] Andrea Gilioli, Dario Braconi, Mario Guagliano, 2017, "Fatigue design of a twin internal combustion engine for a light helicopter by a CAE-based approach", International journal of structural integrity, Vol. 8 Issue: 6, pp. 632-647

[3] Arber Pasha, 2013, "Sviluppo di un approccio di previsione della durata a fretting di bielle automobilistiche", M. Sc. thesis, Politecnico di Milano

[4] Choi K.S., Pan J., 2009, "Simulation of stress distribution in crankshaft section under fillet rolling and bending tests", International journal of fatigue, Vol. 31 Issue: 3, pp. 544-557

[5] Daniela Vignocchi, 2002, *Elementi di progettazione del motore*. *Presentazione di Mauro Forghieri*, First ed., Athena, Modena

[6] Dassault systems, Abaqus Analysis User's Guide, Simulia Abaqus 6.14, link: http://abaqus.software.polimi.it/v6.14/books/usb/default.htm

[7] FERRARI G., 1996, *Motori a combustione interna,* Capitello, Torino

[8] Handouts from the Machine Design 2 course

[9] Handouts from the Methods for Advanced Mechanical Design course

[10] Mathworks, MatLab R2017b tutorials, link: https://it.mathworks.com/support/learn-with-matlab-tutorials.html

[11] Mathworks, MatLab R2017b documentation, link: https://it.mathworks.com/help/

[12] M. Guagliano, A. Terranova, L. Vergani, 1993, "Theoretical and experimental study of the stress concentration factor in diesel engine crankshafts", Journal of mechanical design, Vol. 115, pp. 47-52

[13] Montazersadgh F., Fatemi A., 2007, "Dynamic load and stress analysis of a crankshaft", SAE Technical Paper No. 2007-010258

[14] Montazersadgh F., Fatemi A., 2007, "Stress analysis and optimization of crankshafts subject to dynamic loading", Forging Industry Educational Research Foundation (FIERF) and American Iron and Steel Institute (AISI), The university of Toledo, Toledo, OH

[15] Paulina Krolo, Davor Grandic, Mladen Bulic, 2016, "The guidelines for modelling the preloading bolts in the structural connection using finite element methods", Journal of Computational Engineering Volume 2016, Article ID 4724312

[16] PETERSON R.E., 1974, *Stress concentration factors*, Wiley, New York

[17] Pravardhan S.S., 2004, “Dynamic load analysis and optimization of connecting rod”, M. Sc. Thesis, University of Toledo, Toledo, OH

[18] Sines G., 1955, *Failure of Materials under Combined Repeated Stress with Superimposed Static Stresses*, NACA, Washington, DC

[19] Sines G., 1959, “Behaviour of metals under complex static and alternating stresses”, in Sines R.G. and Waisman J.L. (Eds), *Metal Fatigue*, McGraw Hill, New York, NY, pp. 145-469

[20] THOMSON W., 1978, *Fundamentals of automotive engine balance*, Mechanical Engineering publications, London

[21] Vidner J., Leidich E., 2007, “Enhanced Ruiz criterion for the evaluation of crack initiation in contact subjected to fretting fatigue”, International journal of fatigue, Vol. 29 Issue: 9-11, pp. 2040-2049

[22] Wen L.Z., Guan Z.W., Song J.F., Chen Y., 2011, “Finite element analysis of vehicle engine connection rod under mechanical load”, Advanced Materials Research, Vols 314-316, pp. 653-656

Appendix 1

- Main of the MatLab script that performs the fatigue assessments on each node of the FE models defined and processed in Abaqus in the two selected maximum and minimum load configurations

```
clc; clear all; close all;
%%DATA
UTS=980; %MPa
b2=0.8;
b3=0.8;
s_lim=0.5*UTS*b2*b3; %MPa

%[Node, xn, yn, zn] =
importfile('Coordinate_nodali_Man_Ant.xlsx','Sheet1',4,114042);
[Node, xn, yn, zn] =
importfile('Coordinate_nodali_Man_Post.xlsx','Sheet1',4,145270);
N=length(Node);

%% Extract principal stresses in each node for the maximum and the
minimum load

%extract the stress components for the maximum load

%[TENSOR_374, IDs_374, nodalListing_374, elementListing_374] =
getRPT('Man_Ant_374.rpt');
[TENSOR_374, IDs_374, nodalListing_374, elementListing_374] =
getRPT('Man_Post_374.rpt');

%reorder the matrix

sigma_374=[];

for i=1:1:(N)
    shear_stress=TENSOR_374(i,4:6);
    tensor_i=diag(TENSOR_374(i,1:3));
    tensor_i(1,2:3)=shear_stress(1:2);
    tensor_i(2,[1 3])=shear_stress([1 3]);
    tensor_i(3,1:2)=shear_stress(2:3);
    sigma_374=[sigma_374; tensor_i];
end

princ_stress_374=[];
l_374=size(sigma_374);

for i=1:3:l_374(1)
    k=i+2;
    A=sigma_374(i:k,:);
    princ_stress_374=[princ_stress_374; eig(A)'];
end

%extract the stress components for the minimum load
```

```
%[TENSOR_14, IDs_14, nodalListing_14, elementListing_14] =
getRPT('Man_Ant_14.rpt');
[TENSOR_14, IDs_14, nodalListing_14, elementListing_14] =
getRPT('Man_Post_14.rpt');

%reorder the matrix

sigma_14=[];

for i=1:1:(N)
    shear_stress=TENSOR_14(i,4:6);
    tensor_i=diag(TENSOR_14(i,1:3));
    tensor_i(1,2:3)=shear_stress(1:2);
    tensor_i(2,[1 3])=shear_stress([1 3]);
    tensor_i(3,1:2)=shear_stress(2:3);
    sigma_14=[sigma_14; tensor_i];
end

%extract principal stresses for each node

princ_stress_14=[];
l_14=size(sigma_14);

for i=1:3:l_14(1)
    k=i+2;
    A=sigma_14(i:k,:);
    princ_stress_14=[princ_stress_14; eig(A)'];
end

%% Alternating and mean stress components

s_a=((princ_stress_374-princ_stress_14)/2);

s_m=(princ_stress_374+princ_stress_14)/2;

%% Application of the Sines criterion in each node

s_sines=[];
C=[];
S=ones(N,1)*5;
D=[];
G=ones(N,1)*5;
a=0;
for i=1:(N)
        s_sines=[s_sines; sqrt(s_a(i,1)^2+s_a(i,2)^2+s_a(i,3)^2-
s_a(i,1)*s_a(i,2)-...
       -s_a(i,1)*s_a(i,3)-s_a(i,2)*s_a(i,3))/(1-
(s_m(i,1)+s_m(i,2)+s_m(i,3))/UTS)];

       if s_sines(i)<s_lim
          C=[C; 0 0 1];

       else
          C=[C; 1 0 0 ];
          S(i)=100;
          a=1;
```

```
        end
        if (s_lim/s_sines(i) < 1) || (s_lim/s_sines(i) > 1.5)
            D=[D; 0 0 1];
        else
            D=[D; 1 0 0];
            G(i)=100;
        end
end

if a~= 0
    disp('Il componente non ha vita infinita')
end

%% Graphics creation

figure (1)
scatter3 (zn, yn, xn, S, C);

figure (2)
scatter3 (zn, yn, xn, G, D);

%% Display the minimum safety factor and the maximum Equivalent
stress for the Sines criterion

s_lim/max(s_sines)

max(s_sines)
```

Ringraziamenti

Ringrazio il Professor Mario Guagliano per avermi offerto l'opportunità di svolgere questa tesi ed anche per essere stato sempre presente ed un grande dispensatore di consigli.
Ringrazio Roberto Papetti e Filippo Marino della Robby Moto Engineering, per la loro infinita disponibilità e per tutte le nozioni sui motori (anche per il pranzo a Casalmaggiore).
Ringrazio la mia famiglia, per avermi sopportato e sostenuto durante questi anni di università e soprattutto in questi ultimi mesi, cosa per nulla semplice.